

University of Denver

Digital Commons @ DU

---

Electronic Theses and Dissertations

Graduate Studies

---

1-1-2017

## 3D Bioprinting Hydrogel for Tissue Engineering an Ascending Aortic Scaffold

Benjamin Stewart  
*University of Denver*

Follow this and additional works at: <https://digitalcommons.du.edu/etd>



Part of the [Biomedical Engineering and Bioengineering Commons](#)

---

### Recommended Citation

Stewart, Benjamin, "3D Bioprinting Hydrogel for Tissue Engineering an Ascending Aortic Scaffold" (2017). *Electronic Theses and Dissertations*. 1269.  
<https://digitalcommons.du.edu/etd/1269>

This Thesis is brought to you for free and open access by the Graduate Studies at Digital Commons @ DU. It has been accepted for inclusion in Electronic Theses and Dissertations by an authorized administrator of Digital Commons @ DU. For more information, please contact [jennifer.cox@du.edu](mailto:jennifer.cox@du.edu), [dig-commons@du.edu](mailto:dig-commons@du.edu).

---

# 3D Bioprinting Hydrogel for Tissue Engineering an Ascending Aortic Scaffold

## Abstract

The gold standard in 2016 for thoracic aortic grafts is Dacron<sup>®</sup>, polyethylene terephthalate, due to the durability over time, the low immune response elicited and the propensity for endothelialization of the graft lumen over time. These synthetic grafts provide reliable materials that show remarkable long term patency. Despite the acceptable performance of Dacron<sup>®</sup> grafts, it is noted that autographs still outperform other types of vascular grafts when available due to recognition of the host's cells and adaptive mechanical properties of a living graft. 3-D bioprinting patient-specific scaffolds for tissue engineering (TE) brings the benefits of non-degrading synthetic grafts and autologous grafts together by constructing a synthetic scaffold that supports cell infiltration, adhesion, and development in order to promote the cells to build the native extracellular matrix in response to biochemical and physical cues. Using the BioBots 3-D bioprinter, scaffold materials we tested non-Newtonian photosensitive hydrogel that formed a crosslinked matrix under 365 nm UV light with appropriate water content and mechanical properties for cell infiltration and adhesion to the bioprinted scaffold. Viscometry data on the PEGDA-HPMC 15%-2% w/v hydrogel (non-Newtonian behavior) informed CFD simulation of the extrusion system in order to exact the pressure-flow rate relationship for every hydrogel and geometry combination. Surface tension data and mechanical properties were obtained from material testing and provide content to further characterize each hydrogel and resulting crosslinked scaffold. The goal of this work was to create a basis to build a database of hydrogels with corresponding print settings and resulting mechanical properties in order to progress the field of tissue engineered vascular grafts fabricated by nozzle-based rapid prototyping.

## Document Type

Thesis

## Degree Name

M.S.

## Department

Bioengineering

## First Advisor

Ali N. Azadani, Ph.D.

## Second Advisor

Corinne Lengsfeld

## Third Advisor

Matthew Rutherford

## Keywords

3D Bioprinting, Bioreactor, Hydrogel, Scaffold, Tissue engineering, Vascular graft

## Subject Categories

Biomedical Engineering and Bioengineering

---

**Publication Statement**

Copyright is held by the author. User is responsible for all copyright compliance.

3D BIOPRINTING HYDROGEL FOR TISSUE ENGINEERING AN ASCENDING AORTIC SCAFFOLD

A Thesis

Presented to

the Faculty of the Daniel Felix Ritchie School of Engineering and Computer Science

University of Denver

In Partial Fulfillment

of the Requirements for the Degree

Master of Science

by

Benjamin Stewart

June 2017

Advisor: Dr. Ali N. Azadani

Author: Benjamin Stewart

Title: 3D BIOPRINTING HYDROGEL FOR TISSUE ENGINEERING AN ASCENDING AORTIC SCAFFOLD

Advisor: Dr. Ali N. Azadani

Degree Date: June 2017

## ABSTRACT

The gold standard in 2016 for thoracic aortic grafts is Dacron<sup>®</sup>, polyethylene terephthalate, due to the durability over time, the low immune response elicited and the propensity for endothelialization of the graft lumen over time. These synthetic grafts provide reliable materials that show remarkable long term patency. Despite the acceptable performance of Dacron<sup>®</sup> grafts, it is noted that autographs still outperform other types of vascular grafts when available due to recognition of the host's cells and adaptive mechanical properties of a living graft. 3-D bioprinting patient-specific scaffolds for tissue engineering (TE) brings the benefits of non-degrading synthetic grafts and autologous grafts together by constructing a synthetic scaffold that supports cell infiltration, adhesion, and development in order to promote the cells to build the native extracellular matrix in response to biochemical and physical cues. Using the BioBots 3-D bioprinter, scaffold materials we tested non-Newtonian photosensitive hydrogel that formed a crosslinked matrix under 365 nm UV light with appropriate water content and mechanical properties for cell infiltration and adhesion to the bioprinted scaffold. Viscometry data on the PEGDA-HPMC 15%-2% w/v hydrogel (non-Newtonian behavior) informed CFD simulation of the extrusion system in order to exact the pressure-flow rate relationship for every hydrogel and geometry combination. Surface tension data and mechanical properties were obtained from material testing and provide content to further characterize each hydrogel and resulting crosslinked scaffold. The goal of this work was to create a basis to build a database of hydrogels with corresponding print settings and resulting mechanical properties.

# TABLE OF CONTENTS

I.	LIST OF TABLES.....	iv
II.	LIST OF FIGURES.....	v
III.	LIST OF ABBREVIATIONS.....	x
IV.	CHAPTER 1: INTRODUCTION.....	1
V.	CHAPTER 2: VASCULAR SYSTEM.....	5
	a. Vessels.....	7
	b. Valves.....	11
	c. Aortic Aneurysm.....	17
	d. Cells.....	23
	e. Reactions to Implants.....	30
VI.	CHAPTER 3: TISSUE ENGINEERING.....	37
	a. Materials.....	37
	b. Scaffold Fabrication.....	54
	i. Rapid Prototyping.....	55
	c. Bioreactor.....	66
	i. Cell Adhesion.....	67
VII.	CHAPTER 4: METHODS.....	73
	a. Hydrogel .....	73
	b. Viscometry.....	75
	c. Surface Tension.....	77
	d. Computational Fluid Dynamics.....	80
	e. Patient Specific Geometry.....	85
	f. Planar Biaxial Testing.....	86
	g. 3-D Bioprinting.....	88
VIII.	CHAPTER 5: RESULTS.....	92
IX.	CHAPTER 6: DISCUSSION.....	121
X.	CHAPTER 7: CONCLUSION.....	128
XI.	REFERENCES.....	131
XII.	APPENDIX.....	146

## LIST OF TABLES

<b>Table 1.</b> The uniaxial tensile mechanical properties of native and TE aortic valves, from MIT Cambridge et al. 2014 <sup>9</sup> .....	17
<b>Table 2.</b> The proteins that are useful in tissue engineering.....	42
<b>Table 3.</b> The polysaccharides that are useful in tissue engineering.....	43
<b>Table 4.</b> The synthetic polymers that are useful in tissue engineering.....	45
<b>Table 5:</b> Bond length and bond dissociation energies <sup>10</sup> .....	51
<b>Table 6.</b> Rapid prototyping techniques and attributes <sup>2-4</sup> .....	65
<b>Table 7.</b> Formula of high glucose DMEM from ThermoFisher Scientific <sup>7</sup> .....	70
<b>Table 8.</b> The table shows the best hydrogel composition.....	73
<b>Table 9.</b> Mesh independence study.....	82
<b>Table 10.</b> The boundary conditions and input parameters to the CFD simulation.....	84
<b>Table 11.</b> Surface tension of various fluids and hydrogels at room temperature 25C.....	98
<b>Table 12</b> Calculation of viscous and inertial forces for the best hydrogel when extruded from 0.21mm nozzle at 10 psi.....	99
<b>Table 13.</b> Calculation of dimensionless parameters for the best hydrogel when extruded from 0.21mm nozzle at 10psi.....	99
<b>Table 14.</b> Comparing the different syringe geometries. 0.508mm diameter nozzle 70,000 Pa inlet gauge pressure, 0 outlet gauge pressure, viscosity of 100 cP.....	103
<b>Table 15.</b> The viscosity data from the viscometer is close to the expected value from H-P equation but the error suggests that the small nozzle geometry creates less head loss than expected from its cone and plate behavior.....	108
<b>Table 16.</b> CFD results show effects of nozzle radius with Power Law fluid behavior.....	108
<b>Table 17.</b> PEO copolymer hydrogel with PEGDA 700.....	146
<b>Table 18.</b> Gelatin copolymer with PEGDA 700.....	147
<b>Table 19.</b> Alginate copolymer with PEGDA 700.....	148

## LIST OF FIGURES

<b>Figure 1.</b> The Tissue Engineering Technique <sup>1</sup> . Reproduced with permission, Copyright Massachusetts Medical Society.....	3
<b>Figure 2.</b> Complete aortic root and a depiction of an ascending aortic graft with bifurcations. Aorticdissection.com.....	7
<b>Figure 3.</b> The vascular wall contains three prominent layers held together with connective tissue lamina. Different cells types reside in each layer of the vessel wall. The aorta has its own circulatory system called the vasa vasorum designed within the adventitia layer traversing with nerve connections throughout the vessel wall.....	8
<b>Figure 4.</b> Human artery and vein under microscopy, AnatomyBox.com.....	8
<b>Figure 5.</b> Human Umbilical Vein Endothelial Cells, Nature 511 312-318.....	9
<b>Figure 6.</b> Material properties of human ascending aorta from Azadani et al. 2013 <sup>11</sup> .....	10
<b>Figure 7.</b> The left side shows the aortic wall and aortic valve leaflets. The right side shows the specific layers and the crimping of collagen during systole due to bending. The arterialis of the leaflet contains circumferentially arranged collagen while the ventricularis contains radially arranged elastin and collagen fibers.....	12
<b>Figure 8.</b> The valve during systole and diastole illustrating the communication of mechanical forces to the cells.....	13
<b>Figure 9.</b> Primary molecular structure of collagen <sup>12</sup> .....	14
<b>Figure 10.</b> Collagen is assembled in the cytoplasm into tropocollagen, secondary structure, which is secreted into the ECM for assembly into well-organized fibrils, tertiary structure.....	15
<b>Figure 11.</b> Elastin structure is much longer chains with a high degree of flexibility, reflected in the mechanical role that elastin plays in tissues <sup>13</sup> .....	16
<b>Figure 12.</b> A depiction of the roles the two elastic ECM proteins play <sup>13</sup> .....	16
<b>Figure 13.</b> Anatomy of aortic root and ascending aortic aneurysm <sup>14</sup> . .....	17
<b>Figure 14.</b> Blood pressure throughout the circulatory system .....	19
<b>Figure 15.</b> Material properties of aneurysm and normal tissue from the wall of the ascending aorta, Azadani et al 2013 <sup>15</sup> . (A) Aneurysm tissue circumferentially (B) normal tissue circumferentially (C) aneurysm tissue longitudinally, (D) normal ascending aorta tissue longitudinally.....	22
<b>Figure 16.</b> The cell membrane is a phospholipid bilayer riddled with select molecules, channels, receptors, relays, and effectors. The membrane is reinforced by a filamentous cytoskeleton. Chemical cues are received by receptors within the membrane, by passive diffusion through the membrane, and by channels that actively transport factors between cells and through the cell	



wall. These chemical signals trigger effectors which synthesize cyclic AMP from ATP in order to activate protein kinase, which triggers collagen synthesis. ....27

**Figure 17.** Force-dependent matrix remodeling and deposition of new matrix. The cells react to compression, stretch and shear stresses present in the tissue. The cytoskeleton gives cells shape and strength to adapt to external forces. Focal adhesions to the cell membrane of fibrils traversing from the nucleus provide a continuous mechanical linkage within the cell. Selectins, integrins and cadherins provide covalent bonds between the cell membrane and the ECM. Nuclear remodeling and translocation of transcription factors triggers an intracellular cascade of biochemistry that activates collagen synthesis, or degradation. Communicating in several modes the cells can change the diffusivity of their membrane, alter the conformation of membrane proteins to transport molecules into the cell, and activate amino acid protein chain construction. After synthesizing complete tropocollagen triple helices, the cell packages large molecules into vesicles for secretion through the phospholipid bilayer into the extracellular space where it is organized into collagen fibrils.....29

**Figure 18.** The cascade of events in response to implanted materials begins with extensive protein adhesion to the implanted material surface, which adhere monocytes to practically any material surface <sup>8</sup>.....31

**Figure 19:** Bond length between carbon atoms in polymer chains. The double bond in PEGDA is the most functional site for polymerization step-growth due to the covalent radius of carbon.....51

**Figure 20:** Photoinitiator radicalization for Irgacure, cytotoxic, and LAP, non-cytotoxic. ....51

**Figure 21:** PEGDA where n defines the molecular weight of the polymer chain and the length of each PEO monomer unit in the backbone chain is roughly 352 angstroms. ....52

**Figure 22:** LAP photoinitiator broken into its free radical and ionic pair after activation with 365 nm ultra-violet lightwaves. ....52

**Figure 23:** HPMC monomer has a larger molecular volume than PEGDA per atomic weight.....53

**Figure 24.** SEM micrographs of electrospun fibers of HPMC showing the polymerization into long straight chains at two different concentrations: (a) 0.5 wt% and (b) 1.0 wt%.....53

**Figure 25.** Selective laser sintering depiction. ....57

**Figure 26.** Soft lithography works in small print area. ....59

**Figure 27.** Two photon polymerization in a static bath. In the focal point of the near-infrared laser beams, the custom-made photosensitive polymer solution is crosslinked. ....61

**Figure 28.** Pressure-based extrusion uses a simple nozzle geometry to control flow rate.....63

**Figure 29.** Multi-disciplinary requirements that determine the constraints for ideal TE scaffold design.....65

<b>Figure 30.</b> Bioreactor schematic drawing showing the heated reservoir of optimal perfusion solution, piston pump, reactor chamber, backpressure chamber and silicone tubing.....	68
<b>Figure 31.</b> Bioreactor chamber circumferential stress imparted by pulsatile flow elicits a cellular response to remodel the ECM with more collagen due to mechanotransduction.....	69
<b>Figure 32.</b> Bioreactor chamber lumen surface shear stress imparted by the velocity gradient of flow elicits a cellular response of the endothelium to remodel the surface layer as well as communicate with the media and adventitia layers through microtubules and other intercellular junctions.....	69
<b>Figure 33.</b> The Bohlin instruments Viscometer with 4x40 cone and plate geometry, the standardized output of the software showing the viscosity relative to the shear stress and temperature, and an illustration showing the geometry which uses a gap size of 150µm.....	76
<b>Figure 34.</b> Picture of whole apparatus and close up of the platinum du Nouy ring.....	78
<b>Figure 35.</b> BD 10ml syringe and Jensen Global 0.21mm I.D. nozzle used. Jensen dispensing tips feature a polypropylene Luer Lock hub with a UV-bonded 304 stainless steel cannula.....	81
<b>Figure 36.</b> Geometry with 0.254mm radius nozzle and 0.7ml hydrogel to decrease total elements, all angles are 90 degrees.....	81
<b>Figure 37.</b> Boundaries of the 2-D axisymmetric geometry.....	81
<b>Figure 38.</b> Most basic mesh with 4 elements across the nozzle radius, total elements=13,283.....	82
<b>Figure 39.</b> The basic geometry, 90° corners are shown, but simulations were performed to examine a range of wall angles while maintaining the dimensions of the inlet and the outlet as well as the distance between inlet and outlet.....	83
<b>Figure 40.</b> The tapered syringe design and the cone shaped nozzle geometry, each with same inlet and outlet dimensions.....	83
<b>Figure 41.</b> (a) Medical image from CT scan is adapted with Rapidform into a Solidworks file before converting into a printable file format, (b) complete aortic root in Solidworks software showing the boundary surface and omitted coronary arteries (c) patient specific geometry file for 3D printing software, truncated for print quality.....	85
<b>Figure 42.</b> Biaxial stretching system; molded sample of crosslinked hydrogel; close-up of cuboid testing sample attached to prongs.....	87
<b>Figure 43.</b> BioBots beta version 3-D bioprinter.....	88
<b>Figure 44.</b> First and second layers matching flow rate of hydrogel to the print velocity and the print cross-sectional area. A slight difference always exists between the first layer profile and the rest of the layers.....	90

<b>Figure 45.</b> The g-code designs the pattern of motion for each layer.....	91
<b>Figure 46.</b> Effects of LAP concentration and UV light exposure time, 365 nm and 410 mW/cm <sup>2</sup> .....	94
<b>Figure 47.</b> The best hydrogel has shear thinning behavior as shown. A curve is well fit to the viscometry data using the formula shown for Power Law fluids.....	96
<b>Figure 48.</b> The best hydrogel in context of its component molecules and their viscosities.....	97
<b>Figure 49.</b> The surface tension of a 2% w/v HPMC hydrogel on a dime for illustration of the interfacial forces in room air and temperature. ....	98
<b>Figure 50.</b> 99% of pressure drop. Most of the pressure is lost due to the length of the nozzle and not the syringe. Top shows the contours for 100 % of the $\Delta P$ while the bottom shows 99% of the $\Delta P$ , that 70,000 Pa and 69,300 Pa respectively.....	101
<b>Figure 51.</b> The hydrogel extrusion flow pattern pathlines colored by velocity magnitude.....	102
<b>Figure 52.</b> The different geometries tested and the pathlines colored by velocity magnitude, same scale for figures (b) - (f). Notice the similar flow speeds under each design and the preservation of the no-flow corner between the walls adjacent to the constriction.....	103
<b>Figure 53.</b> The wall shear stress maximum which occurs at the entrance length of the nozzle.....	104
<b>Figure 54.</b> The strain rate across the outlet is interesting because it linearly increases from the center to the wall for Newtonian fluids.....	105
<b>Figure 55.</b> The velocity contours, maximum velocity shown in red is 8.73 mm/s.....	105
<b>Figure 56.</b> The pathlines colored by velocity magnitude.....	105
<b>Figure 57.</b> The velocity vectors as the hydrogel accelerates into the nozzle and reaches a fully developed state after 78 microns.....	106
<b>Figure 58.</b> The preliminary Q vs P graph showing experimental, CFD and analytical results.....	107
<b>Figure 59.</b> The post processing graph show the simulation results after adjusting the viscosity to match the CFD simulation to the experimental P and to the experimental Q.....	107
<b>Figure 60.</b> The outlet velocity profile is parabolic and follows H-P as long as the viscosity is constant.....	109
<b>Figure 61.</b> The comparison of a Newtonian simulation and the Power law simulation with k=4 and n=0.52.....	109
<b>Figure 62.</b> (a) Complete aortic root in Solidworks showing the boundary surface and omitted coronary arteries, (b) complete file imported for printing exceeds current print area, (c) patient specific geometry file for 3D printing software, truncated for print quality.....	111

<b>Figure 63.</b> Mechanical properties of scaffold materials.....	113
<b>Figure 64.</b> Raw data in graphical form from the biaxial stretch test results.....	115
<b>Figure 65.</b> The properties of scaffolds after crosslinking compared with native tissue shows the relative disorganization of the scaffolding provisional matrix for cell seeding.....	116
<b>Figure 66.</b> Aortic scaffold being printed under 365 nm UV light with intensity of 410 mW/cm <sup>2</sup> ; finished scaffold from two angles, 15 % PEGDA 2% HPMC w/v.....	117
<b>Figure 67.</b> Thin walled scaffold printed with thickness between 0.4mm-0.8mm, and dimensional fidelity is +/- 2% with several dramatically overhung features. Gelatin 5% -PEGDA 15% w/v copolymer.....	117
<b>Figure 68.</b> Aortic valve scaffolds from separate prints of 2% HPMC and 10% PEGDA 700.....	118
<b>Figure 69.</b> Aortic valve scaffolds from separate prints of 5% gelatin and 10% PEGDA 700.....	118
<b>Figure 70.</b> Aortic valve scaffolds from early testing with testing with alginate-PEGDA copolymer hydrogels.....	119
<b>Figure 71.</b> There are real phenomena when the print settings are wrong.....	119
<b>Figure 72.</b> The extrusion can be configured such that the material crosslinks before contacting the print bed and thus creates a long elastic thread.....	119
<b>Figure 73.</b> The Kayes effect is a product of the shear thinning behavior as the fast moving stream has low shear stress when it moves through the bulk material.....	126
<b>Figure 74.</b> The Weissenberg effect is also due to the shear thinning behavior and shows dramatic contrast to Newtonian behavior.....	126
<b>Figure 75.</b> The Barus effect changes the cross-sectional area as flow leaves the nozzle, slowing its average velocity and affecting the print settings <sup>6</sup> .....	126
<b>Figure 76.</b> First layer, matching nozzle flow rate, $V_1 * A_1$ , with print speed, $V_3$ , by examining the cross sectional area, considering die swell, and using the law of continuity.....	127
<b>Figure 77.</b> Top, fracture of PEO-PEGDA copolymer hydrogel at 22% Green strain. Right, biaxial stretch data plot compared with human aortic tissue.....	146
<b>Figure 78.</b> Top, fracture of Gelatin-PEGDA (5-15% w/v) copolymer hydrogel at 3% Green strain. Right, biaxial stretch data plot comparing concentration of PEGDA 700 at 10% and 15% w/v....	147
<b>Figure 79.</b> Top, fracture of Alginate-PEGDA (4-15% w/v) copolymer hydrogel at 4% Green strain. Right, biaxial stretch data plot comparing the effect of concentration of PEGDA 700 and alginate on the mechanical properties. ....	148

## LIST OF ABBREVIATIONS

2PP – Two-photon polymerization

ATP – Adenosine triphosphate

cAMP – cyclic adenosine monophosphate

CFD – Computational fluid dynamics

CT – Computed tomography

DIW – Direct ink writing

DMEM – Dubecco's modified eagle medium

ECM – Extracellular matrix

FBGCs – Foreign body giant cells

FBS – Fetal bovine serum

FDM – Fused deposition modeling or FFF – Fused filament fabrication

FGF – Fibroblast growth factor

GAG – Glycosaminoglycans

HA – Hyaluronic acid

HPMC – (Hydroxypropyl)methyl cellulose

ICE – Ionic covalent entanglement

IPN – Interpenetrating polymer network

IR – Infrared light

Irgacure (I2959) - 2-hydroxy-1-(4-(2-hydroxyethoxy) phenyl)-2-methyl-1-propanone

LAP – Lithium phenyl-2,4,6-trimethylbenzoylphosphinate

LDL – Low density lipids

LDM – Low temperature deposition modeling

NSF - *N*-ethylmaleimide-sensitive factor

PAA – Poly(acrylic acid)

PAM – Pressure assisted microsyringe

PCL – Poly(caprolactone)

PDGF – Platelet derived growth factor

PEG – Poly(ethylene glycol)  
PEGDA – Poly(ethylene glycol) diacrylate  
PEO – Poly(ethylene oxide)  
PGA – Poly(glycolic acid)  
PLA – Poly(lactic acid)  
PMMA – Poly(methyl methacrylate)  
PMNs – Polymorphonuclear leukocytes  
PU – Polyurethane  
RGD - Arginylglycylaspartic acid  
ROI – reactive oxygen intermediates  
RP – Rapid prototyping  
SLA – Soft lithography  
SLS – Selective laser sintering  
SMCs – Smooth muscle cells  
SNAREs – Soluble NSF attachment protein receptors  
TAA – Thoracic aortic aneurysm  
TE – Tissue engineering  
VECs – Valvular endothelial cells  
VEGF – vascular endothelial cell growth factor  
VICs – Valvular interstitial cells

## CHAPTER 1: INTRODUCTION

Numerous surgical implants for the vascular system are grafted into patients across the world each year. The current implant choices are autografts, allografts, xenografts, synthetic grafts and tissue engineered grafts. While there are examples of viable options in each category, the availability and the long term patency make tissue engineered grafts the most promising choice for the future. Tissue engineered grafts possess the benefits of the cellularization and the compatibility of autografts with the availability and customization of synthetic grafts. In concert with the boom in 3-D printing technologies, the progressive research in tissue engineered vascular grafts (TEVG) has increase substantially and many experimental results show the reality of this bioengineering concept.

Before presenting laboratory work, the biology of native vasculature is discussed and related to the specific work of tissue engineering research and methods. Understanding the histology and the formation of native tissue uncovers the natural extracellular matrix (ECM) fabrication and helps illuminates the governing principles of tissue engineering a blood vessel. Furthermore, understanding the polymer technology and fabrication methods used in biomedical implants provides feedback about real experimentation. A complete report on laboratory research is then provided to demonstrate the intricacies of fabricating a scaffold for TEVGs.

The structure and morphology of the human circulatory system is determined by the mechanical demands on each part of the circuit. Where the highest pressure exists there are

thick artery walls or highly organized matrices of elastic fibers in the aortic leaflets, while the locations with lower pressures have thinner walls or matrices of elastic fibers in the pulmonary leaflets. In some senses, this is obviously a good natural design but it demands a closer evaluation to understand why the morphology is so sensible. A review of the vessel and valve anatomy will introduce the context to understand the forces that structure the morphology of the cardiovascular system. Furthermore, comprehension of the dynamics shaping generation and regeneration within the cardiovascular system is the best foundation to understand the function and outcomes related to cardiovascular implants. With a thorough understanding of the human anatomy and cellular biology, the use polymers as cardiovascular grafts and medical implants is justified. Finally, the parts come together to project the future of improved cardiovascular grafts and the practicality of research in 3D printing scaffolds for tissue engineering.

The vascular wall has layers that are each composed of an extracellular matrix adhering cells, which is designed by the mechanical environment and biochemical signals. As vascular walls develop from infancy the endothelial layer shapes first, building into the muscular and collagen rich layers over time. As these layers develop, the cells express a phenotype based on where they reside, i.e. the mechanical and biochemical cues of the specific region. In this sense, the natural environment shapes cell expression and cells engineer their surrounding connectivity based on the movement and atmosphere of their residence. The cells within the vascular walls are constantly degrading and newly synthesizing collagen and materials for the ECM. By using the cells as the engineers for TE, we can design a scaffold that is a perfect garden for them to work and then let them build their own ECM.



Since the design is to use cells to synthesize and polymerize the final structural matrix of the aortic graft, our job is to craft the ideal dynamics for the cells to adhere, and construct a

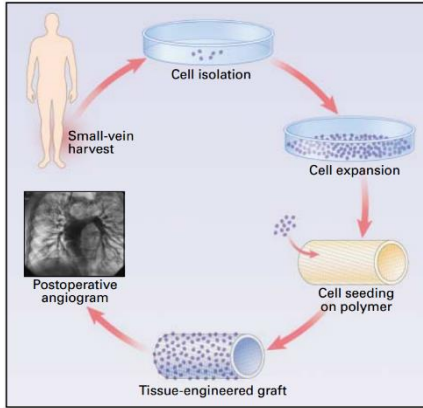


**Figure 1. The Tissue Engineering Technique** <sup>1</sup>. Reproduced with permission, Copyright Massachusetts Medical Society.

robust ECM as quickly as possible. From a mechanical engineering standpoint, the focus is on the pressure based extrusion of a particular composition hydrogel. Using viscometry and surface tension data to inform extrusion settings and efficiently optimize the print settings my achievement was 3-D bioprinting a hydrogel into a patient-specific geometry with difficult features to fabricate by any conventional method. Computational simulations were used to characterize the flow rate and

pressure relationship for accurate nozzle-based extrusion, however it is complicated for most hydrogels due to their non-Newtonian behavior. Finally, the mechanical properties of the crosslinked scaffolds provide further insight to achieve the goal of creating an optimal scaffold material. In working through this research, the flow and mechanical properties of the hydrogel and scaffold are well characterized and comprise a sound contribution from a mechanical engineering perspective to this multi-disciplinary work.

The connection between ultimate performance of the scaffold in a bioreactor and the fabrication is yet to be definitively established, but the purpose of this work is to empower the TE designer to be able to iterate through various hydrogels while efficiently updating print settings for new gels, and to be able to iterate through different mechanical properties to find out what scaffold properties are best for cells to adhere and to quickly engineer the ECM.

Motivating this work is the promise of helping children and those recipients that will benefit enormously if their vascular graft can grow and adapt with their own body. A cutting edge implant from 2001 created by the tissue engineering technique and Shin'oka et al.<sup>1,16</sup> was successfully implanted into the pulmonary root of a young patient, the patency was reported for at least 5 years post-operatively. Additionally, there is a huge deficiency for small diameter vascular grafts that maintain long-term patency, which has driven a great deal of the research over the past 20 years in small diameter TEVGs. While many applications remain viable for TE, it is vascular tissue engineering that holds particular promise for economical, functional and practical use in patients. With more time, it appears that tissue engineered grafts will become the gold standard for vascular grafts.

## CHAPTER 2: VASCULAR SYSTEM

The cardiovascular system performs the remarkable mechanical task of continuously circulating nutrient infused blood without respite. The cardiovascular system is comprised of the heart, the arteries, the capillaries, the veins and the valves. These elements work in harmony to efficiently circulate blood in one direction as a pulsatile flow. The cellular anatomy of the human cardiovascular system is complex, however simpler for the blood vessels and valves than for the myocardium. The circulatory system is modeled in the embryonic phase of life by genetics but as systemic growth progresses the morphology of the system reflects the responses of local cells to mechanical forces acting upon it as well as the biochemical cues from the body. Owing to covalent bonding between proteins tethered to the cell membrane and the molecular structure of the ECM, the cells are able to sense any mechanical strains in the ECM. As cells respond to their environment, the degradation and synthesis of new extracellular matrix is tuned to maintain a range of mechanical strain to the cell<sup>17</sup>. This direct feedback loop creates the anatomical circulatory system that is tailored to each region and particular to its place in the circuit. Vessels are gauged by the pressure and flow rates across their length, which is illustrated by the wide range of vessel diameters and wall thickness found across the circuit. The differences between arteries, arterioles, venules and veins arise from the different amounts of ECM established in each layer of the vessel and the populations of cells within each layer, which serves to point out that all vessels have the same basic design of layers and the thickness of the

layers is determined by pressure and wall shear. By designing a circulatory system that is shaped by local flow conditions nature is able to construct a flow loop that is phenomenal.

The function of the vascular system is dependent on elasticity of the vascular wall. Without passive energy storage and recovery, the circulatory system would require far more power to operate. The elasticity of all vessels is largely due to highly organized collagen fibrils. Collagen molecules are the nature engineered polymer of vascular interstitial cells (VIC). Stronger than steel by cross-sectional area, collagen is a miraculous elastic fiber that facilitates life on earth. Working constantly to adjust the ECM, VICs use the high quality properties of collagen to effectively adjust the mechanical strain of their surroundings, and therein the mechanical energy storage during pulsatile circulation. From a histology standpoint, the valves are comprised of collagen with select glycosaminoglycans (GAGs) and elastin fibers, the vessel contain similar molecules in lower concentrations by volume. The human circulatory system is reliant on local cellular response to mechanical and biochemical conditions to optimize ECM synthesis and degradation, but owes its elastic performance to the outstanding properties of the well-organized ECM, which is mostly collagen, synthesized by resident cells.

This work focuses on the aortic root and treatment of ascending aortic aneurysms. While these are not likely to work as vascular grafts, there is potential that after TE develops better small diameter grafts there will be enough progress to replace Dacron implants in this role. Currently Dacron far exceeds the performance of all other aortic grafting options.

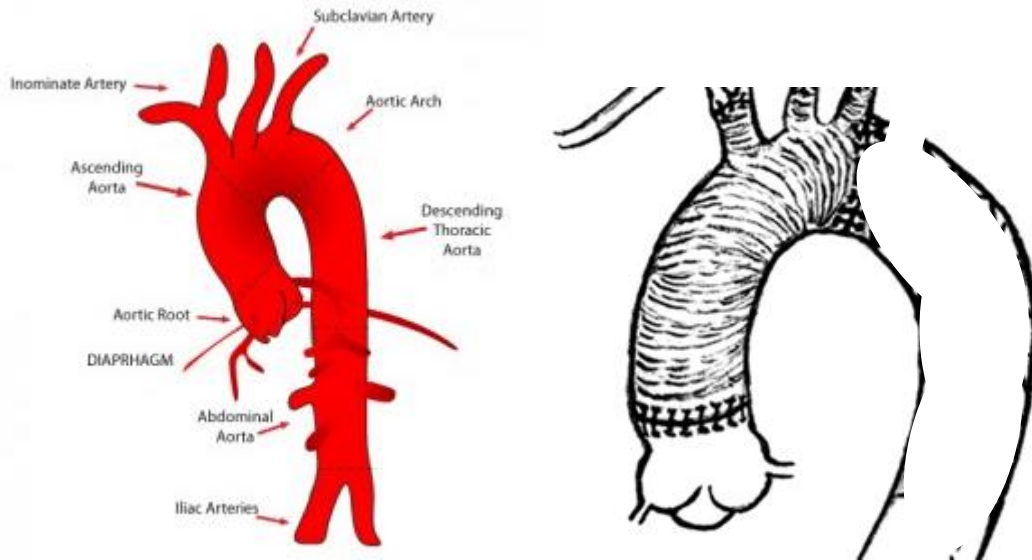


**Figure 2. Complete aortic root and a depiction of an ascending aortic graft with bifurcations. With permission from Aorticdissection.com.**

## Vessels

Native vessels are comprised of four layers: tunica intima, tunica media, adventitia, and vasa vasorum. These layers are separated by thin layers of connective tissue that give a foundation for cell attachment and subsequent cell mobility. Within the vessel layers there are various types of cells: endothelial cells, smooth muscle cells (SMC), mesenchymal cells, and interstitial cells. The tunica intima has a layer of endothelial cells and a layer of connective tissue, called the internal elastic lamina that separates the inner layers. Smooth muscle cells are circumferentially arranged throughout the tunica media with collagen, elastin lamellae and ground substance. The external elastic lamina separates the outer layers, fibroblasts and collagen dominate the adventitia but elastin and macrophages are also present. The vasa vasorum lines the outside of the adventitia and circulates oxygen to the thick vessel walls where passive diffusion does not extend through the thickness. Endothelial cells are localized on the

inner surface and SMCs are found predominately in tunica media while mesenchymal cells and interstitial cells are more dispersed.

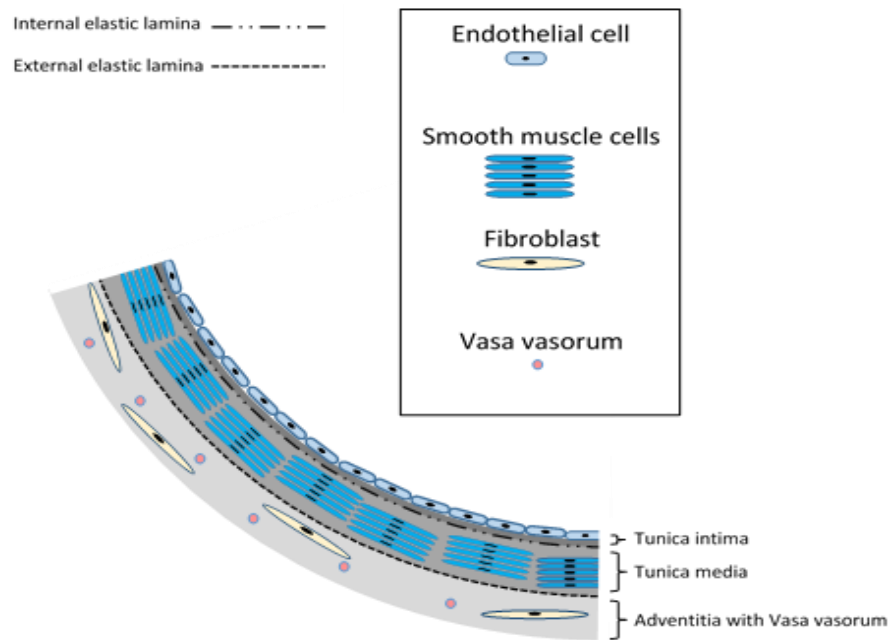


**Figure 3. The vascular wall contains three prominent layers held together with connective tissue lamina. Different cells types reside in each layer of the vessel wall. The aorta has its own circulatory system called the vasa vasorum designed within the adventitia layer traversing with nerve connections throughout the vessel wall.**

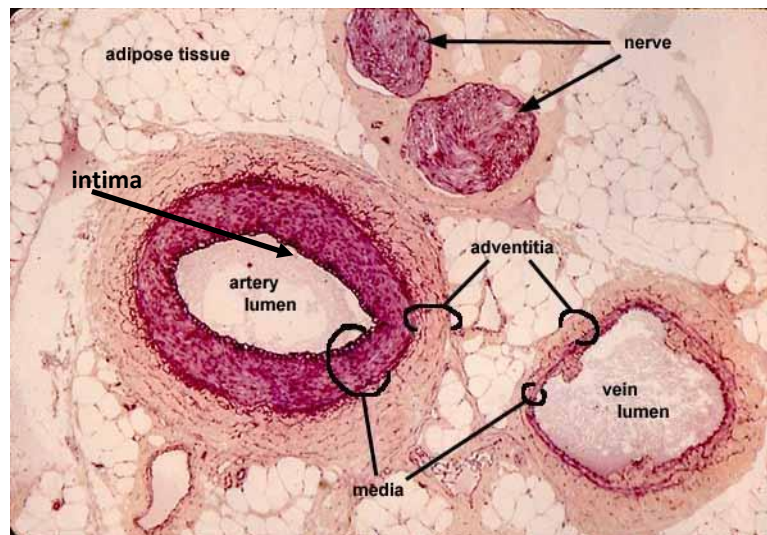


**Figure 4. Human artery and vein under microscopy. With permission from Anatomybox.com.**

The extracellular matrix (ECM) in its natural form is a matrix of collagen, elastin, fibronectin, laminin, proteins, proteoglycans, glycosaminoglycans, growth factors, cytokines and other biological molecules produced by cells that form the structural and functional components of all soft tissues in the body<sup>13,18-22</sup>.

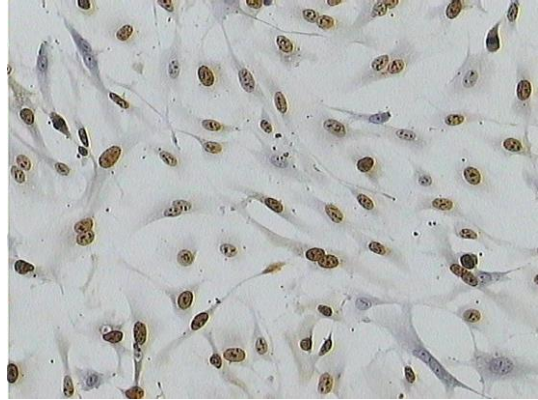


**Figure 5. Human Umbilical Vein Endothelial Cells, Nature 511 312-318.**

The ECM serves as a structural scaffold with molecular sites to orient cells, and communication portals that provide a means for cells to communicate via signaling factors to regulate a variety of molecular functions. The ECM controls the reaction to injury and serves as an inductive scaffold for tissue repair and regeneration. Cadherins are well researched and play a major role in the connections built between adjacent cells<sup>23</sup>; integrins play a major role connecting the cytoskeleton within cells to the ECM outside of the cell membrane<sup>24</sup>. Lipids, proteins and carbohydrates, and glycosaminoglycans are also incorporated into the ECM. The histology of blood vessels is highly dependent on their location within the body and the associated mechanical and chemical signaling cues received by the cells, which directs the adhesion of molecules from the ECM, the synthesis and secretion of molecules produced from within the cells, and also the degradation and adaptation of the existing internal and external cytoskeleton. This cascade of signaling originates from the endothelial layer of cells<sup>25-28</sup>, which are in direct contact with the flow conditions and the blood composition within the vessel interior. The endothelial layer is shown in the figure above and illustrates the tightly packed formation of the VECs in order to create a surface that is smooth and completely covers the internal lamina. Improper endothelialization is shown to be a major factor in immune

response by the body because the blood reacts and attaches proteins to practically anything except VECs, which have an active communication with the blood.

Normal vascular development, including the growth and differentiation, is a result of the balance between stimulators and inhibitors of vascular cell processes<sup>29-32</sup>. The endothelia and basal lamina is all that starts a vessel in an infant, the endothelial cells signal the development and reaction of vessel walls to shear and pressure. Vascular smooth muscle cells and endothelial cells are the two major cells of the vessels. Potent mitogens basic fibroblast growth factor (bFGF), vascular endothelial cell growth factor (VEGF), and platelet derived growth factor (PDGF) each stimulate these cells in a specific manner to direct cell mitosis in one or both cell layers. Other growth factors are reported to stimulate or inhibit smooth muscle cell proliferation, depending on the cell density and growth factor concentration<sup>30,33,34</sup>. Therefore, the status of the tissue plays a huge role in the impact of growth factor action.

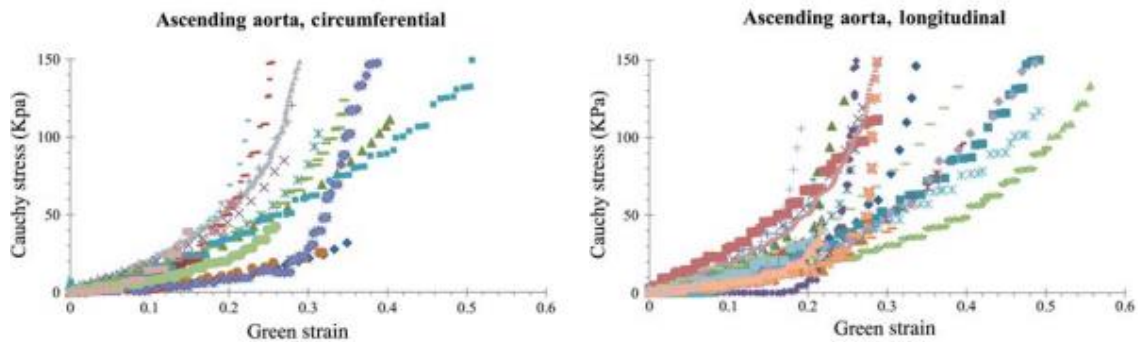


**Figure 6. Material properties of human ascending aorta from Azadani et al. 2013<sup>11</sup>.**



## Valves

With a highly dynamic job the valves further demonstrate the performance of collagen as an ECM protein<sup>12</sup>. Far thinner than the vessel walls, the valves have no smooth muscle cells and rely completely on the passive mechanical properties of the leaflets. The role of elastin is introduced because it conveys the higher elasticity demanded of the ventricle side of the aortic valve. Since the valves contain mostly cells for the synthesis of collagen, the valves are a fascinatingly simple demonstration of cells creating tailored, highly organized, polymerizations of collagen<sup>35</sup>.

Not unlike the vessel walls, the valves are comprised of layers, which react to the physical environment to appropriate mechanical function. The valve leaflets have 4 layers of tissue that reflect the optimal mechanical properties: arterialis, fibrosa, spongiosa and ventricularis. There is a lower cell density across the leaflets than observed in the vessels and the leaflets are predominantly an extracellular matrix (ECM) of collagen, select glycosaminoglycans (GAGs), and elastin fibers. Within the valve layers, endothelial cells, valvular interstitial cells and mesenchymal cells are found<sup>36</sup>. The figures show the layers and the mechanical forces that influence the cell behavior within the leaflets.

The ventricularis and arteriosa layers are lined with endothelial cells, which are differentiated on each aspect of the leaflets due to differing flow and pressure regimes. Below the endothelium is a basement layer of connective tissue. The ventricularis layer contains high elastin content to optimize recoil of the leaflets, while the arterialis layer contains a collagen basement layer to support the diastolic load on the valve. The fibrosa layer is a thin well-organized layer of mostly circumferentially arranged collagen molecules that provides tensile

strength. The spongiosa layer is an ECM that provides hydration and cushioning and it is rich in glycosaminoglycans<sup>35</sup>.

During valve development and maturation, fetal VIC have a myofibroblast-like phenotype, characterized by expression of specific growth hormones, and continuously remodel the ECM<sup>30</sup>. The cells become quiescent in the normal valve post-natally, suggesting progressive adaptation to the prevailing hemodynamic environment. Moreover, the cell density progressively decreases (by nearly 90%) throughout life<sup>37</sup>.

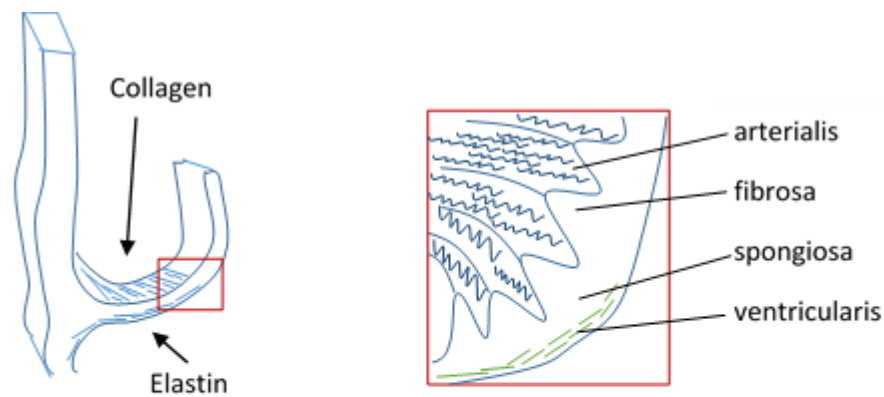


**Figure 7. The left side shows the aortic wall and aortic valve leaflets. The right side shows the specific layers and the crimping of collagen during systole due to bending. The arterialis of the leaflet contains circumferentially arranged collagen while the ventricularis contains radially arranged elastin and collagen fibers.**

The morphology of the valves reflects the physical stress from flow of blood through the valve and the closure of the valve to stop retrograde flow. The figure below depicts these two limit states, which are dramatically different. The shear forces during systole and the normal force on the valve during diastole are paramount influences on the action of VECs and VICs. Under each condition the thickness of the valve experiences different strains, which are communicated through the cellular junctions to actualize the synthesis or degradation of ECM to normalize strain within the valve.

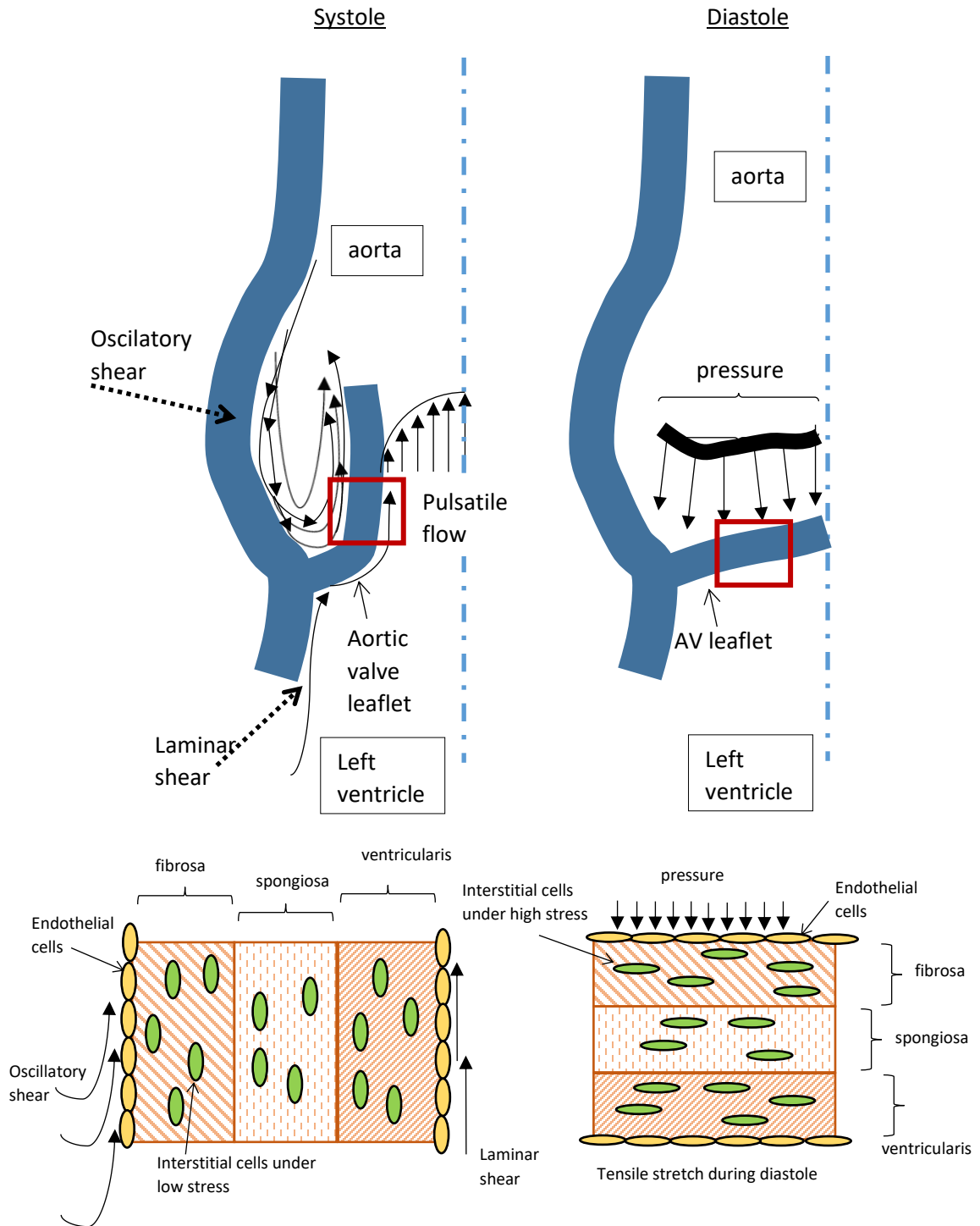


**Figure 8. The valve during systole and diastole illustrating the communication of mechanical forces to the cells.**

The ECM structurally supports the cells and is composed mostly of collagen. Collagen constitutes approximately 90% of the protein content of the valve insoluble matrix<sup>9</sup>. The vast majority of the valve's content is composed of collagens type I, III, and V. Together, these fibrillar collagens account for 60% of the valve's dry weight<sup>38</sup>. There is approximately 74% collagen type I, 24% collagen type III, and 2% collagen type V distributed throughout the valve<sup>39</sup>. Whereas collagen type I mainly exists in the fibrosa, collagen type III is expressed ubiquitously throughout all three layers<sup>40</sup>.

The valve histology emphasizes the role of collagen and elastin in the function of the vascular system. The primary, secondary and tertiary structure of collagen in particular shows the marvelous organization of this heteropolymer of amino acids. The performance of collagen is due to the combination of bonds that exist at each level. The covalent bonds of the backbone chain are precisely ordered, the hydrogen bonding between hydroxyproline groups conforms three fibers tightly together into a triple helix, and steric hindrance organizes the tropocollagen into a staggered array. The synthesis and construction of collagen fibrils is a critical function of valvular interstitial cells within the spongiosa and fibrosa layers.

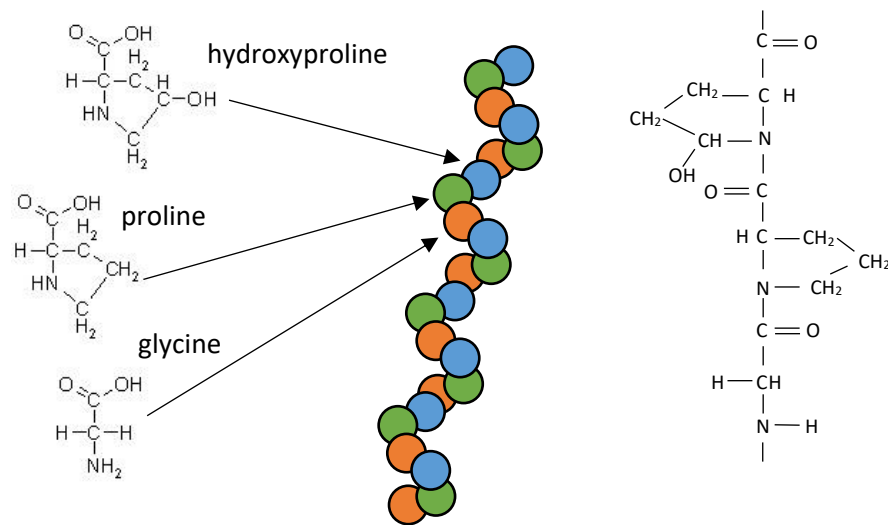
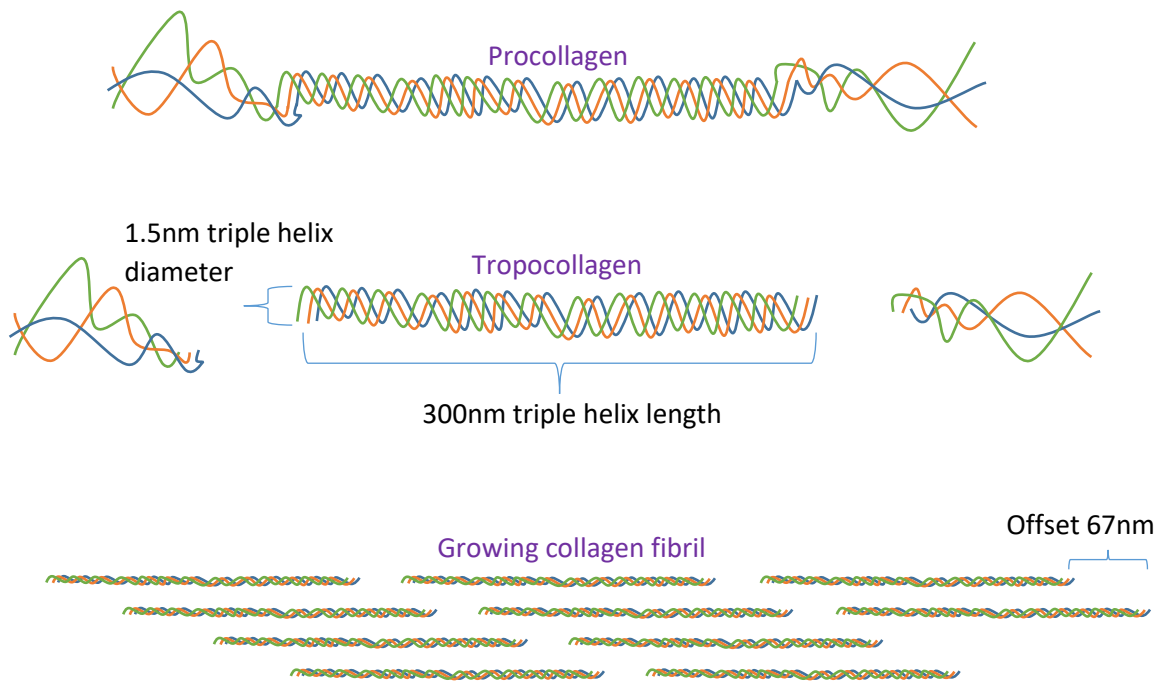


Figure 9. Primary molecular structure of collagen<sup>12</sup>.



**Figure 10. Collagen is assembled in the cytoplasm into tropocollagen, secondary structure, which is secreted into the ECM for assembly into well-organized fibrils, tertiary structure.**

The chemistry of steric hindrance, hydrogen bonding, hydrophobic bonding, van der Waals forces, and ionic bonds are all relevant to the extraordinary performance of collagen<sup>12</sup>. Compared to steel, which is currently used worldwide as a trustworthy building material, collagen is by far more impressive on a strength per fiber diameter basis.

Tropoelastin is the protein unit that comprises elastin and is itself made from glycine, valine and modified alanine and proline residues. Tropoelastin is a roughly 65,000 Da molecule that becomes highly crosslinked and forms an insoluble complex that is elastin, which consists of approximately 700 amino acids with a total molecular mass of 700 kDa<sup>41</sup>. Fibroblasts attached within the ECM of the media layer are responsible for synthesizing tropoelastin and constructing elastin polymers in the ECM. Elastin has less variation than collagen. It is a longer molecule and

is referred to as yellow, where collagen is white. There is only one gene for its synthesis and it decays over time, so running out of elastin content is an aging issue<sup>42</sup>.

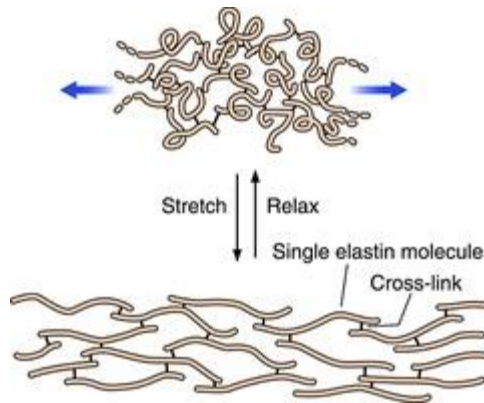


**Figure 11.** Elastin structure is much longer chains with a high degree of flexibility, reflected in the mechanical role that elastin plays in tissues<sup>13</sup>.

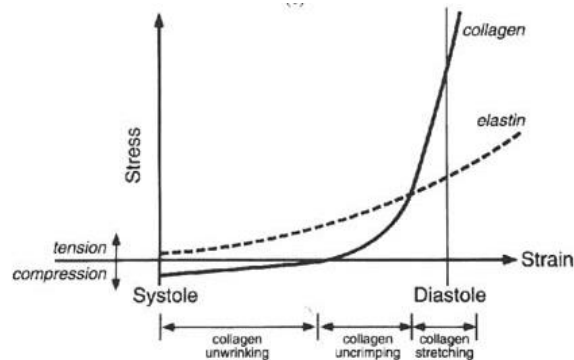


**Figure 12.** A depiction of the roles the two elastic ECM proteins play<sup>13</sup>. With permission from Schoen, F. J. and Levy, R. J. (1999), Tissue heart valves: Current challenges and future research perspectives. *J. Biomed. Mater. Res.*, 47: 439–465. doi:10.1002/(SICI)1097-4636(19991215)47:4<439::AID-JBM1>3.0.CO;2-O.

The figure above illustrates the complimentary roles that elastin and collagen play in the elastic behavior of the valve and also the vessels. Strain is easily accommodated by both materials initially, but as strain increases further collagen has a strong loading behavior and recoils energetically due to the triple helical tertiary structure and molecular interactions, hydrogen bonding between consecutive twists of the helix, which have a high affinity for the passive conformation of the helices. On the other hand, elastin can be strained further and

continues to stretch with relative ease due to the more random conformation of its long contorted chains with less regularity than collagen. Elastin provides the recoil for the leaflets to return to the close position after systole, which requires less force and a larger range of motion.

**Table 1. The uniaxial tensile mechanical properties of native and TE aortic valves<sup>9</sup>.**

	Young's modulus (MPa)	Ultimate tensile strength (MPa)	Strain at ultimate tensile stress (%)
Native circumferential	15	2.6	22
Native radial	2	0.4	30
Tissue engineered static	3	0.7	33
Tissue engineered dynamic	6	0.9	25
Unseeded scaffold	0.705	0.732	61
Tissue engineered conduit wall (1 week <i>in vivo</i> )	1.325	0.967	10
Unseeded control of the conduit wall (5 weeks <i>in vivo</i> )	1.279	0.955	9
Tissue engineered conduit wall (5 weeks <i>in vivo</i> )	0.487	0.838	88
Tissue engineered conduit wall (17 weeks <i>in vivo</i> )	0.140	0.648	101
Native pulmonary artery	0.040	0.385	91

## Aortic Aneurysms

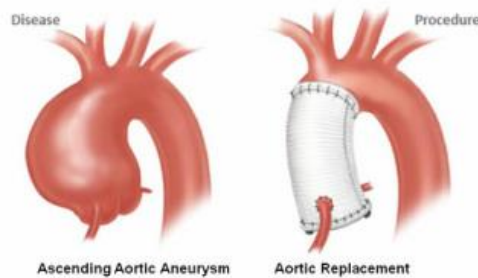


**Figure 13. Anatomy of aortic root and ascending aortic aneurysm<sup>14</sup>.**

An ascending aortic aneurysm is a focal dilation of more than fifty percent occurring in the vasculature of the ascending aorta below the arch. Ascending aortic aneurysms account for 15,000 deaths each year in the United States, making them a public health concern, particularly for those over the age of 55<sup>43</sup>. While visualized with ultrasound, aneurysms often go undetected for years lingering as a mortal risk upon rupture. Dramatically, rupture causes death in 2 out of 3

people before reaching the hospital; however, there can be positive outcomes if the aneurysm is detected before rupture and the diameter of the vessel is restored to normal. This is done surgically or with interventional techniques, both have good outcomes reflected in the 20-30 year life expectancy after open surgical repair or aneurysm graft<sup>44</sup>.

According to the American Heart Association, about 20% of AA patients have at least one relative with this condition, suggesting significant genetic factors. This points to the critical nature of proper ECM construction by the aortic vascular cells, and furthermore it accentuates the subtlety in proper ECM construction at the molecular level. Beyond genetic disposition, there are three scientific elements that must be understood in order to predict and evaluate aneurysms: the epidemiology of the aorta and branching vasculature, the inertial and chemical forces of blood, and the local pressure gradient. An insufficient local cellular response to changing flow conditions over time leads to the insufficiency of the aortic wall and hoop stress can eventually exceed ECM strength. Insufficient cellular reaction to mechanotransduction, inadequate cellular signaling between cells, low response to biochemical cues, high blood pressure, improper ECM synthesis and organization, and atherosclerosis can all contribute to aneurysm development among other pathologies.

The three layers of the aorta each play a role in the pathology of aneurysms: the *intima layer*, the *media layer* and the *adventitia*. The *intima layer* is a single layer of endothelial cells that provide feedback on flow conditions, adhere blood cells as needed and trigger restructuring of the vascular wall to meet demand. Thus shear rate, blood pressure, wall distress and blood chemistry each register with the intima layer, which then signals for the appropriate response. The *media layer* is substantial in the ascending aorta, full of smooth muscle it is held between the internal and external elastic lamina, which are comprised of elastin and collagen. If



atherosclerosis is present, the fatty deposits reside in the media layer creating a weakness in the smooth muscle, which reinforces, compounding the protrusion into the lumen. The *adventitia* is a non-muscular connective tissue layer that provides nutrients and nerve signals to the outer half of the media cells by the vasa vasorum and nervi vasorum, respectively. This implies a connection between wall thickness and nourishment, and wall thickness and nerve signaling<sup>45</sup>.

The Hagen-Poiseuille equation for resistance relates the resistance of a vessel to its radius, the flow geometry and the viscosity:

$$R_s = \frac{\Delta P}{Q} = \frac{8\mu L}{\pi R^4} \quad (1.1)$$

An increase of 10% of the aortic radius will decrease the resistance by almost 50%, and smaller vessels create dramatically more resistance than the aorta. Illustrated below are the pressure gradients across the cardiovascular circuit. We notice that most pressure is converted within the small arteries and arterioles, which propagate pressure energy as flow velocity and it is dissipated as head loss due to viscosity and vessel diameter.

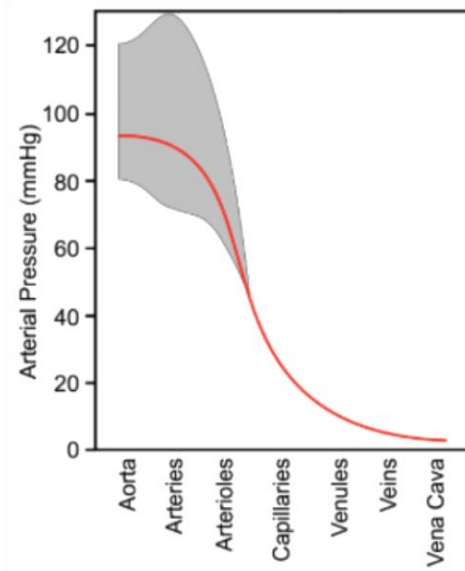


Figure 14. Blood pressure throughout the circulatory system<sup>73</sup>.

An existing aneurysm is influenced by the flow stasis within the bulb, which is problematic for plaque and thrombocytes activation; however, even small arterioles may provide sufficient flow out of bulb to prevent mural thrombosis burden<sup>46</sup>. Beyond blood clots, the stasis within existing aneurysms creates cesspools of misguided cellular activity that leads to further negative feedback exacerbating the problem of wall deterioration and elastin-collagen elongation<sup>47</sup>.

Within an abdominal aneurysm the flow of blood is described by particle resident times and is estimated as 4 seconds to clear 97% of particles, according to CFD analysis of 8 males with AAA<sup>48</sup>. This represents a scientific measure of energy conversion as entering particles displace resident particles and then become resident, then subsequently move into the flow pattern regaining kinetic energy. This explains a portion of the energy inefficiency due to an aneurysm.

Viscosity of blood plays a few roles in aneurysms. It contributes linearly to resistance, it is detrimental to the vessel walls as a source of atherosclerotic building blocks, and it is harmful within the residential region of the aneurysm. Blood cells and large molecules tend to stay towards the central flow, which can create displacements of plasma into the early arterioles while a thickening flow descends the aorta. This is one reason atherosclerosis is commonly seen in the distal region lining the branches as they leave the abdominal aorta.

In early formation as well as rupture prognosis of abdominal aneurysms the degradation of the cell wall by atherosclerotic plaque directly reduces yield strain, which is a major risk if stress increases above the yield level. However, non-local downstream atherosclerosis increases pressure locally, which is a main factor in aneurysm formation and potential rupture.

Among all factors, the American Heart Association states that blood pressure is the highest sensitivity factor in aneurysm rupture. Likewise, aneurysm formation correlates with high blood pressure and also depends on atherosclerosis, high cholesterol, and elevated peripheral resistance. The pressure gradient across the arterioles increases due to an aneurysm and this may cause secondary problems for normal arterioles, in particular the renal artery, which is highly sensitive to pressure.

When a vessel radius doubles, then the velocity will decrease by 4 fold, and the pressure will increase by the absolute magnitude of kinetic energy loss. The pressure energy within the aorta pushes normal to all surfaces and creates hoop stress in the vessel wall. This is balanced with the tension in the elastic and smooth muscle layers of the aorta.

Hoop stress is described by LaPlace's equation for thick and thin-walled cylinders. Relating the previous equations, when radius doubles the hoop stress will more than double, due to the coincident increase in pressure. It is important to consider aneurysm shape in addition to size, which is not accounted for in the hoop stress equation.

$$\sigma_{\theta} = \frac{P R_1^2}{R_2^2 - R_1^2} \left(1 + \frac{R_2^2}{r^2}\right) \quad (1.5)$$

$$\sigma_{\theta} = \frac{\text{Pressure} \times \text{Radius}}{\text{Thickness}} \quad (1.6)$$

The circumferential stress results in variable levels of strain depending on the particular region of the aneurysm. In addition to mechanical stiffening of the vessel wall, the ECM The Young's modulus for ascending aortic aneurysms tissue is shown below.

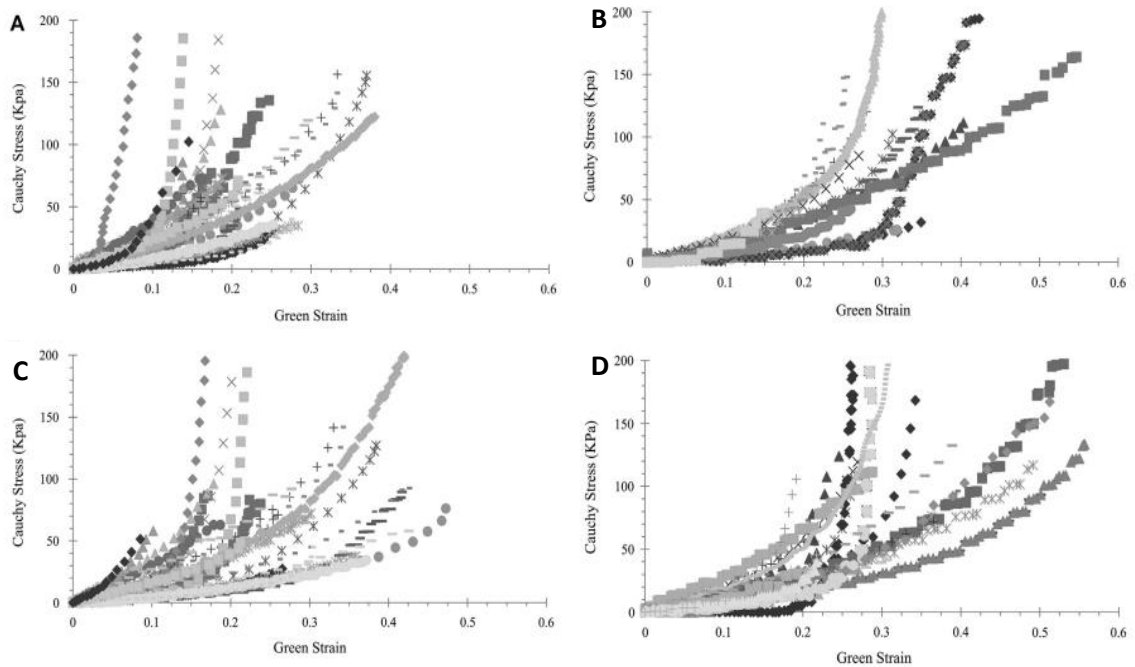


**Figure 15. Material properties of aneurysm and normal tissue from the wall of the ascending aorta, Azadani et al 2013<sup>15</sup>. (A) Aneurysm tissue circumferentially (B) normal tissue circumferentially (C) aneurysm tissue longitudinally, (D) normal ascending aorta tissue longitudinally.**

Different regions of the aneurysm have different yield stress, yield strains, and other mechanical properties, and this must be considered in understanding where the rupture might occur. Maximum stress is a better predictor of rupture risk than diameter. Focal stress areas and anisotropic wall tissue are factors deciding the exact location of rupture within the aneurysm. Each of these material factors is used to understand the compliance of the vessel wall to blood pressure and find the point of least resistance where rupture will occur.

A 2011 Mayo Clinic study stated that a 1 cm larger initial diameter was associated with an approximately 50 percent increase in the adjusted rupture risk. Due to conservation of mass, the Poisson ratio is pertinent: the increase in diameter will decrease the vessel thickness, local collagen molecules will extend further and elastic properties will be diminished, meaning that yield strain is closer to preconditioned length.

In medically addressing aneurysms, two methods of repair are most common: interventional radiology and open surgery. Both resolve the pressure increase due to the aneurysm by restoring the artery diameter using a graft within the lumen.

Interventional radiology uses the femoral artery as the access point and using a catheter, the graft is positioned and expanded into the aorta. This creates a conduit that passes blood flow through the aneurysm without interruption. Endurant from Medtronic is one example of an endovascular graft, introduced in 2008 it has been implanted in 150,000 people worldwide with no catastrophic results<sup>49</sup>.

Open surgical repair provides a similar conduit for flow within the artery. The graft is sutured end-to-end to the artery at the inlet and outlet, while the surrounding aneurysm is cleaned and sutured back together around the graft. Plaque is removed from the area during open surgery, it is not removed during interventional radiology. Ultimately the best solution for ascending aortic aneurysms is endothelialized synthetic grafts due to the demographics of patients needing the grafts and the mechanical demands on the ascending aorta. Tissue engineered grafts have not shown appropriate mechanical properties on the order of 1,700 mm Hg burst pressure to function reliably in this role, however Dacron grafts have performed well for decades as function ascending aortic grafts.

## Cells

At the cellular and molecular levels there are important facts that inform tissue engineering decisions. While much of the intracellular content is beyond the scope of this work, the cytosphere has a communication network which is critical to understand. The ability of

vascular walls to receive and send communications between cells directly is the critical component defining a tissue as an organized collection of cells. Cells and their membranes with an array of attachment proteins are designed to attach within the ECM and empower cells to migrate and remain mobile while sensing mechanical forces exerted on the molecular frame of the ECM. Affixed to the ECM and interconnected, the cells are able to respond in harmony to chemical, physical, thermal, electrical, magnetic, and light changes. As well, the passive and active diffusion of nutrients and factors from the extracellular space connects the response of the cells to the entire systemic state of being. The responses to synthesize more ECM or to degrade the ECM are controlled by several modes: the current molecular structure of the ECM, the response of cell membranes to local ECM strains, the intercellular communication through cell junctions, and the passive and active diffusion from the extracellular space<sup>50</sup>.

The dimensions of vascular cells vary but their diameter is between 10-30  $\mu\text{m}$ . The Smithsonian has recently published an estimation that there are  $1 \times 10^8$  vascular cells in a human adult, and 37 trillion cells in the entire body. While these figures have normal variation across the population it puts the abundance of cells into perspective. Each microscopic cellular unit must perform its job and the marvel of life becomes the result. There are clear conclusions about the effects of the decreasing cell population as human age, and the obvious extrapolation that cell density relates to the capacity for vascular cells to synthesize and degrade the ECM for normal function as well for TE.

Organization of cells takes three main forms in the body, Gap junctions, tight junctions and desmosomes. Gap junctions are channels that allow ions, sugars, amino acids and other small molecules or communication to pass between two adjacent cells. Tight junctions of the intestines, kidneys, epithelium of skin and they are zipperlike junction between cells.

Desmosomes are found in the stomach, bladder and heart because of their elastic properties. These junctions are formed by cytoplasmic plaque that binds adjacent cells with keratin giving a strong yet elastic network.

Glycoproteins are rooted in the cell membrane with the protein and have attachment sites on the homodimer cadherin outstretched into the ECM. Integrins, selectins, and cadherins are each related to these outstretched glycoproteins and each play a role in tethering the cell to the surrounding environment. These outstretched molecules provide sites for covalent bonding with various parts of the ECM, basal lamina, and other cells. It is also these attachment sites that must bond with a TE scaffold during cell seeding<sup>24,51</sup>.

In addition to the physical bonds the cells have with the vascular tissue, the cells are extensively connected by junctions that facilitate biochemical communication between cells. Beyond communication with each other, cells also receive chemical signal from passive and active transport through the cell membrane, this allows systemic controls on the vascular cells.

Some passive diffusion occurs through the phospholipid cell membrane, while other passive movement happens through the protein channels. Gases like oxygen and carbon dioxide pass through the plasma membrane by passive diffusion. Water molecules can pass the plasma membrane passively but the rate is slow because of the polarity of water molecules. Lipids, like steroid hormones, and lipid soluble molecules, like hydrocarbons, alcohols, and select vitamins, can all pass through the plasma membrane by diffusion. Small non-charged molecules, like  $\text{NH}_3$ , can also pass through the phospholipid bilayer. Ions, sugars, amino acids, small molecules, water (fastest by facilitated diffusion) are transported mainly by facilitated diffusion.

Active transport across the cell membrane which requires ATP, but can transport against the diffusion gradient. The Na/K pump (sodium-potassium channel) is important for creating the electrochemical gradient as three sodium ions are transported out and two potassium ions into the cell using one ATP phosphate bond dissociation energy. Endocytosis is a final method for crossing the cell membrane and phagocytosis is one example, pinocytosis for liquids and small dissolved molecules, and receptor-mediated endocytosis for low density lipids (LDLs)<sup>52</sup>.

There is a strong network that gives shape and improves transport within the cell itself known as the cytoskeleton. It is comprised of actin filaments, intermediate filaments and microtubules. The actin filaments are globular actin monomers as long chains in a double helix with 7nm diameter. Actin filaments are in microvilli and play helpful role in motor movement and the complex network inside the cell membrane surface. The intermediate filaments are 8-10nm diameter and are made of fibrous polypeptides.

Microtubules are one form of cellular highway that facilitates communication and transport within a cell. Their geometry is a small hollow cylinder about 25 nm in diameter and 0.2 – 25  $\mu\text{m}$  in length. These channels are commonly in the fibroblast cells of animal tissues and facilitate movement of granules, growth factors and other biomolecules. They are composed of 13 rows of alpha and beta tubulin dimers, which surround an empty core to create a sort of tunnel through the tissue. Chameleons rely on microtubules to quickly shift pigment granules within their skin cells. Microtubules can actively and passively move molecules within the cytosphere.



Microtubules (20-25 nm diameter channels), neurofilaments (10nm channels), and microfilaments (6nm filaments) create the frame of the cytoskeleton<sup>53</sup>. These three elements are involved in the transport, communication, and physical organization of all of the elements of cells. These threadlike structures organize the intracellular space with channels for

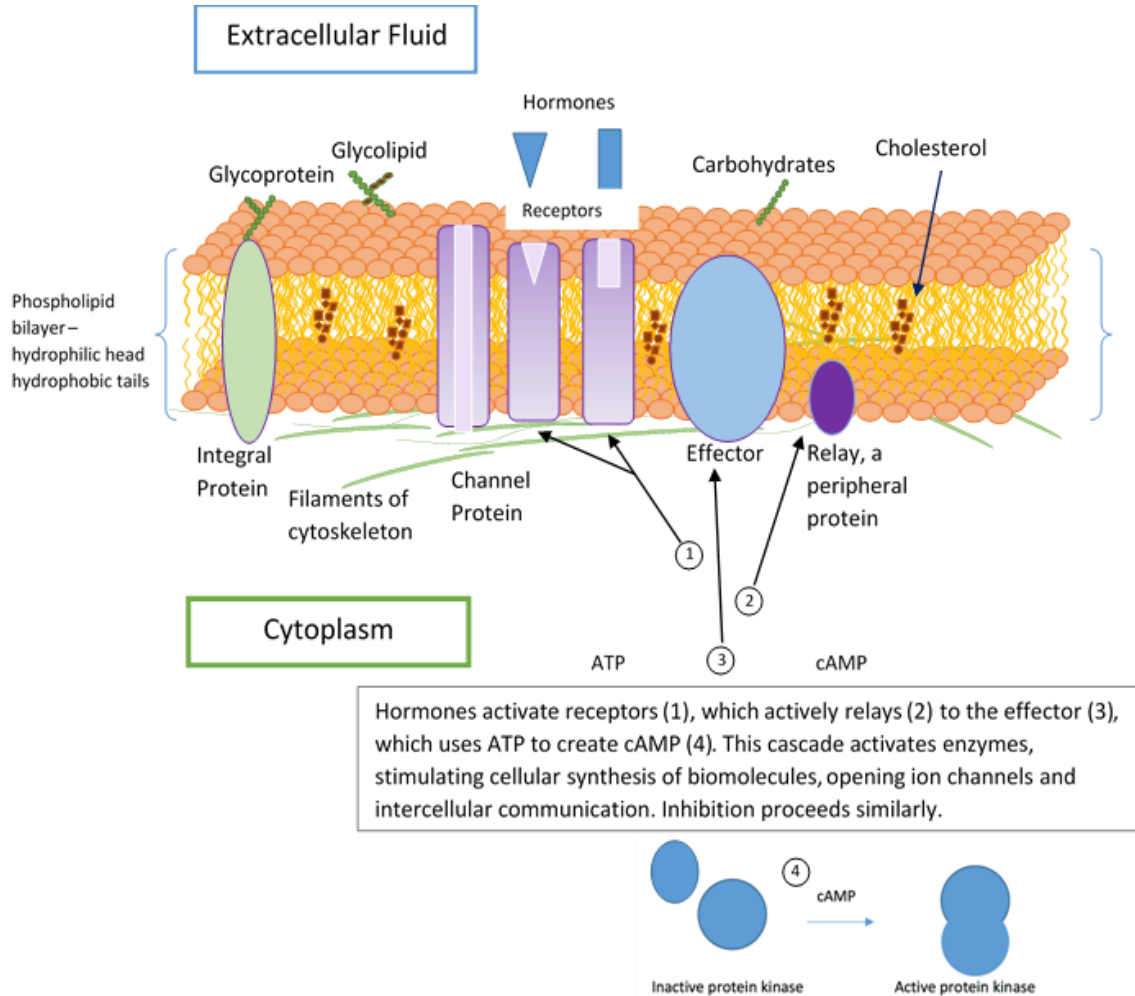
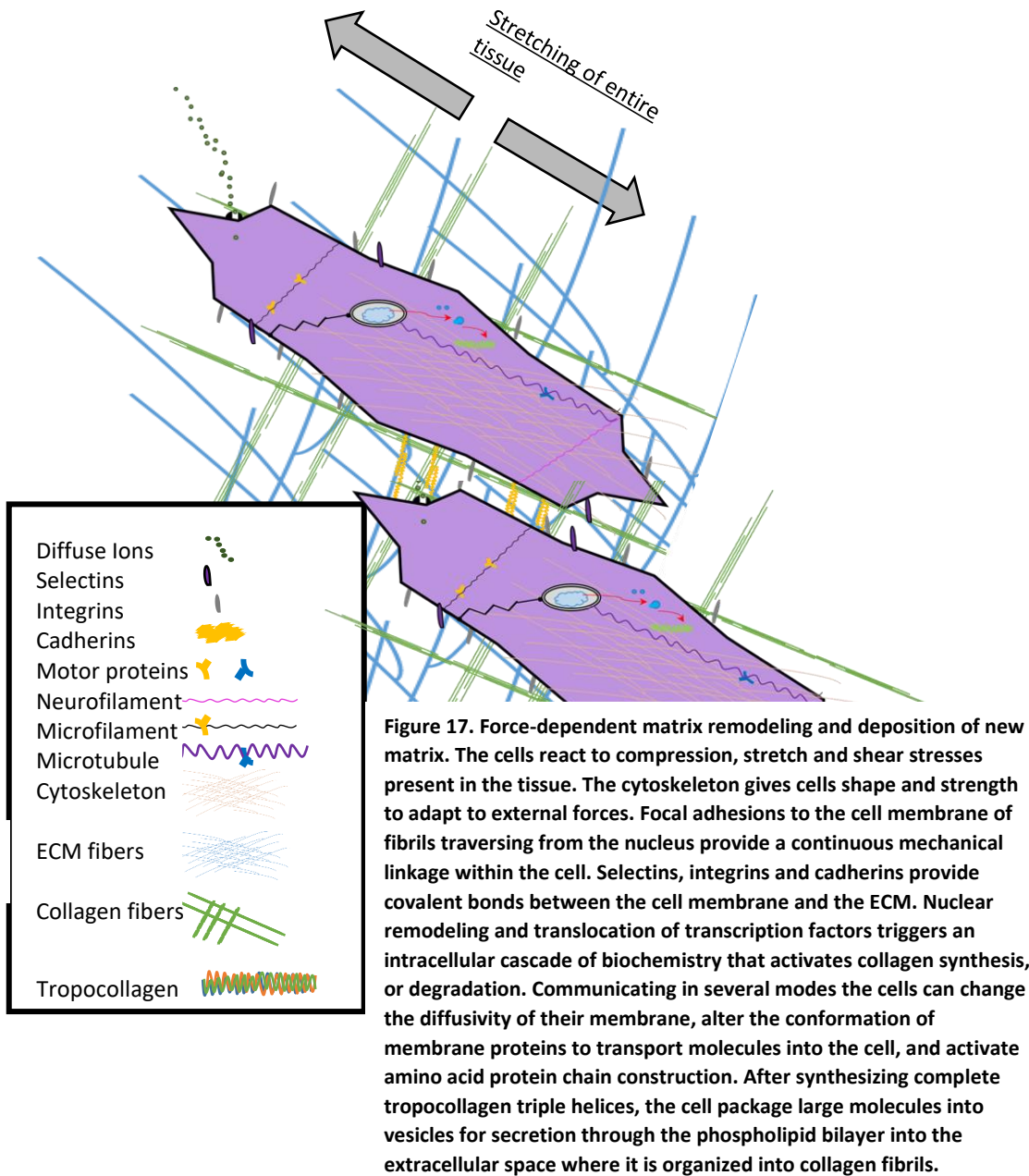


**Figure 16. The cell membrane is a phospholipid bilayer riddled with select molecules, channels, receptors, relays, and effectors, which is reinforced by a filamentous cytoskeletal frame. Chemical cues are received by receptors within the membrane, by passive diffusion through the membrane, and by channels that actively transport factors between cells and through the cell wall. These chemical signals trigger effectors which synthesize cyclic AMP from ATP in order to activate protein kinase, which aids in collagen synthesis.**

communication, are essential in cell and nuclear mitosis, contribute to cell motility and are responsible for much of the intracellular transport. The microfilaments are a made from two G-actin chains coiled together and tether the elements of the intracellular space in place. The

neurofilaments, or intermediate filaments, are made from 8 tetramers, akin to keratin, coiled together into a ropelike structure and they serve to connect the cellular cytoskeleton to the adjacent cells, particularly relevant in the endothelium. The microtubules are a heterodimer of alpha and beta tubulin units arranged into microchannels that create an extensive network for intracellular and intercellular communication. Motor proteins attached to the microtubules, microfilaments and intermediate filaments actively transport vesicles, chromosomes and other cell elements in a controlled manner<sup>54</sup>.



The endothelial cells that cover both surfaces of the valve play an important role in valve function. The endothelial layer protects against calcific disease. The endothelial layer of cells also has a role in embryonic development, regulation of cell attachment, modulation of the mechanical properties of the valve, prevention of VIC differentiation into pathological cell phenotypes and regulation of the valvular ECM. Valve endothelial cells have a unique range of

properties not seen elsewhere in the vasculatory system. Furthermore, the VEC are differentiated from each other on each side of the valve, which respond to dramatically different flow conditions. The surface chemistry of human vasculature, and especially valves, is a living layer of highly specialized cells that are strongly interconnected with the layers beneath in order to create a feedback loop for proliferation, differentiation, degradation and regeneration.

## Reactions to Implants

All biomaterials will elicit cellular and tissue responses when implanted *in vivo*. These biological responses are the inflammatory response, the wound healing response, foreign body reactions and fibrous encapsulation of biomaterial implants. Macrophages are the key immune cells that respond to foreign materials and damage. Macrophages are myeloid immune cells throughout the tissues of the body, in order to ingest and degrade dead cells or foreign material, as well as initiate the inflammatory response. In certain cases, macrophages aggregate to become multinucleated giant cells that remain at the interface for the lifetime of the implanted material, fused foreign body giant cells (FBGCs) are the dominant form of this giant cell type in the body. An important role of macrophages is the appropriate degradation of bio-resorbable materials by extracellular degradation and phagocytosis. The surface chemistry of the biomaterial implant plays a crucial role in the foreign body reaction. The foreign body response includes protein absorption, adhesion of monocytes/macrophages, fusion into FBGCs, and modifications to the biomaterial surface. The goal with medical implants is to use a better understanding of macrophages in rejuvenation to create smarter tissue engineered constructs that elicit a favorable immune response, both short and long term.

The first reaction to implants is protein absorption to the biomaterial surface, which is followed by the development of a provisional thrombus layer at the interface around the biomaterial. Cytokines, growth factors and chemo-attractants within the provisional matrix recruit cells from the immune system to the site. Acute inflammation follows the provisional matrix formation and is due to the degranulation of mast cells, histamine release and fibrinogen absorption, all of which is characterized by the presence of neutrophils (polymorphonuclear leukocytes, PMNs).

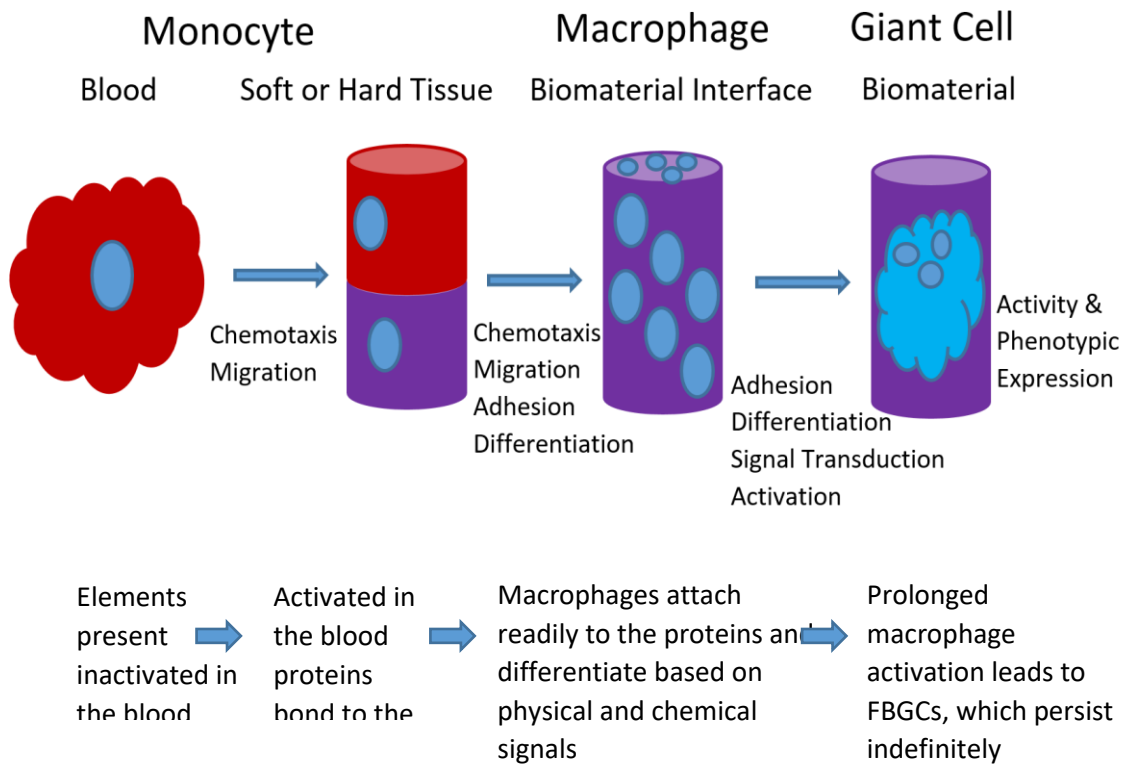


**Figure 18. The cascade of events in response to implanted materials begins with extensive protein adhesion to the implanted material surface, which adhere monocytes to practically any material surface <sup>8</sup>.**

There are smart ways to alter these events to improve levels of remodeling and lessen fibrous tissue formation, which has shaped many new copolymer choices for surgical implants.

Granulation tissue comes after chronic inflammation and is followed by foreign body reaction and fibrous capsule formation.

As macrophages aggregate at the interface they become a group with microbicidal and tumoricidal functions. Interferon- $\gamma$  (INF $\gamma$ ) and tumor necrosis factor (TNF), or lipopolysaccharide (LPS), are key factors that signal the pro-inflammatory secretion of cytokines. Natural killer cells and T-cells both produce INF $\gamma$ . Typically for host defense, macrophages secrete nitric oxide synthase and pro-inflammatory cytokines along with TNF, IL-12 and IL-23<sup>55</sup>. Importantly, this response has detrimental effects as the increased production of IL-1, IL-6 and IL-23 signal more TH17 cells to release more IL-17. IL-17 release leads to polymorphous leukocyte recruitment, which has the potential consequence of immunopathology and inflammatory diseases.

Macrophages directly associated with wound healing and reparative action arise due to innate or adaptive signaling mechanisms. These cells play a role in repair rather than defense. In reaction to injury, IL-4 is released by mast cells and basophils, which in turn promotes the formation of macrophages that aid in wound healing by synthesizing components of the extracellular matrix. These particular macrophages release small amounts of pro-inflammatory cytokines and are inefficient at producing radicals. They secrete very little IL-12 and IL-23, but high levels of IL-10, an anti-inflammatory cytokine. The adaptive immune response can also release IL-4 and has been proposed as the predominant pathway for the development of wound healing macrophages. The release of Interleukin-4 and 13 (IL-4, IL-13) from degranulating mast cells has been connected to the extent and degree of subsequent foreign body reaction<sup>8</sup>.

Wound repair, as a biological response, is generally beneficial but there are clear cases where dysregulated activity causes tissue fibrosis.

Macrophage plasticity – Macrophages have the interesting characteristic of being terminally differentiated, but can respond to local microenvironment signals and switch phenotype to one of the various macrophage subtypes. Macrophages can be mobile or stationary. They are 21 microns in size, they engulf debris and consume bad cells, phagocytosis. Macrophages are produced by the differentiation of monocytes in tissues. This is evolutionarily ideal because it gives the ability to form rapid response to a pathogen. FBGCs are terminally differentiated and exhibit poor phagocytic capacity. These cells are associated with chronic inflammation and biomaterial degradation.

Fusion mechanisms, recognition – At the structural level, cell fusion requires both the approximation and disruption of cell membranes. One modulator of fusion is calcium ions that bind Soluble NSF Attachment protein Receptors (SNAREs) and destabilize the membrane to allow fusion.

Tissue, protein and cellular responses – Four stages to tissue injury: hemostasis, inflammation, proliferation, and remodeling<sup>56</sup>. Damage to vasculature triggers the activation of platelets and subsequent blood clotting factors initiate hemostasis. This provisional matrix consists of erythrocytes and fibrin, and provides an adherent platform for other cell types to migrate. Platelets also release growth factors that signal neutrophils, macrophages, and fibroblasts. The neutrophils arrive first to remove debris and bacteria, as well as recruit macrophages to the site. Macrophages then secrete platelet derived growth factor, TNF, IL-6, granulocyte-stimulating factor, which serve pro-inflammatory roles, and GM-CSF, which recruits more macrophages. 48 hours after injury the classically activated macrophages are the predominant cell type. At this time, the macrophages phagocytose debris and apoptotic cells. Along with T lymphocytes polarizing macrophages to reparative phenotype with the release of

IL-4 and IL-13, the process of cleaning debris itself seems to lead to conversion to a reparative macrophage. The proliferation phase increases the number of cells, new blood vessels are formed, and extracellular matrix is synthesized and deposited. Reparative macrophages and fibroblasts continue to resorb debris and lay down new matrix, which contributes to angiogenesis along with signaling factors, and granulation tissue if formed. The remodeling phase restructures the granulation tissue with metalloproteinases and their respective tissue inhibitors to form mature tissue or scar.

Phagocytosis – as size and multinucleation proceed the phagocytic abilities decrease and the ability to degrade the ECM progresses. Size limit is between 10 to 100 microns in diameter to be engulfed.

Surface chemistry – implants immediately get a layer of host proteins before interacting with host cells. This protein coating includes albumin, vitronectin, fibrinogen, globulins, fibronectin, and complement proteins<sup>57-61</sup>. The characteristics of the absorbed proteins are crucial determinants to the biological reaction to implants, making the surface chemistry of implants quite important. Remarkably, macrophages have been shown to adhere to nearly all surfaces, however the type, level, and surface conformations of adhered proteins will affect the adhesion and survival of monocytes, macrophages and FBGCs. Microsize topography has been researched for its effects on interface.

Degradation – Unlike wound healing, foreign body response has a persistent macrophage activity for the life of the implant. Macrophages use podosomes to migrate and perform mechano-sensing, or haptokinesis, to interact with absorbed proteins and change position. FBGCs remain for the lifetime of the implant. Macrophages and FBGCs secrete reactive oxygen intermediates (ROIs), enzymes, and acid between the cell membrane and biomaterial



surface. Polyurethane can become stress cracked due to this, Polypropylene may undergo surface oxidation by ROIs, as well as polyethylene. The addition of antioxidants helps and this is shown in the literature. Resorbable polyesters can be designed to degrade into monomer units that can be further completely degraded in the Krobs' cycle (PLA, PGA, PCL). Not all polyesters undergo degradation, polyethylene terephthalate (Dacron<sup>®</sup>, Vascutek Terumo, Inchinnan, Scotland) has been used as a vascular graft material with good results for over 30 years, although some biodegradation of Dacron<sup>®</sup> can be observed <sup>62</sup>.

Chemistry and specific materials – It is observed that biomaterials produce micro-environmental cues that modulate the response of inflammatory cells <sup>63</sup>. So surface chemistry, ligand presentation, degradation rate, and release of growth factors as well as size, stiffness and topography will determine the foreign body response.

Implants with more macrophages end up having more fibrosis. Higher surface to volume ratios will have more macrophages. PEO has been shown to reduce protein absorption, macrophage attachment and postoperative adhesions <sup>64</sup>. Hydrophobic molecules, typical of implants, have high affinity to several proteins. The protein change conformation to expose their hydrophobic domains, which are attracted to the hydrophobic surface chemistry. These conformational changes account for adverse reactions like inflammation, coagulation and foreign body response <sup>8</sup>.

Recent studies have shown that macrophages play an important role in dental implants<sup>67,208,217,218</sup>. With osseointegration of dental implants, it has been observed that the foreign body reaction and the inflammatory response play critical roles in allowing bone to grow onto the implant surface. The problem is observed in the poorly vascularized and enervated fibrous tissue that ultimately surrounds the implant, which is commonly observed.

For biomaterials that do not degrade it is best to implant those that evoke less macrophage response, this is because the FGBCs will be there for the lifetime and macrophages will continue to infiltrate and try to consume undigested particles and remain on the surface and/or fuse into FGBC.

The vast number of vascular grafts implanted each year shows engineers that there is significant demand for parts. The options are autograph, homograft, xenograft, bioprosthetic and purely synthetic grafts. These options each fall short of meeting the demand and inadequately. The prospects for engineering better synthetic grafts is realistic, while the benefits of scaffold based engineered tissues may ultimately be of more value to humankind. TE scaffolds offer patient specific geometry and sizing for grafts using microCTA scans. Along with a graft that contains the patient's own cells there is great promise that grafts of this type will elicit almost no immune response and will become unified with the graft recipient's native vasculature.

The essence of tissue engineering is using cells to do the building and the organization of molecular matrices for ECM structure and connectivity, which then leads to adequate signaling and response to mechanical demands from the environment. Importantly, the complexity of cells remains well beyond the scope of human engineering; however, the innovation of tissue engineering is the use of the cell as itself the engineer, where the human is merely configuring the ideal materials so that the cells can do the job. This method is akin to using seeds to grow a garden along a lattice which you have designed, and rooted in soil that is especially composed.

## CHAPTER 3: TISSUE ENGINEERING

### Materials

Hydrogels are useful tools for designing water based solutions with tunable viscosity and composition. The properties of hydrogels can be remarkable due to the ability to absorb water. This propensity for hydrogen bonding with water allows the design of hydrogels with high viscosity that are composed of mostly water. Using natural hydrogels with high viscosity, synthetic polymers with biocompatibility can be added to supplement the polymerization reaction. With biocompatible choices for monomer, photoinitiator it is possible to make viscous hydrogels that are ideal for nozzle-based extrusion and furthermore, crosslink into a printed scaffold with tailored mechanical properties and a remarkable diffusivity. Hydrogels are used across industries, but their utility as a medical grade implant is evident and their application to tissue engineering, specifically, may yet become their greatest employment.

One of the most important molecules for creating synthetic hydrogels is poly(ethylene glycol) PEG. It is a straight chain that repeats a carbon-carbon-oxygen monomer unit in its backbone chain. It has remarkable utility for mankind and the medical applications for PEG continue to be proven. Paul Flory made some of first discoveries about the qualities of PEG in the 1960's. Since then a plethora of uses have been found for PEG owing to the elegant simplicity of its chemical structure and inert nature. For TE scaffolds PEG has the correct range of transfer properties, grafts however need more mechanical properties so polyurethane, a

branched polymer network, has proven more useful. PEG is not a native molecule for cells, however PEG is readily degraded by the natural mechanisms of cells, which is a distinguishing factor among relatively similar chemical structures of relevant polymers. As a highly porous and simple matrix PEG has the unique propensity to bestow its material properties to any copolymers<sup>68</sup>, possibly suggesting that long thin chains have a strong influence on material properties. As a filamentous sparse matrix PEG may play the most important role as a fresh garden for cells. The cells can adhere and begin growing their natural ECM unhindered by the scaffold matrix. The scaffold will degrade incrementally over time as the cellular feedback loop for recycling activates. Over time collagen is secreted and organized by cells, which leads to changes in the mechanical effect of stress on the cells and therefore cellular activity will shift to maintain equilibrium of perceived strains. Several groups demonstrated the performance of PEG as a biomaterial in the 1960's<sup>69,70</sup>.

FDA approval in 1990 of PEGylated hydrogels for drug delivery was a stepping stone that brought research into the field of drug delivery and extended or controlled release pharmaceuticals. Other polymers have similarly low cytotoxicity and foreign body response and are successfully grafted into humans: PLA, PGA, PCL, PU, PMMA and still others<sup>71,72</sup>, but the mechanical properties and degradation of PEG based biomaterials make it useful for degradable scaffolds for TE. The addition of functional end groups, like methacrylate or diacrylate, to PEG backbones is useful to make more sites for cell attachment and different crosslinking structures. Cell adhesion has been shown to be low for simple PEG scaffolds, however functionalizing PEG chains with a diacrylate group grafted to each end dramatically improves cell adhesion. This known as poly(ethylene glycol) diacrylate PEGDA and shows the qualities of PEG and is able to

attach cells more readily<sup>73,74</sup>. The mechanical properties of PEGDA scaffold can be tailored by controlling the molecular weight distribution.

Protein based natural polymers, such as collagen, silk and gelatin are polymerizations of amino acids and have elegant conformations of their backbone chains, which makes their mechanical properties so outstanding and also contributes to their macrostructural organization. The polymers can be further crosslinked with chemical agents, such as formaldehyde or glutaraldehyde, to form thermoset materials that can be molded into various shapes. These crosslinked protein polymers have been used with silicone rubber using a lamination technique to produce synthetic skin<sup>75</sup>. The strength of these materials is a quality for direct implantation, however the attributes of less robust polymeric materials are better suited for cell seeding, proliferation and generation of a well-organized natural ECM.

Glycosaminoglycans GAGs and polysaccharides are important natural polymers used in TE. These molecules are branched and hydrated by nature, they provide the compressive and shock bearing component of tissue. Specific examples include hyaluronic acid, chondroitin sulfate, keratin sulfate, and chitin. Covalent crosslinking with PEG and GAGs creates highly swellable gels, showing a positive interaction effect. GAGs can be deacetylated or desulfated to provide free amino groups in order to provide a site for PEG covalent bond. This type of copolymer hydrogel shows promise because of the balance between straight chains and bulky polysaccharides, and the corresponding balance of mechanical properties and cell adhesion. The benefits can be tailored further by producing interpenetrating networks of covalently and ionically bonded polymers, which requires the addition of a cation to ionically bond specific regions of the polymers, as in alginate copolymers with PEGDA. This is similar to fixing with

glutaraldehyde except the bonds are not covalent. The formation of a secondary crosslink network can increase mechanical properties significantly without changing degradability<sup>76</sup>.

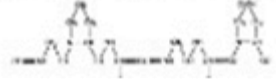
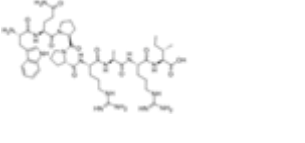
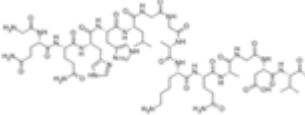
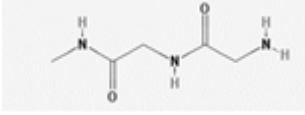
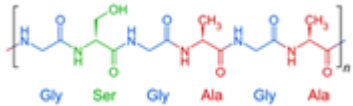
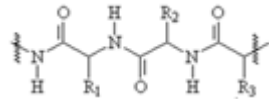
Sodium alginate is mannuronic acid and guluronic acid, and undergoes gelation by a complexation mechanism when exposed to a divalent cation, such as calcium, magnesium or barium. This coacervation phenomenon has been well studied for the encapsulation of mammalian cells. There has been extensive research on the properties of alginate for TE because it makes a low viscosity gel that can be poured, and it can be made into an elastic material with substantial mechanical properties. Due to its natural origin it is cytocompatible and has no toxic byproducts or chemical catalysts.

Poly(lactic acid) PLA was used in the 1950s and aiding in aortic tissue regeneration, as well as fixation of fractures<sup>7</sup>. PLA can have a wide range of properties and is appropriate for soft and rigid applications. *In vivo* performance of PLA bone implants shows low immune response from the host, it shows minimal infiltration of the implant by cells, although the surface becomes coated with proteins and may have persistent macrophage activity<sup>71</sup>. Poly(glycolic acid) PGA was originally used in guides for bone healing in the 1960's. In the subsequent decades, PGA and PLA became used in sutures, clips, staples, pins, fibers, meshes and drug delivery matrices. It is the synergistic combination of these two polymers that makes their products so varied and so functional. The cyclic monomers lactide and glycolide can be used to create the gambit of copolymer concentrations to tailor the mechanical properties. Preventing oxidation and hydrolysis is important when polymerizing this hydrogel in order to make pure product.

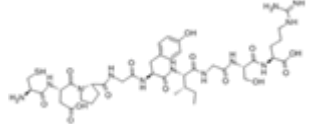
With a few good examples of biomaterials introduced, several tables of biocompatible polymer that are relevant to TE are presented. The number of viable polymers illustrates the

recognizable nature of their chemistry and structure when implanted into the human body. The natural proteins and polysaccharides are all organic however some are isolated using man made techniques beyond heating and pressure. The synthetic polymers are man-made and are often synthesized using expensive, intensive chemical procedures.

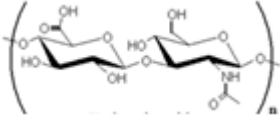
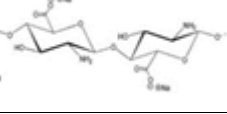
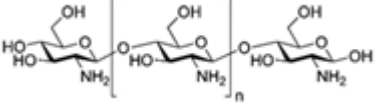
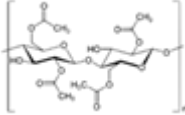
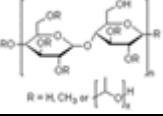
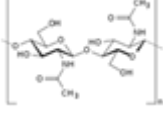
**Table 2. Proteins that are useful in TE and medical applications.**

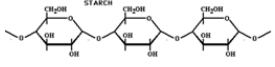
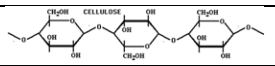
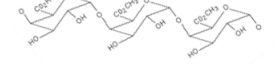
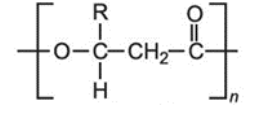
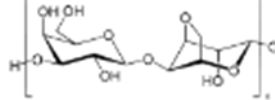
<u>Organic Proteins</u>				
<u>Name</u>	<u>Abbreviation</u>	<u>Monomer</u>	<u>Medical Applications</u>	<u>References</u>
Collagen Type I	Collagen Type I	amino acid chain with triple helical structure	Cell encapsulation, dermal substitutes, hydrophobic bonding, cell adherent, slow gelation.	12,77,78
Elastin	Elastin	amino acid chain with highly coiled structure	Creating highly elastic and robust scaffolds. Tony Weiss PhD has shown remarkable results with TE scaffolds.	79,80
Gelatin Porcine Skin	Gelatin		Cell seeding and cell adherent, hydrophobic thermal bonding, and can be glutaraldehyde crosslinked (cytotoxic)	81-87
Fibronectin Bovine	Fibronectin		Fibronectin is a high-molecular weight (~440kDa) glycoprotein of the extracellular matrix that binds to membrane-spanning receptor proteins called integrins. Similar to integrins, fibronectin binds extracellular matrix components such as collagen, fibrin, and heparan sulfate proteoglycans (e.g. syndecans).	53,88,89
Fibrinogen	Fibrinogen		Cell recognition, and degradable, good copolymer with PEGDA.	57,90,91
Fibrin	Fibrin		Surgical glue, thromin-catalyzed fibrin polymerization, fast crosslinking time, high Young's modulus, TE scaffolds, wound dressings, copolymer with PGA, PLA, collagen and others show results.	92
Silk	Silk		Gelation of silk with ethanol, Hydrophobic formation of semicrystalline structures, great mechanical properties, slow degradation time.	63,79,93,94
Keratin	Keratin		Fibrous protein forming the main structural constituent of hair, feathers, hoofs, claws, horns, etc. 11 unit repeating amino chain, alpha helix conformation like collagen. Disulfide bridges add strength to the tertiary structure.	75



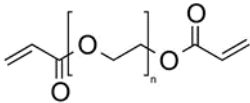
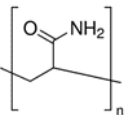
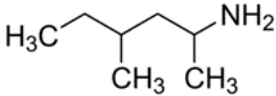
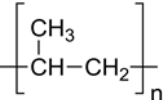
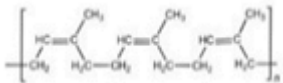
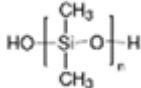
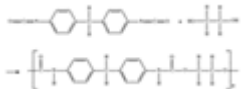

Laminin	laminin		Copolymer with PEGDA, degradable, TE scaffolds, cell cultures, thin films, surgical glue, binds to collagen and other natural ECM proteins because it is a natural ECM molecule.	95
---------	---------	---	--	----

**Table 3. Polysaccharides that are useful in TE and medical applications.**

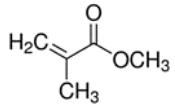
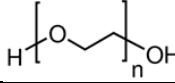
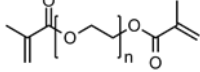
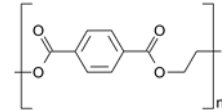
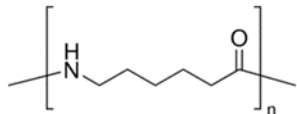
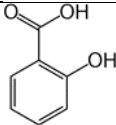
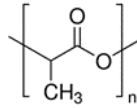
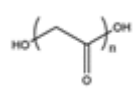
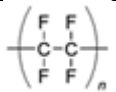
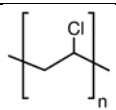
<u>Organic Polysaccharides</u>				
<u>Name</u>	<u>Abbreviation</u>	<u>Monomer</u>	<u>Medical Applications</u>	<u>References</u>
Hyaluronic acid	HA		Wound healing, bioprinting, by UV crosslinks, fast gelation, low mechanical properties, chondroitin sulfate is used for TE solids. Both are glycosaminoglycans	96
Sodium Alginate			Cell encapsulation but needs modification for cell adherence, CaCl2 can be toxic with prolonged exp., CaCl2 ion exchange creates fast gelation	85,97-99
Chitosan			Biodegradable, useful for cartilage or meniscus implants and injections, wound healing, topic use, and	100-103
Cellulose acetate	Rayon		Artificial kidney, cellophane and rayon, films, membrane and fibers.	104,105
Hydroxypropyl methyl cellulose	HPMC	 R = H, CH <sub>3</sub> or $\text{CH}_2\text{CH}_2\text{CH}_2$	Cell adhesion, drug release hydrogels, scaffold materials, ophthalmology uses	106-109
N-acetylglucosamine (derivative of glucose)	Chitin		Favorable as surgical thread, flexible, strong and biodegradable. exoskeletons of arthropods. Similar to linkages between glucose units that form cellulose - one hydroxyl group on each monomer replaced by an acetyl amine group, making for increased hydrogen	103,110

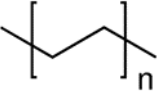


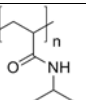
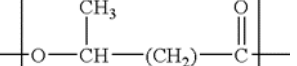
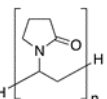
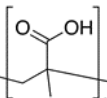
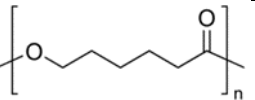
			bonding and the improved strength of chitin polymer matrix.	
polymeric carbohydrate - many glucose units joined by glycosidic bonds.	Starch		Cell adhesion and proliferation, biomaterials for degradable applications.	111,112
Cellulose	Wood		Thin films, packaging, fibrous stiff biomaterials, and can be modified with functional groups.	113,114
heteropolysaccharide, as fruits ripen pectin is being broken down by pectinases	Pectin		Combined with silk it's soft, complex and has exceptional strength, and injectable biomaterial for immobilization of cells for bone regeneration.	115
Hydroxyalkanoates	Linear polyesters produced in nature by bacterial fermentation of sugar or lipids. Bioplastic		Sutures, suture fasteners, meniscus repair devices, rivets, tacks, staples, screws, surgical mesh, repair patches, slings, cardiovascular patches, adhesion barriers, stents, guided tissue repair/regeneration devices, nerve guides, atrial septal defect repair devices, pericardial patches, bulking and filling agents, vein valves, bone marrow scaffolds, meniscus regeneration devices, ligament and tendon grafts, ocular cell implants, wound dressings	116-118
Agarose	Agarose			119,120

**Table 4. Synthetic polymers that are useful in TE and medical applications.**

<u>Synthetic Biomaterials</u>				
<u>Name</u>	<u>Abbreviation</u>	<u>Monomer</u>	<u>Medical Applications</u>	<u>Reference</u>
Poly(ethylene glycol) diacrylate	PEGDA		Tailorable mechanical properties with MW of monomer, photoinitiated hydrogels	<u>S</u> 73,74,121-124
Polyacrylamide (PAM)	PAAm		pH sensitive and non-biodegradable	101,125-127
Dimethylamylamine	DMAA		Contact lenses use this as a major component, see file in Res. Lit. folder, N,N - dimethylacrylamide. FDA ban in dietary supplements because it elevates BP.	128,129
Polypropylene	PP		Membrane oxygenators, sutures, vascular grafts, nonwoven fabrics, thermoplastic with low energy surface so it is not easily adhered	130-132
Dimethyl siloxane	PDMS		Mixed with stannous octate as catalyst it is used for implant fabrication	133,134
cis 1,4 polyisoprene	Rubber		Tubing and catheters., inferior to synthetic rubbers	135-137
Polyurethanes	PU		Coating for implants, great abrasion resistance, strong thermosetting urethane links	138-140
Polyacetals	Polyacetals		Mechanical properties	141,142

Polysulfones	Polysulfones		High thermal stability, high strength, high resistance to oxidation, flame retardant, ether linkages impart the stability, transparent thermoplastics	143
Polycarbonates	Polycarbonates		excellent thermal and mechanical properties	144,145
polystyrene	PS		Sterilized for medical device packaging, high impact resistance.	58,144,146,147
poly(vinyl alcohol)	PVA		Vocal cord reconstruction. PVA as support material that dissolves in warm water. nontoxic. non-biodegradable	148,149
poly(acrylic acid)	PAA		self healing materials, pH sensitive and non-biodegradable, nonionic, hydrophilic polymer: repel nonspecific protein adsorption and cell adhesion,	150-153
polymethylmethacrylate, "acrylic"	PMMA		blood reservoir, IV system, membranes for blood dialyzer, contacts (optics) excellent optical transparency, dentures, bone cement (F451)	154
poly(2-hydroxyethyl methacrylate)	PHEMA		1950's soft contact lens material, non-biodegradable	155-158
Methacrylic acid	MAA		soft contact lens material copolymer	159-162
Butyl methacrylate	BMA		soft contact lens material copolymer	163,164

Methyl methacrylate	MMA		soft contact lense material copolymer	165-168
Poly(ethylene oxide)	PEO, PEG in biomaterial lingo		Laxative, controlled drug release tablets, excipient in pharmaceuticals.	64,169,170
Polyethylene glycol dimethacrylate	PEGDMA		Photosensitive polymer, less dense than PEGDA and makes strong co-polymers with PEGDA.	171
Polyethylene terephthalate	PET		Woven into strong flexible vascular grafts, sutures, meshes. Structure spirals and oxygen groups make steric hindrance that gives the stiffer elastic properties.	43,44,172-177
Polyamides	Nylons		Strong hydrogen bonding between chains due to the amine group make exceptional elastic strength.	178,179
Poly alpha-hydroxy acids	<i>bioresorbable polyesters</i>		Topical creams, degradable implants, electrospun fibers, surgical sutures, and drug delivery.	61
Poly lactide	PLA		Bone fractures – mesh, anchors, screws, pins, biodegradable in 6-24 months, copolymers with PGA,	71,180-182
Polyglycolide	PGA		Biodegradable in 6-12 months, orthopaedic implants, crystalline structure with high strength and hydrophilicity.	180,183-185
[62]Polytetrafluoroethylene	PTFE (Teflon)		Requires high temp for molding. Plastic implants, ASME F754,, Fluorocarbon polymer	28,44,186
Polyvinyl chloride	PVC		IV tubing, dialysis, catheters, cannulae	187

Polyethylene	PE		Total hip acetabular, patellar of knee (ultra high density, MW), density of polymer drives material properties. Low density used for tubing and tear resistant bags	[62]
Low density polyethylene	LDPE		Soft waxy solid; blood bags, thin films	[62]
High density polyethylene	HDPE		Rigid translucent solid; hip joints	[62]
Poly(N-isopropyl acrylamide)	PNIPAAm		Temperature sensitive	151,159,188
Polyhydroxyalkanoate	PHA		Used by Langer with PGA for copolymer to create aortic graft 1999	111,116-118
Poly(N-vinyl pyrrolidone)	PNVP		Soft contact lens material copolymer, non-biodegradable	128,129,189
Poly(methacrylic acid)	PMAA		pH sensitive and non-biodegradable	160
Poly(caprolactone)	PCL		3D scaffolding for cell seeding, drug delivery, melt cure, robust mechanical properties,	190-193

The tables of biomaterials illustrate the types of molecules that function in TE applications as well as non-degradable devices, implants and items like contact lenses. In addition to demonstrating the specific moieties that are inert to the human body, the number of materials that already serve a purpose in medical applications emphasizes the adaptability of the human body to many materials as long as they are perfectly sterile. The prevalence of functional materials urges researchers to discern the differences in performance for many hydrogels and many scaffold materials.

Hydrogel polymerization is about the attraction between monomers in the solution. The chemistry of free radicals and the chain growth of polymer units go hand-in-hand. For photoinitiated solutions the free radical is the product of light hitting the photoinitiator, for chemical catalysts it is in free radical form, and for ionic catalysts it is not actually a free radical. The chemical structure and bond energies of a polymer, like PEGDA, control the structure of the crosslinked matrix. Likewise, the addition of copolymers will affect the hydrogel and the crosslinked matrix based on its chemical structure. Polymerization is catalyzed when the activated free radical takes an electron from one monomer unit and leaving that monomer with a strong attraction for a new electron, which it takes from a specific site on a new monomer unit, thus propogating this *step-growth* of the polymer units into a network. The residues of the photoinitiator are diffused away, and the crosslinked network in a macrostructure like a randomly woven fabric is created.

The bond lengths of the monomer unit determine where it will most likely form new bonds. The bond distance between two atoms is the sum of their covalent radii. In general, bond length decreases across a row and increases down a group in the periodic table, i.e. follows the trend for atomic radius. Bond length is related to how many electrons participate in the bond

formation, that is bond order. The dissociation energy of a bond is inversely related to the bond length. Bond lengths are given in picometers and in angstroms Å, where 110 pm equals 1.1 Å. The length of a carbon-hydrogen bond equals 0.11 nm. Bond lengths are measured by X-ray diffraction or approximated by microwave spectroscopy.

For PEGDA, the C-H bond is 108-110 picometers, C-C bond is 154 pm, C=C bond is 134 pm, C-O bond is 143 pm, C=O bond is 120 pm. The double bonds are more readily broken than single bonds of greater length because the dissociation energy of the double bond is lower than the dissociation energy of a single bond between the same atoms. When a free radical takes an electron from the monomer it must break a bond. It takes an electron from the double bonded carbons and propagates step growth to the other end of the monomer. While random reaction must be considered the overall propensity for the system to take the electron from the double bonded carbon is strong.

In addition to bonding, the atomic nuclei create polarity that will affect the affinity of free radicals for certain regions. The C-O bonds are strongly polarized towards oxygen because of its electronegativity of 3.44 vs 2.55 for carbon and 2.2 for hydrogen, where fluorine is the most electronegative at 3.98 and lithium is 0.98. This electronegativity of oxygen means that electrons engaged in bonding between the carbon and oxygen will be closer to the oxygen most of the time. This affects the strength of the adjacent bonds in which the carbon is engaged. This is the mechanics of carbonyl groups and the applications are shown in the figures about photoinitiators. The carbonyl group serves a useful purpose, which is seen in its abundance across many biomaterial monomers.



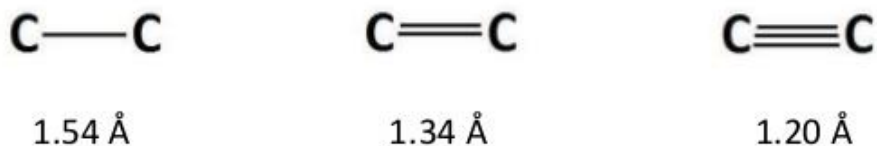


Figure 19: Bond length between carbon atoms in polymer chains. The double bond in PEGDA is the most functional site for polymerization step growth due to the covalent radius of carbon.

Table 5: Bond length and bond dissociation energies<sup>10</sup>.

Bond Elements	Dissociation E (kJ/mol)	r bond length (pm)
C-C	346	154
C=C	602	134
C≡C	835	120
C-N	305	147
C=N	615	129
C-H	423-439	108-110
C-P	264	184
C-O	358	143
C=O	799	120
C≡O	1072	113
C-F	485	135
C-Cl	327	177
Si-Si	222	233
Si-O	452	163
Si-S	293	200
Si-F	565	160
Si-Cl	381	202

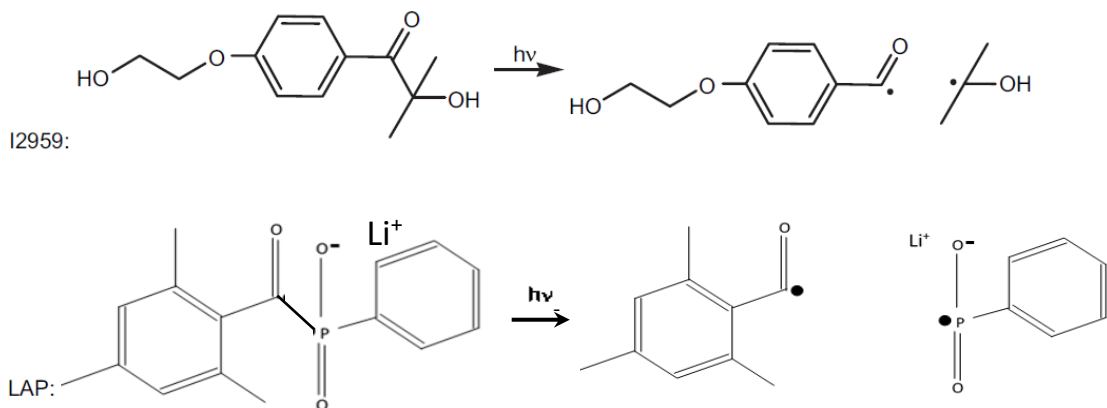
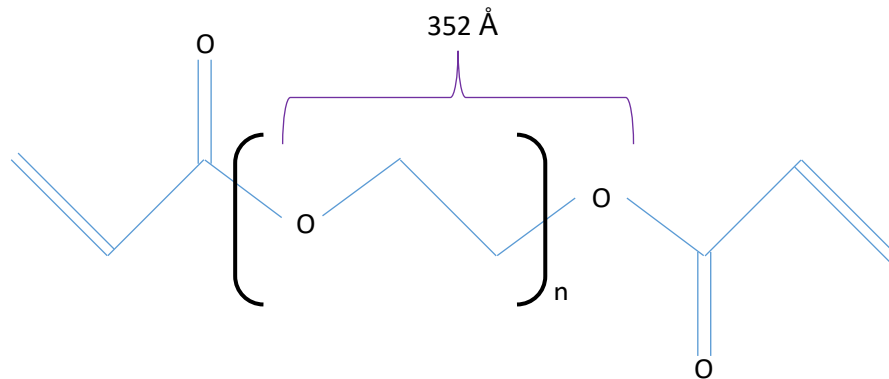


Figure 20: Photoinitiator radicalization for Irgacure and LAP.

The relative size of the hydrogel molecules to the extrusion is estimated to predict any effects of small nozzles with large MW polymers. The molecular structure has 154 angstrom C-C bonds, 143 angstrom C-O bonds, and angles of 109.5° between backbone atoms. In PEGDA average  $M_n$  6,000 there are on average 130 repeats of poly ethylene oxide between the two

diacrylate functional end groups. The number of repeats and the length per monomer give the rough estimate that an ideally straight PEGDA 6,000 chain will be 15,000 angstroms. This means an ideally straight chain of PEGDA 6,000 would be on the order of 1% of the diameter of a 0.1mm nozzle.

The U. S. Food and Drug Administration (FDA) approved PEG usage in the pharmaceutical, food, and cosmetics industries<sup>194</sup>. PEG is a commercial product made from ethylene oxide with water and ethylene glycol or ethylene glycol oligomers. PEGs can be functionalized as telechelic polymers for hydrogels preparation. PEG is bifunctionalized by adding acrylate and methacrylate groups that are reactive in polymerizations and their presence controls the distance between crosslinks.



**Figure 21: PEGDA where n defines the molecular weight of the polymer chain and the length of each PEO monomer unit in the backbone chain is roughly 352 angstroms.**

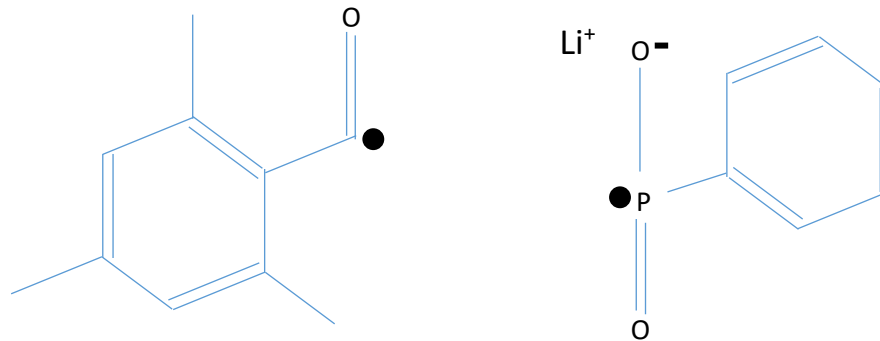


**Figure 22: LAP photoinitiator broken into its free radical and ionic pair after activation with 365 nm ultra-violet lightwaves.**

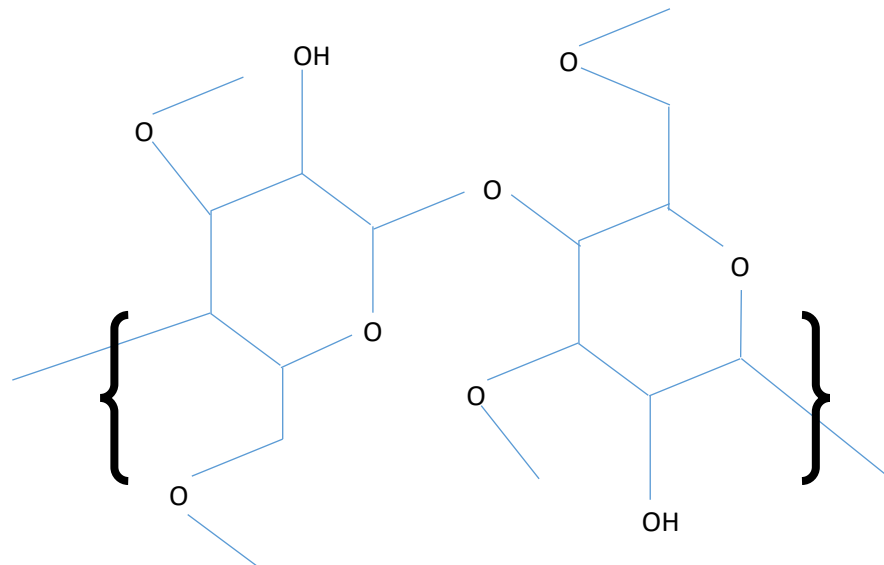


**Figure 23: HPMC monomer has a larger molecular volume than PEGDA per atomic weight.**

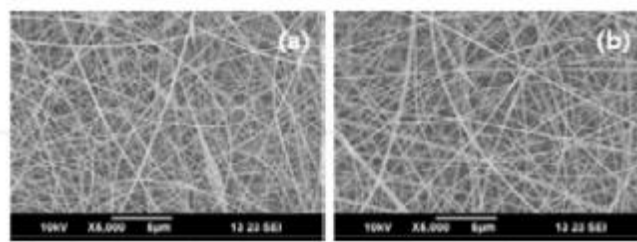


**Figure 24. SEM micrographs of electrospun fibers of HPMC showing the polymerization into long straight chains at two different concentrations: (a) 0.5 wt% and (b) 1.0 wt%. With permission from John Wiley and Sons.**

So the polymerization reaction of monomers proceeds by steps as the initiator activates functional end groups by removing an electron from the double bonded carbon diacrylate group. The propensity is to dissociate the bond with the lowest energy which is the double bonded carbon so the activated PEGDA chains find end groups, bond with the carbon atoms, breaking the double bond and propagating the loss of the electron to the far end of the polymer chain, creating a new reactive site seeking to break a carbon double bond and further grow the chain.

By controlling the polymerization reaction with a photoinitiator that is non-cytotoxic and timing its rate so that the extruded material crosslinks before losing its shape it is possible to construct a wide variety of geometries with 3-D bioprinting. The chemical reaction is key to the crosslinking rate and the fate of all byproducts, but it also affects the mechanical properties. Several groups have worked on computer simulations to model the polymeric matrices of TE scaffolds in order to predict the mechanical properties of scaffolds. This work promises to clarify the atomic level of scaffold matrices and may allow for most intricate design of cell attachment site concentration and distribution.

## Scaffold Fabrication

Scaffold fabrication for tissue engineering has strict requirements that must be met in order to ensure potential long term viability as an implant. Most importantly, it must not be cytotoxic. This creates various challenges because many polymerization reactions are initiated with caustic reagents that cause certain harm in the human body. This limitation to the activation of hydrogels to create scaffolds leads to the use of special photoinitiators, thermal, and ionic catalysts as crosslink methods. Anseth et al have justified an excellent photoinitiator, lithium triphenyl benzoyl phosphinate (LAP) <sup>7</sup>. Due to its cytocompatibility and proven cell attachment LAP appears more relevant than Irgacure photoinitiators, which have struggled to succeed in TE due to cytotoxicity.

Pharmacology uses extensive cell replication for testing of medicines, as well other medical industry and genetic research groups have been routinely multiplying cells for experimental testing. Petri dish testing was a reasonable start for many cell adhesion studies.

Early on, the adhesion of cell to gelatin scaffolds was shown <sup>82,83,85-87,195,196</sup>. This propensity for cell to adhere within dishes of gelatin was at the time an interesting discovery. The limitation of this rudimentary method is there can be no mechanotransduction to elicit cellular reaction. Largely due to infectious disease research, many other good materials for cell cultures have been used including agarose <sup>197</sup>, starch <sup>198</sup>, fibrin <sup>90,199-201</sup>, cellulose <sup>107,108,202-204</sup>, and collagen <sup>205</sup>. As the knowledge of materials that attach cells grew over time, more ideas for fabricating the cell scaffold arose. Research groups began molding shapes for thermally crosslinked scaffolds and producing sheets of collagen and then rolling them into vessel scaffolds, as well as deuceullarizing vessels and reseeding them with new cells. Several of the conventional methods are relevant for testing of the cellular affinity of the scaffold, but none of them can create complex shapes to match the native geometry of many human vessels.

With the remarkable photoinitiator LAP, the context for sophisticated 3-D bioprinting technologies is opened. Several technologies are able to utilize this photoinitiator and they are each explored. The goal is to understand all of the options for rapid prototyping scaffolds so that a holistic view of the practicality of the work is achieved.

## *RAPID PROTOTYPING*

### *Laser Based Systems*

#### **Selective Laser Sintering**

This process is used for a wide range of materials that can be melted and fused. The process typically involves a fine powder that is exposed to a laser to create fusion at specific sites depending on the geometry of that specific layer. Then more powder is added and the

process is completed to create 3-D objects that grow from the bottom up as more and more material powder is added on top of sintered layers beneath<sup>206</sup>.

SLS directly fuses particles together layer by layer with a high energy pulse laser. Similar to stereolithography, this method starts with a tank full of bulk polymer, but rather than liquid photopolymer it is in powder form. As the print progresses the bed lowers and new powder is leveled over the top to be cured and bonded to the adjacent layers below. Overhangs are simplified because the excess powder supports those features more simply than FDM, where separate support material is required. The bulk material powder is maintained at a temperature just below its transition temperature to expedite particle fusion and print speed.

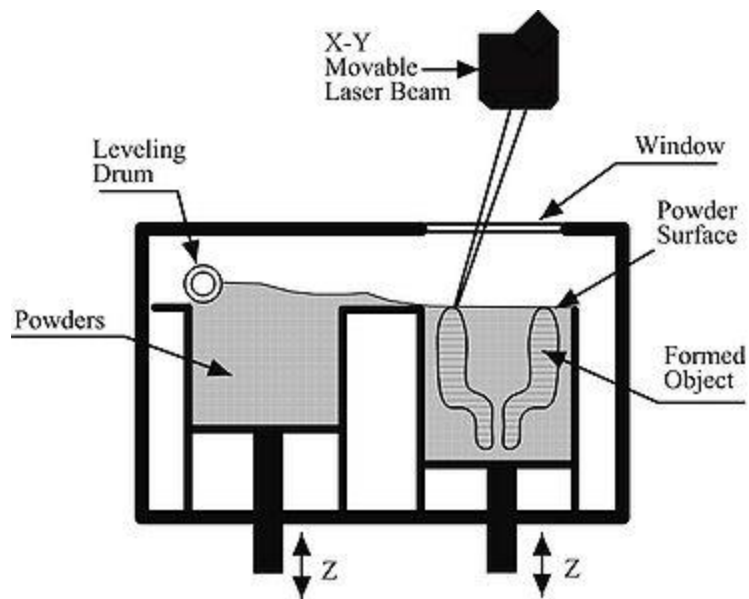


**Figure 25. Selective lazer sintering depiction <sup>4</sup>, with permission.**

A major benefit of this method is the wide range of materials that can be used: from plastics to metals there is a lot of flexibility in materials while creating durable prototypes. The quality of the powders is important, but base materials still are more abundant than photopolymer resins and are cheaper. The energy requirements for this method are rather high compared to other methods creating a certain compromise in costs. The industry average for

resolution with this method is 0.1mm. This method is most appropriate for small precise parts and is impractical for high volume production run. Great for exotic materials and metals.

### **Stereolithography**

This process has been around for 30 years. One of the major drawbacks to its usage as a fabrication process is the time required and the amount of scrap created. This makes each layer time consuming and costly. Although the refinement of the prints is noteworthy compared to other methods it has only begun to exploit the potential of extremely high resolution prints without the need to perform layer by layer scraping. Carbon M1 is a company manufacturing a new age SLA machine that is taking 3-D printing to the next level<sup>2</sup>.

SLA is another example of building layer by layer, but rather than extruding molten plastic through a nozzle, the process uses liquid plastic resin (photopolymer) which is cured by an ultraviolet laser. The process requires an excess amount of photopolymer to complete prints. As layers are cured the bed moves downward into the photopolymer bath in order to cure the next layer, upon completing the print the object is raised out of the photopolymer tank to expose the printed object and the excess photopolymer that was not cured is rinsed off and the tank is disposed of.

The process can be done bottom-up as shown in the figure or top-down, whereby the laser projects the entire 2-D layer at once with dynamic light projection technology. Digital Micro-mirror Device™ (DMD) technology consists of many small mirrors, which can be independently tilted to serve as a sort of dynamic mask to project the complete 2-D layer at once. The method of top-down is gaining interest, Carbon M1 printer, due to the minimal amount of photopolymer resin needed in the tank, the control of oxygen exposure and related

crosslinking, and the smooth irradiated surface due to the non-adhering transparent bottom plate.

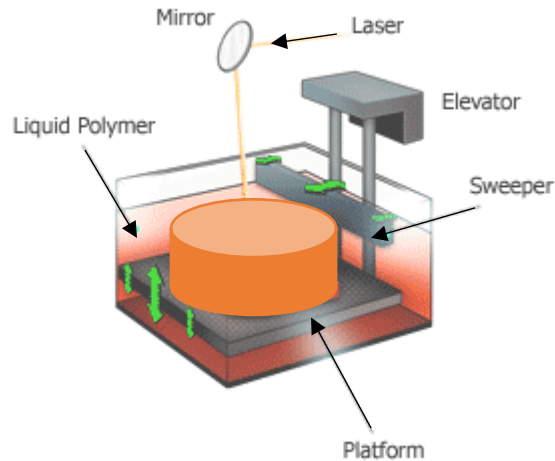


**Figure 26. Soft lithography works in small print area<sup>2,3</sup>, with permission.**

Resolution of SLA varies from 0.05mm to 0.15mm with an industry average of 0.1mm tolerance. It is more precise than FDM and is the preferred rapid prototyping method when small tolerances are required. This is because the cross sectional area of the laser can be smaller than the cross sectional area of the nozzle with nozzle based methods. This smaller cross sectional area also makes SLA much slower than FDM. Production times may be several days for refined large parts. It is also noteworthy that material costs are much higher for SLA than other methods due to the proprietary nature and limited availability of useful photopolymers. This method is therefore highly limited for real world production due to costs.

SLA has been around for 30 years, layers and lots of time, there is a scrap process. Carbon M1 looked at it and got rid of layers by controlling oxygen and light. Wider range of polymers, oxygen prevents liquid to turning into solid. UV light same but the combo with oxygen control makes the difference. DLP projector projects onto layer but the model ends up being



seamless. Wide range of resins for prototypes or real final production parts. Great method for light and strong 3-D meshes. “hardware, software and the chemistry make this all work! Control light and control oxygen, understand the physics and chemistry of light and oxygen.

### **Solid Ground Curing**

Similar to DMD, SGC uses the complete 2-D projection at once to cure the appropriate geometry of a single layer. The layer is then rinsed of uncured excess material, which is replaced by wax and then the entire layer is milled flat to provide a perfectly accurate and reliable surface for the next layer<sup>4</sup>.

### **Two-Photon Polymerization**

Femtosecond laser irradiation is referred to as two-photon polymerization in the context of creating a microchannel within a bulk polymer. The general concept has been exploring several exciting applications like photonic devices, nanosurgery, and materials processing<sup>166</sup>. This critical aspect of the technology is the laser, which is tuned to a specific wavelength based on the energy of the valence electrons in the bulk material. This laser has three parameters: pulse duration, pulse energy, and the focusing numerical aperture. By controlling these appropriately, the focused region of the laser pulse is excited to the point of ionizing many electrons, which in turn transfer energy to the matrix and cause structural changes. The changes can be very different, in some cases creating voids and in other cases changing the refractive index but not the phase. The focal area for femtosecond laser irradiation methods is its most compelling quality, at approximately 200 square micrometers. Due to the short duration and careful control of the timescale the laser pulses contact small areas without affecting surround material.

The field has explored silica in many forms and it is likely to be a plausible method for fabrication a 100 micron diameter tube with changes in diameter and wall thickness as small as 20 microns. Microfluidic devices can be fabricated using a two-part process of irradiating fused silicone, exposing the tube interior to laser pulses, and then etching the irradiated channels to become voids by using hydrofluoric acid.

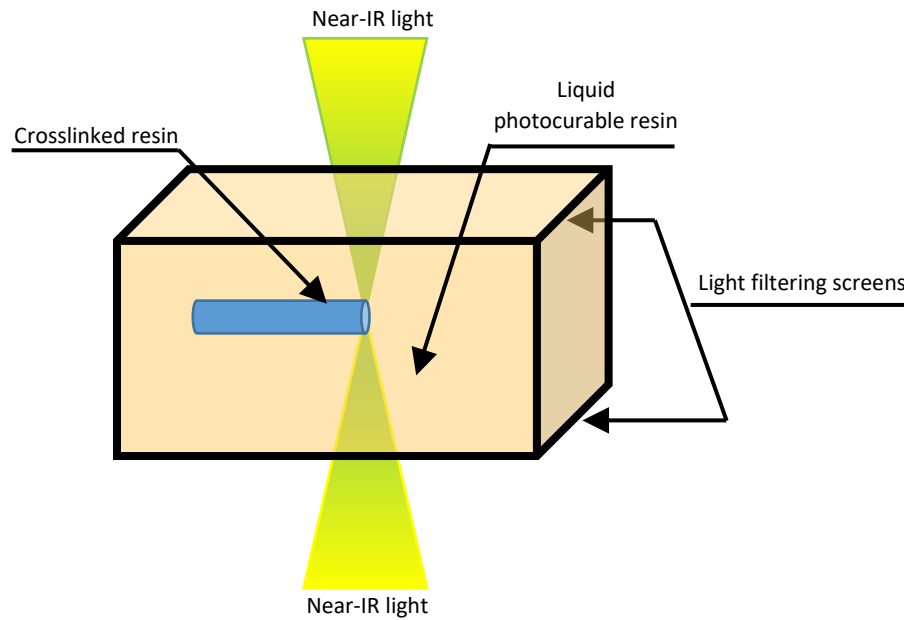


**Figure 27. Two photon polymerization in a static bath. In the focal point of the near-infrared laser beams, the custom-made photosensitive polymer solution is crosslinked.**

This is an emerging state-of-the-art laser technique. In this method, light is used to trigger the chemical reaction of photosensitive material. Unlike other light curing methods of fabrication, 2PP initiates the polymerization through irradiation with near-infrared femtosecond laser pulses of 800 nm. In the focal point, a suitable photoinitiator will absorb two photons, each with a wavelength of 800 nm, simultaneously, which causes them to act as one photon of 400 nm, thus starting the polymerization reaction. This nonlinear excitation triggers polymerization only in the focal point, leaving other areas unaffected. Therefore, this method has a potential

solidification resolution below the diffraction limit of applied light, making it superior in accuracy and resolution to all other solid freeform fabrication techniques.

### *Nozzle Based Systems*

#### **Fused Deposition Modelling**

Also known as fused filament fabrication (FFF), FDM works by laying down consecutive layers of hot material, which is allowed to cool and bond to adjacent layers before depositing the next layer. Print tolerances range from 0.05mm to 0.5mm with 0.2mm as the industry average in 2014<sup>4</sup>. The ability to control infill, and therefore production time and cost is one of the major benefits of FFF. Additionally, controlling infill is useful for creating insulating cavities within an object, which is difficult or impossible with other methods of fabrication and provides certain performance benefits under thermal loads<sup>207</sup>. While FFF has become popular for mainstream rapid prototyping applications it is limited in biological applications due to thermal load on the hydrogel or filament material. Nonetheless several medical grade polymers can be formed this way<sup>3</sup>.

#### **Freeform Reversible Embedding**

This method involves printing into a tank that is filled with a fluid that has the same density as the hydrogel extruded. This controls flow properties after leaving the nozzle. The material can then be extruded and holds its shape, then it is crosslinked and forms a solid. This solid is removed and the supporting material is broken down by one of several methods depending on the material. This leaves only the embedded print remaining. Stellar research with the method<sup>208</sup>.

### Pressure-Actuated

Potentially the most relevant, cost effective and high quality method for prototyping TE scaffold, pressure actuated nozzle systems have shown excellent results when coupled with no toxic photoinitiators for crosslink initiation. Additionally, these systems offer a range of futuristic possibilities as nozzles become more advanced and smaller. Nozzles surrounded by an annulus have been used to extruded tubes of 0.1mm diameter by using initiator flow in core nozzle and hydrogel flow in the annulus. The size of the nozzles available is currently advancing below 0.8mm diameters, but slowly because this is a challenging engineering project of its own. Pressure based systems offer flexibility, simplicity and appropriate refinement for productive research in fabricating TE scaffolds<sup>4,120</sup>.

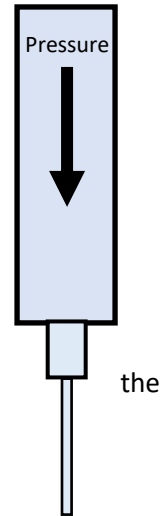


**Figure 28. Pressure-based extrusion uses a simple nozzle geometry to control flow rate.**

Pressure based systems are limited by the viscosity of the hydrogel, because low viscosity hydrogels are difficult to work with in this fabrication method. Exact dosing methods from solenoid, piezoelectric and volume actuated extrusion resolves this low viscosity problem, however the cost and reliability of pressure-actuated extrusion are strong qualities.

### Solenoid-Actuated, Piezoelectric-Actuated, and Volume-Actuated

Similar to pressure actuated, but use different mechanical mechanisms to extrude the hydrogel. ViscoTec demonstrates a great application to nozzle based systems with their metering nozzle that is solenoid actuated. A piston in the nozzle rotates and extrudes an exact volume of hydrogel, therefore ideally controlling the flow rate, dripping and any non-Newtonian

flow behavior. This dosing technology has applied well for silicone modeling with nozzle-based RP<sup>209</sup>.

### *Printer Based Systems*

Important to the context of all 3-D printing technologies because of their numerous applications and prolific development since the early 1900's, printer based systems direct link with electrical signals. Perhaps the least relevant modern technology for hydrogels and scaffold fabrication, printer based systems have manufactured myriad of biocompatible constructs from PEO, PCL, collagen/PDL mixtures, collagen, fibrin, alginate with CaCl<sub>2</sub>, polyurethane, among others<sup>3</sup>.

#### **Inkjet Printers**

There may be room to confuse this with other nozzle based systems because printer-based system is a loosely used term. Specifically, printer based systems are manufacturing techniques that implement inkjet technology. Inkjet printers exist in two types: drop-on-demand and continuous ejection. Drop-on-demand systems use electrical signals to control the ejection of individual droplets. Continuous ejection systems continuously deposit ink/material under pressure, this jet is then directed by electrical signals into a train of droplets to be deposited precisely.

#### **3D Printing™**

Trademarked by MIT and Professor Emanuel Sachs this is a solid-phase RP technology. This fabrication technology can be used to make parts out of various materials including ceramic, metal, composites and polymeric materials. The system works by depositing a layer of powder in a thin plane along the z-axis, which is smoothed by a roller causing excess to fall into

an overflow tank. An inkjet print head then prints a liquid binder onto the plane to bond the adjacent particles together. Essential to the process are biocompatible powder-binder systems. One documented advantage of this method is improved cell attachment to the rough surface that created by this powder based system<sup>24,59,210</sup>. In the case of direct inkjet writing (DIW), the construct is built up by the liquid itself.

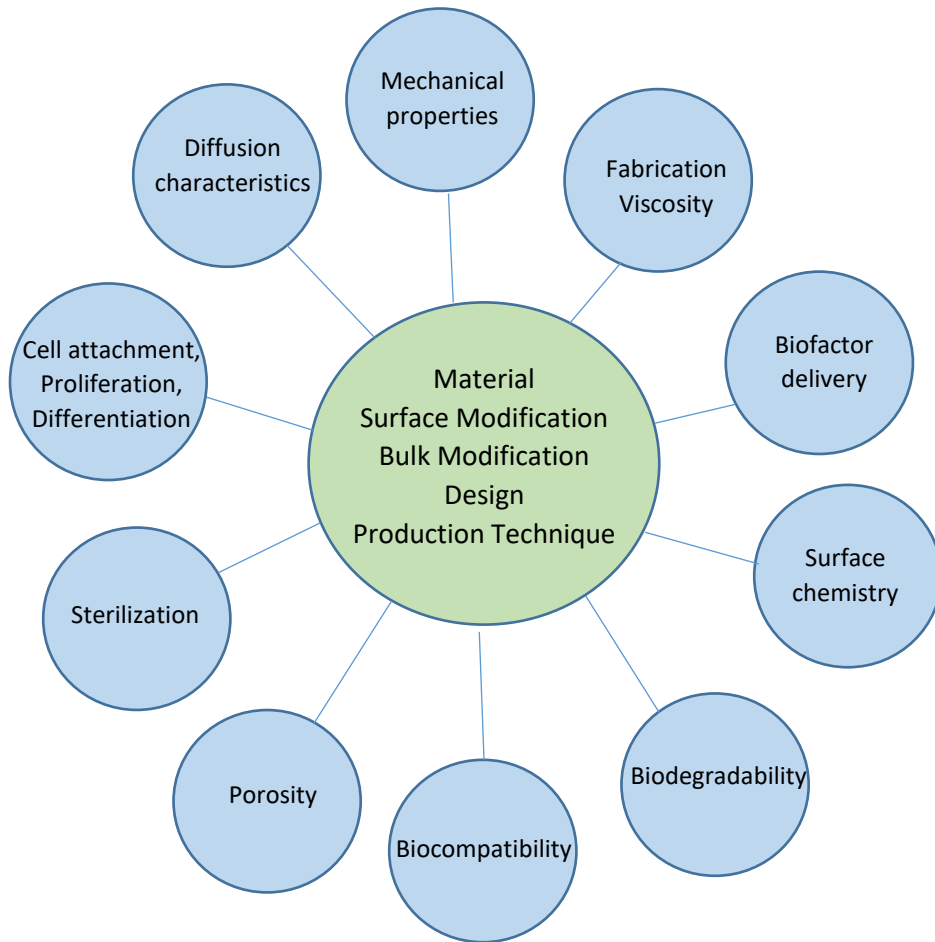


**Figure 29. Multi-disciplinary requirements that determine the constraints for ideal TE scaffold design.**

**Table 6. Rapid prototyping techniques and attributes <sup>2-4</sup>.**

RP Method	Abbreviation	Strengths	Weaknesses	Resolution	Porosity
Selective laser sintering	SLS	Accuracy, design flexibility, material flexibility, material cost	Manufacturing costs, production speed	10 $\mu\text{m}$	<80%
Stereolithography	SLA	Accuracy, design flexibility	Material flexibility, material costs, production speed, shrinkage from water evaporation, post curing essential, cytotoxic photo-initiator	30 $\mu\text{m}$ ; 1 $\mu\text{m}$ for $\mu\text{-SLA}$	<90%
2 photon-polymerization	2PP	Superior resolution	Manufacturing costs, small scale, shrinkage from water evaporation, diffusion driven polymerization results in undesired crosslinking	<diffraction limit of applied light	N/A
Fused deposition modeling or Fused filament fabrication	FDM or FFF	Material costs, production speed, design flexibility	Accuracy, overhang features, melt process	200 $\mu\text{m}$	<70%
Precise extrusion manufacturing	PEM	Accuracy, material flexibility	Manufacturing costs, melt process	100 $\mu\text{m}$	<90%
Pressure-assisted microsyringe	PAM	Accuracy, manufacturing costs, fabrication of microchannels, nozzle flexibility	Narrow range of printable viscosities, solvent used, highly water-soluble materials do not work	7-500 $\mu\text{m}$	<70%
Direct ink writing	DIW	Manufacturing costs, broad applications, accuracy	Low mechanical strength, smooth surface, low accuracy, slow processing	5-100 $\mu\text{m}$	<60%
Low temperature deposition modeling	LDM	Direct cell seeding, biocompatible	solvent is used, requires freeze drying	300-500 $\mu\text{m}$	<70%
Drop-on-demand	DOD	Accuracy, print area	Material flexibility, overhang features, material strength	200 $\mu\text{m}$	<50%
Continuous ejection		Material costs, caustic polymerizations, elastic materials	Accuracy, material flexibility, overhang features, high viscosity	200 $\mu\text{m}$	<70%
3D Printing™		Material strength, accuracy, biocompatibility	Material flexibility, material costs, post processing	100 $\mu\text{m}$	<90%

While the various methods for rapid prototyping provide numerous fabrication methods for elastomeric water-based constructs, the production of a viable TE scaffold using biocompatible hydrogels seriously limits the possible fabrication methods. These limitations are mostly related to caustic levels of light exposure, caustic chemical catalysts for polymerization, and excessive heat for thermal crosslinking methods. Additional limitations involve printing overhanging features and complex curves of the aortic wall, which cannot be accomplished with many methods as noted in the table. In summary, laser-based methods are costly and intensive because of chemical resins that must be prepared in excess to fill entire print area, printer-based methods are well developed but less practical for hydrogels than powders and thin

adhesives, and finally nozzle-based systems provide several compelling options for rapid prototyping scaffolds for exhaustive testing of many iterations of a similar hydrogel that can be crosslinked in a polymerization reactions that are inert and result in biocompatible constructs.

## Bioreactor

The bioreactor is designed for two steps: cell seeding and scaffold development. First, the bioreactor is used to statically, or dynamically, saturate the scaffold through passive, or dynamically assisted, diffusive force with a perfusion solution full of nutrients, growth factors and approximately  $1 \times 10^7$  cells per ml<sup>211</sup> in order to seed the scaffold with sufficient cells to create a functional ECM in turn. Second, the seeded scaffold is placed in the bioreactor to circulate, diffuse, a nutrient soup to the lumen of a vascular scaffold. The exterior of the scaffold is not circulated but it is maintained in a separate static solution. In order to biochemically and mechanically stimulate the scaffold to synthesize new collagen and create the extracellular network for mechanical strength and communication the solution and the pulsatile flow are tuned to maintain the fastest possible growth rate of collagen in the extracellular space within the scaffold. After days of cell seeding and 7-10 weeks of development<sup>37,212</sup> elicited by mechanotransduction and chemical cell signaling, the material properties of the scaffold increase to native vessel burst pressures of >1,700 mmHg for the saphenous vein<sup>24</sup>. Ideally, the bioreactor process mimics embryonic development but expedites the process by starting with the full size scaffold geometry and advancing the cellular proliferation throughout the scaffold in an unnatural way. Although outside of natural developmental time frames, the cells are unaltered and the subsequent development will potentially create a completely natural ECM and the expeditious development will not affect the long term patency of the vessel.



## Cell Adhesion

The cell attachment is accomplished by scaffold design but also by intelligent design of the cell seeding method. Cell attachment is achieved by constructing the scaffold with sufficient diffusivity and pore size for cell infiltration into the bulk material where cells can attach to recognizable molecular bonding sites on the scaffold matrix. Then a specific seeding bioreactor is used to statically or dynamically seed healthy cells into the scaffold and aid in adhering them with covalent bonds to the prefabricated scaffold. Static seeding has been shown to have remarkable results by simple passive diffusion and the mobility of the cells themselves. It is noteworthy that rotational and vacuum chamber cell seeding have shown promise for increasing seeded cell density. Cells have been shown to attach to most of the materials in this chapter, however the propensity for cell adhesion to the scaffold varies and the ability of the scaffold to convey mechanotransduction appropriately is dependent on the exact geometry and conformation of the attachments of cells to the matrix.

Scaffold design determines the water % in the hydrogel, the pore size of the matrix, the diffusion coefficients for different solutes, and the attachable moieties on the molecular matrix. Once these are chosen, the purpose of the bioreactor is to seed cells as effectively as possible into the scaffold material with an even distribution throughout the thickness. Challenges remain to achieve fully homogenous cell distribution in the bulk material, due to the propensity to attach near to the surfaces, which is a potentially important reason to fabricate thin scaffolds that can gain thickness over time with natural development and distribution of cells as they migrate within the ECM being created.

In order to attach the vascular scaffold within the bioreactor a compliant silicone tubing has proven functional<sup>213</sup>. The seeded scaffolds with VICs and SMCs are stimulated by adding 10% carbon dioxide at 37°C<sup>211,212,214</sup> once the pulsatile flow is started. According to several research groups, the pulsatile flow protocol should be started 5 days after seeding (165 beats per minute, 1% radial distention<sup>213,214</sup>). Ascorbic acid is replenished twice weekly and the bioreactor perfusion medium is replaced each week. Once the construct has developed sufficient

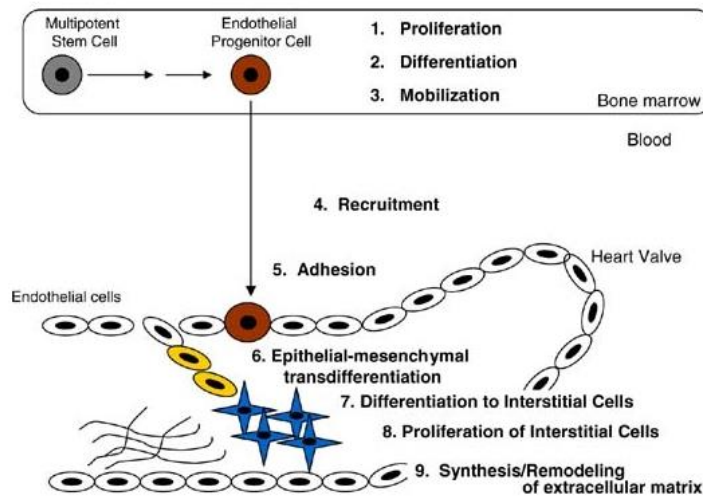


**Figure 30. A depiction of the infiltration of a tissue engineered scaffold by endogenous cells. Proliferation, differentiation and mobilization of the endothelial progenitor cells within the bone marrow releases multipotent stem cell into the blood, where they are recruited by and adhere to the valve VECs. Subsequently, recruited cells may undergo a transdifferentiation from endothelial to mesenchymal phenotype, and further differentiation to interstitial cells that ultimately synthesize, degrade and constantly remodel the ECM<sup>5</sup>, with permission.**

mechanical properties the lumen is endothelialized. To form the endothelial layer,  $1 \times 10^6$  endothelial cells per ml are added to the perfusion solution into the lumen of the vessel and allowed to adhere in a static environment for 6 h. Flow is gradually increased to  $0.3 \text{ N/m}^2$ , which approximates venous shear stress, and vessels are able to be harvested after 24 hours of normal venous shear stress. Several methods corroborate this method based on pulsatile mechanotransduction and time frames<sup>32,65,37,65,215,65,216,65,217,65</sup>.

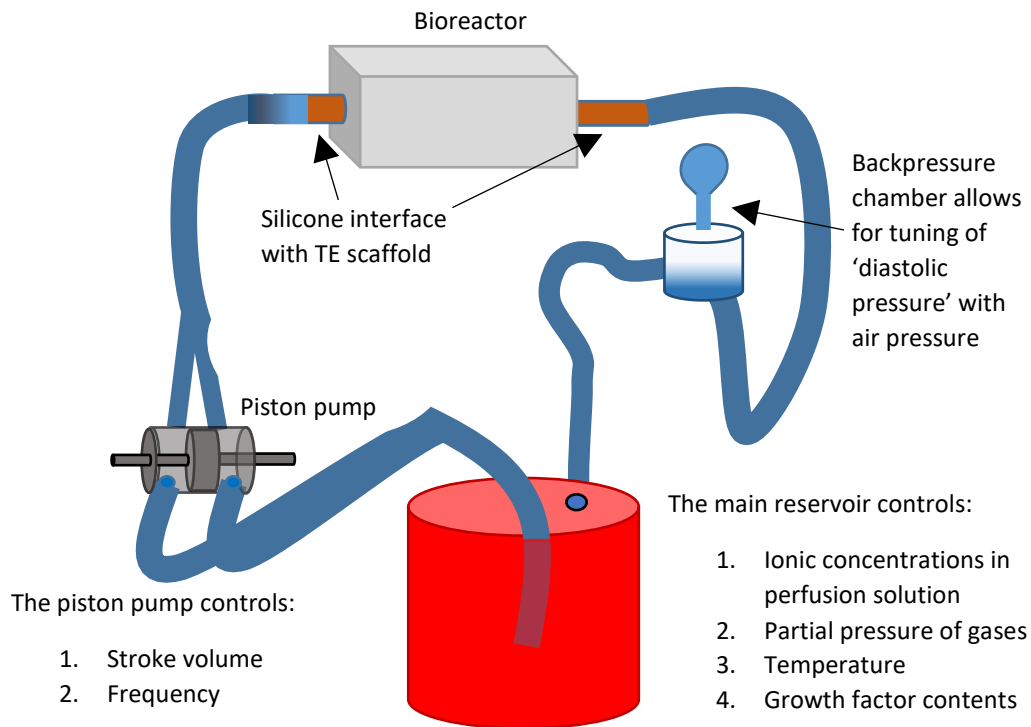


Figure 31. Bioreactor schematic drawing showing the heated reservoir of optimal perfusion solution, piston pump, reactor chamber, backpressure chamber and silicone tubing.

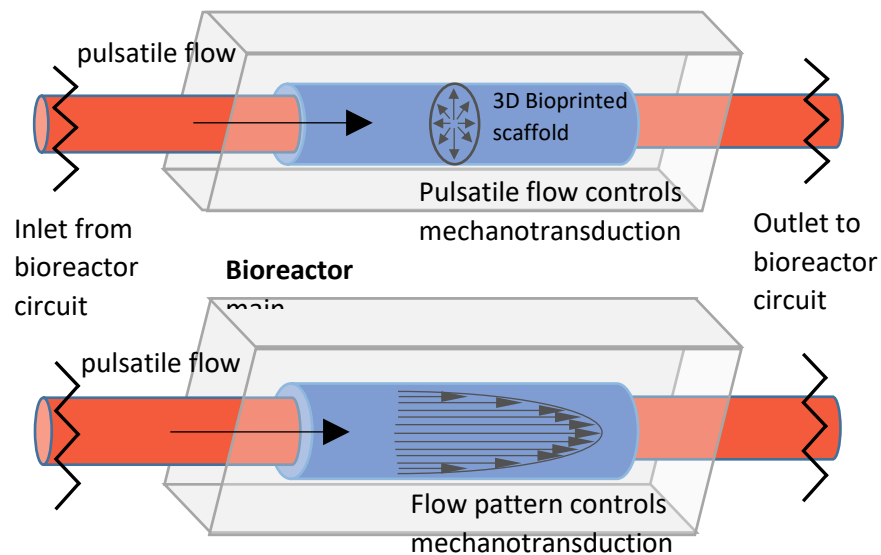


Figure 32. Mechanotransduction dynamics of the pulsatile bioreactor setup. *Top*, in the bioreactor chamber circumferential stress is imparted by pulsatile flow in order to elicit an interstitial cellular response to remodel the ECM. *Bottom*, in the bioreactor chamber shear stress is imparted by the velocity gradient of the flow to elicit an endothelial cell response. In both cases intercellular junctions and mechanical linkages propagate signals widely throughout the tissue.

This procedure underlines the propensity for cell to attach to scaffold made from the group of biocompatible polymers. It also emphasizes the ease with which cell can be multiplied and the relative importance of this element of the cell seeding process because without the high concentration of cells, the diffusion will not progress rapidly due to the lower concentration gradient and the governing transport properties in the bioreactor. In addition to cells, the

**Table 7. Formula of high glucose DMEM from ThermoFisher Scientific <sup>7</sup>.**

Components	Molecular Weight	Concentration (mg/L)	mmol/L
<b>Amino Acids</b>			
Glycine	75	30	0.4
L-Arginine hydrochloride	211	84	0.39810428
L-Cystine 2HCl	313	63	0.20127796
L-Glutamine	146	584	4
L-Histidine hydrochloride-H <sub>2</sub> O	210	42	0.2
L-Isoleucine	131	105	0.8015267
L-Leucine	131	105	0.8015267
L-Lysine hydrochloride	183	146	0.7978142
L-Methionine	149	30	0.20134228
L-Phenylalanine	165	66	0.4
L-Serine	105	42	0.4
L-Threonine	119	95	0.79831934
L-Tryptophan	204	16	0.078431375
L-Tyrosine disodium salt dihydrate	261	104	0.39846742
L-Valine	117	94	0.8034188
<b>Vitamins</b>			
Choline chloride	140	4	0.028571429
D-Calcium pantothenate	477	4	0.008385744
Folic Acid	441	4	0.009070295
Niacinamide	122	4	0.032786883
Pyridoxine hydrochloride	206	4	0.019417476
Riboflavin	376	0.4	0.00106383
Thiamine hydrochloride	337	4	0.011869436
i-Inositol	180	7.2	0.04
<b>Inorganic Salts</b>			
Calcium Chloride (CaCl <sub>2</sub> ) (anhyd.)	111	200	1.8018018
Ferric Nitrate (Fe(NO <sub>3</sub> ) <sub>3</sub> ·9H <sub>2</sub> O)	404	0.1	2.48E-04
Magnesium Sulfate (MgSO <sub>4</sub> ) (anhyd.)	120	97.67	0.8139166
Potassium Chloride (KCl)	75	400	5.3333335
Sodium Bicarbonate (NaHCO <sub>3</sub> )	84	3700	44.04762
Sodium Chloride (NaCl)	58	6400	110.344826
Sodium Phosphate monobasic (NaH <sub>2</sub> PO <sub>4</sub> ·H <sub>2</sub> O)	138	125	0.9057971
<b>Other Components</b>			
D-Glucose (Dextrose)	180	4500	25
Phenol Red	376.4	15	0.039851222
Sodium Pyruvate	110	110	1]

perfusion medium in the bioreactor is full of nutrients and growth factors that are essential for cellular activity and for synthesizing new collagen molecules to arrange in the ECM. The list of all of those are listed. The goal is to use cytokines and growth factors to elicit strong response from the cells to synthesize new ECM. Overall, the mechanotransduction of the bioreactor is as important as the quality of the perfusion solution and equally important as the scaffold material<sup>218</sup>.

In addition to the nutrient rich basic medium, DMEM, fetal bovine serum FBS is used to supplement the amino acid profile of the perfusion solution in the bioreactor. FBS contains no cells or clotting factors, but it is rich in amino acids, fatty acids, trace elements, lipids, and vitamins. Hormones that act as attachment, migration, proliferation and differentiation stimulants are abundantly present in FBS. Cell attachment as well as mobility of cells is assisted by the presence of binding and transport proteins that also help in carrying other molecules from the medium into the cells and between cells. Finally, detoxifying factors in FBS aid in disposal and deactivation of proteases which degrade and erode cell junctions and integrins with the ECM of the scaffold. In the current research, 5-20% v/v FBS is added to the bioreactor perfusion solution.

Also important to the bioreactor is antibiotic factors, which prevent bacteria from growing in the culture medium. Penicillin/streptomycin is common used at 1% v/v to aid in proper cultivation of the scaffold. Fungizone is sometimes used to reduce the risk of fungal contamination.

Lastly, vitamin C (L-ascorbic acid), basic fibroblast growth factor (bFGF), transforming growth factor (TGF- $\beta$ 1), insulin and sometimes an additional pH buffer, HEPES (4-(2-hydroxyethyl)-1-piperazineethanesulfonic acid), are added. However, control over the CO<sub>2</sub> levels

in the perfusion solution as well as the sodium bicarbonate in the DMEM make control over pH possible without the addition of HEPES.

In our approach the scaffold created is a high water content, large pore size matrix, highly degradable scaffold that will go from low mechanical properties to cell infiltrated quickly and the cells can build the ECM in the easiest environment possible to create the most organized ECM possible. Along with extrusion based 3-D bioprinting, this combination of current technologies shows promise for several reasons explored in the laboratory work of next chapter.

## CHAPTER 4: MATERIALS AND METHODS

### Hydrogels

Lithium phenyl-2,4,6-trimethylbenzoylphosphinate (TCI Chemicals, Portland, OR) was mixed at 1% w/w ratio to poly(ethylene glycol diacrylate) average  $M_n$  700 in PBS solution at 60°C. PEGDA 700 was added to the LAP solution at concentrations from 5, 10, 15, and 20% w/v and vortexed for 30 minutes under protection from UV. After mixing, the monomer solution with photoinitiator was transferred and centrifuged for 15 minutes. The resultant PEGDA solution was allocated into a 5ml viscometry sample and the remainder was cast in 0.338 ml cuboids for biaxial mechanical testing.

Separately, (hydroxypropyl)methyl cellulose (H7509, Sigma-Aldrich, St. Louis, MO) 1, 2, and 4% w/v was solubilized in 25°C PBS<sup>219</sup>. To mix the composite hydrogel, equal volumes of

**Table 8. The table shows the best hydrogel composition.**

Weighout:		Polymer solution with photoinitiator			Volume, mL
Ingredient:	Density, g/ml	Weight, grams:	Baker's %:	w/v	
PEGDA MW700 at 15°C	1.100	3.00	78.9%	15.0%	2.73
PEGDA MW6000 at 15°C	10.000	0.40	10.5%	2.0%	0.04
Gelatin from porcine skin Type A	4.000	0.00	0.0%	0.0%	0.00
PEO - 12-50 cP, 5 % in H2O	5.000	0.00	0.0%	0.0%	0.00
Hydroxypropyl methylcellulose	2.000	0.40	10.5%	2.0%	0.20
Sodium Alginate	10.000	0.00	0.0%	0.0%	0.00
Collagen, Type I	1.004	0.00	0.0%	0.0%	0.00
Calcium Chloride	10.000	0.000	0.0%	0.0%	
NaOH	1.000	0.000	0.0%	0.0%	0.00
LAP	10.000	0.060	1.6%	0.3%	0.01
Deionized Water	1.000	17.027	448%	80.7%	17.03
Set desired volume total, mL	20			100.0%	20.00

cellulose and PEGDA-LAP solution (at double concentrations of 10, 20, 30, and 40% w/v PEGDA 700) were combined and vortexed for 60 minutes while returning to room temperature passively. 10ml of each hydrogel was loaded into 10ml syringe and centrifuged for 15 minutes to degas and concentrate any insolubilized particles at the outlet. The final hydrogel is then allocated into two 5ml samples for viscometry and mechanical testing, while the remaining hydrogel was loaded into 10ml syringes and used for 3-D printing into scaffold geometry.

Additionally, the properties of mixtures were tested by combining gelatin(Sigma), polyethylene oxide Mn 100,000 (Sigma), alginate, or polyacrylamide Mn 40,000 (Sigma) with cellulose hydrogel. Separately mixed cellulose solution 4% w/v was mixed into the PEGDA 90% w/v solution at a ratio of 3:1 v/v and vortexed 15 minutes before adding premixed gelatin, PEO, alginate, or polyacrylamide solution 12% w/v at a ratio of 1:2 v/v of PEGDA-cellulose solution. This made comparable hydrogels with 4% w/v of the additional molecule in a 15% PEGDA 700 w/v 2% HPMC w/v photoinitiated hydrogel. The blended solutions were vortexed for 60 minutes under protection from UV while passively approaching room temperature. This results of these extra tests are included in the appendix.

The best performing hydrogel was mixed with PEGDA average  $M_n$  6,000 2% w/v while increasing total LAP 0.02% w/v. The addition of longer chain monomers has been shown to increase fracture strain <sup>7</sup>. Additions like this are critical to tuning the mechanical properties of the crosslinked hydrogel, however due to the costs of synthesizing and purifying larger MW monomers, PEGDA 6,000 is far more expensive than PEGDA 700.



## Viscometry

A viscometer (CVO, Bohlin Instruments, Malvern, UK) was used to test viscosity of 2ml samples of hydrogel across the relevant shear rates between 0.0123 and ~1000 1/s in 100 linear increments while keeping temperature at 25°C or 37°C. The c440 cone and plate geometry was used with the CV software program (Bohlin). The software creates a viscosity as a function of shear stress graph, which is manually translated to a plot shear stress as a function of shear rate and then fit to a Newtonian (1) or Power-Law (2) model.

$$\mu = C\gamma \quad (4.1)$$

$$\mu = K\gamma^n \quad (4.2)$$

$$\mu = \mu_0 e^{\frac{E_\mu}{RT}} \quad (4.3)$$

The dependence of viscosity on temperature is shown in an Arrhenius-type equation, where  $\mu_0$  is a reference viscosity at a certain temperature,  $E_\mu$  is the temperature coefficient for viscosity,  $R$  is the universal gas constant and  $T$  is the relevant temperature.

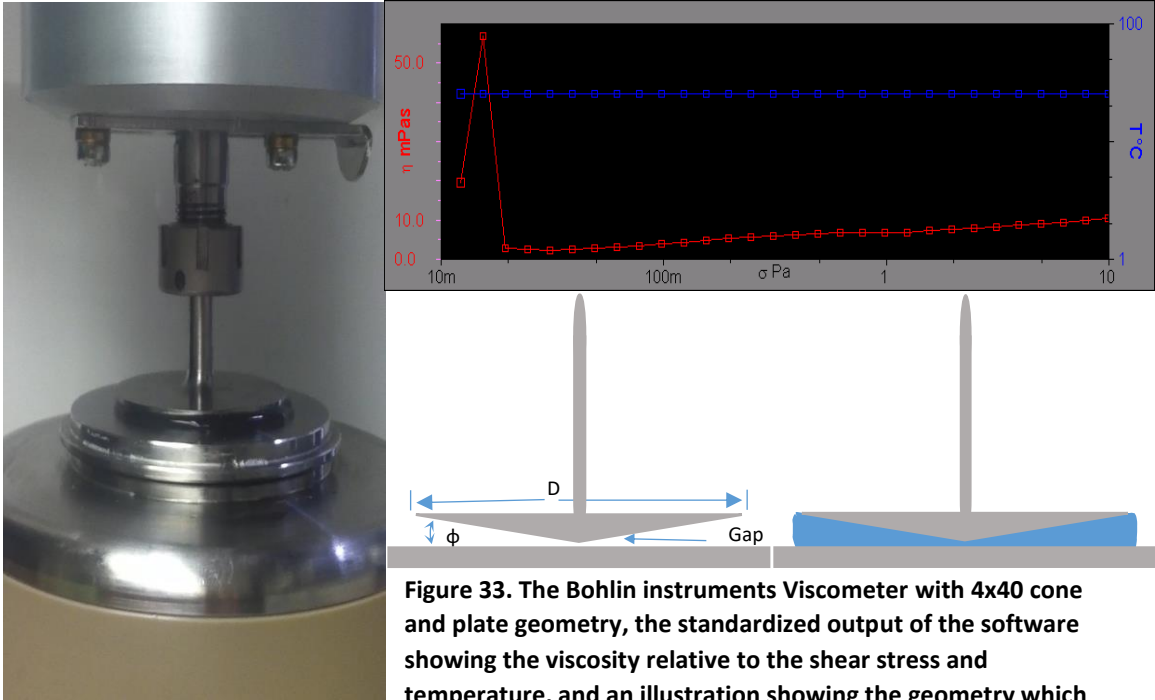


**Figure 33. The Bohlin instruments Viscometer with 4x40 cone and plate geometry, the standardized output of the software showing the viscosity relative to the shear stress and temperature, and an illustration showing the geometry which uses a gap size of 150μm.**

In a cone and plate viscometer, the angular velocity of the plate is zero while the cone rotates clockwise creating a shear between the top and bottom layers, while the rotational body of fluid has no radial velocity gradient. The velocity gradient is set by the cone angle, the gap size and the angular velocity. The diameter of the cone allows for sufficient sample size and balances centripetal forces of the small system. The angular velocity together with the cone angle and diameter give linear velocity along the cone surface, which extrapolates into the complete strain rate profile (constant throughout). Torque is measured instrumentally and viscosity is computed.

$$\tau = \frac{3M}{2\pi R^3} \quad (4.3)$$

The equation for the torque, M, conversion to shear stress on the fluid top surface with radius R.

$$\dot{\gamma} = \frac{\Omega}{\alpha} \quad (4.4)$$

The equation for shear rate in terms of angular velocity,  $\Omega$ , and cone angle,  $\alpha$ .

$$\mu = \frac{\tau}{\gamma} = \frac{3\alpha M}{2\pi R^3 \Omega} \quad (4.5)$$

In terms of viscosity, the ratio of the total torque relative to the cone angle are directly proportional, while the surface area and angular velocity are inversely related to the viscosity.

$$k = \text{Manufacturer's specification} = \frac{3\alpha}{2\pi R^3} \quad (4.6)$$

Ultimately, the manufacturer only needs to supply the coefficient  $k$  in order to allow users to correlate angular velocity with viscosity<sup>204</sup>, that is the dependence of viscosity on shear rate.

The viscometry data is insightful and informs the computer simulation of extrusion by setting an initial parameter for viscosity. However, extrusion of hydrogels under experimental conditions (microchannel flow) provides a more relevant description of viscous behavior for our 3-D printing purpose than the cone and plate geometry, or bob and cup geometry. Furthermore, flow of oil through tubes by hydrostatic pressure has long been the most trusted method of characterizing the viscous behavior of oils.

## Surface Tension

A Sigma 700 Tensiometer was used to measure interfacial tension. A du Nouy ring made of platinum (Boilin Scientific, ) was used to measure the surface tension of the fluid in room air. The du Nouy ring must be well cleaned and sterilized with a Bunsen burner (>500C) until it glows red hot. The hydrogel was prepared by partially filling a 100ml dish with fluid and allowing it to set before suctioning off the surface layer before beginning testing. This purifies the interfacial

layer and minimizes error. The sterilized ring was affixed to the instrument before initiating 8mm pulls from 3mm below the surface of the fluid. As the ring lifts through the interface the force hits a maximum value, which reflects the breaking point of the surface tension at the interface. Surface tension measurements are applied to calculate the Capillary number, Weber number, and Bond number. These relevant dimensionless parameters define a given hydrogel by relating the viscous, inertial, and gravitational energies to the surface tension energy.



**Figure 34. Picture of whole apparatus and close up of the platinum du Nouy ring.**

While surface tension does not necessarily convey surface chemistry of the crosslinked scaffold, surface energy at the interface provides information about the hydrogel at the molecular level that alludes to the cohesion of the surface molecules. The importance of surface properties is well established by research so we apply the tensiometer to uncover any correlations to extrusion flow rate and scaffold surface properties.

The surface tension data along with flow pattern information allows for the extrapolation of the relative importance of factors affecting the hydrogel as it flows through the extrusion geometry. The flow regime is characterized by several equations that relate viscous and surface forces to the momentum of the fluid flow. Calculations for shear stress at the wall

and viscous losses within the extrusion system are informative about the dissipation of pressure energy into viscous losses and interfacial forces. The Reynolds number, Capillary number, Euler number, and Weber number were also calculated to characterize the hydrogel in the extrusion geometry. These dimensionless parameters given certain insight to the CFD simulation settings and they also provide a context for comparing one hydrogel to another in an unbiased manner.

$$\text{Wall shear stress, } \tau = \frac{r}{2} \times \frac{\Delta P}{L} \text{ or } \tau = \frac{4\mu U_{avg}}{r} \quad (4.7)$$

$$\text{Friction Factor, } FF = \frac{64\mu}{\rho D U_{avg}} \quad (4.8)$$

$$\text{Head Loss, } H.L. = FF \times \frac{L \cdot U_{avg}^2}{2D} \quad (4.9)$$

$$\text{Reynolds' parameter, } Re = \frac{\rho V D}{\mu} \quad (4.10)$$

$$\text{Capillary Number, } C = \frac{\mu V}{\gamma} \quad (4.11)$$

$$\text{Euler Number, } E = \frac{\Delta P}{\rho V^2} \quad (4.12)$$

$$\text{Weber Number, } We = \frac{\rho V^2 L}{\gamma} \quad (4.13)$$

$$\text{Surface tension, } \gamma = \frac{\text{Gibbs free energy}}{\text{Area}} \quad (4.14)$$

Where  $r$  is nozzle radius,  $\Delta P$  is total pressure loss,  $L$  is nozzle length,  $\mu$  is hydrogel viscosity,  $D$  is nozzle diameter,  $V_{avg}$  is average flow velocity at the outlet,  $\rho$  is hydrogel density, and Gibbs free energy defines the energy to dissociate the surface. Gibbs free energy of a surface will decrease as temperature increases, which explains the inverse relationship between temperature and surface tension.

## Computational Fluid Dynamics

The viscous flow of hydrogel extruding from the 3-D printer was simulated using ANSYS Fluent CFD analysis. ANSYS Fluent (location) was used to illuminate the effect of non-Newtonian flow properties of the hydrogels. The relationship between the pressure setting and the expected flow rate was plotted for the chosen nozzle size, 0.21mm diameter and 25.4mm length (Jensen Global), as a guide for configuring the printer settings. Initially, several geometries were analyzed in order to understand the effects of the shape of the boundary in the extrusion setup. The mesh was designed to be mapped to the orthogonal walls in order to create a uniform mesh with aspect ratio of 1 across all elements. An axisymmetric 2-D laminar model was used to simulate the extrusion efficiently. The pressure difference between the inlet and outlet was obtained from experimental validation testing and applied to the boundary conditions for the inlet and outlet for the simulations. No-slip boundary conditions were applied to the 5 walls of the axisymmetric geometry, and a symmetry was applied to the axis as a boundary condition. A first-order implicit steady state formulation was utilized. Pressure-velocity coupling was handled using Simple scheme, and the spatial discretization of momentum equations were performed by the QUICK method. The results converged to residuals of  $< 10^{-6}$  in order to complete the simulations. The density of the hydrogel was set to equal the measured values from the scale  $1112.0 \text{ kg/m}^3$ . The viscosity was set to 500 cP for Newtonian and Power Law coefficients were set to  $K=5.5$  and  $n=0.52$ . The model decreases the configuration time for new hydrogels by extrapolating a small set of validated flow simulations for many different nozzle sizes and flow rates.

The geometry matches the instruments, pictured below, used with a change to the length of the syringe. Shortening the syringe decreases the number of elements, and associated

computational time, required for a high quality mesh, as well the head loss and velocity magnitudes are low in this entire section of the geometry. The geometry used in the simulation is shown and illustrates the shortening of the syringe length and the unchanged geometry of the nozzle and neck of the axisymmetric model. Even with this truncation, the number of elements to resolve the flow in the nozzle is remarkable.



**Figure 35. BD 10ml syringe and Jensen Global 0.21mm I.D. nozzle used. Jensen dispensing tips feature a polypropylene Luer Lock hub with a UV-bonded 304 stainless steel cannula.**

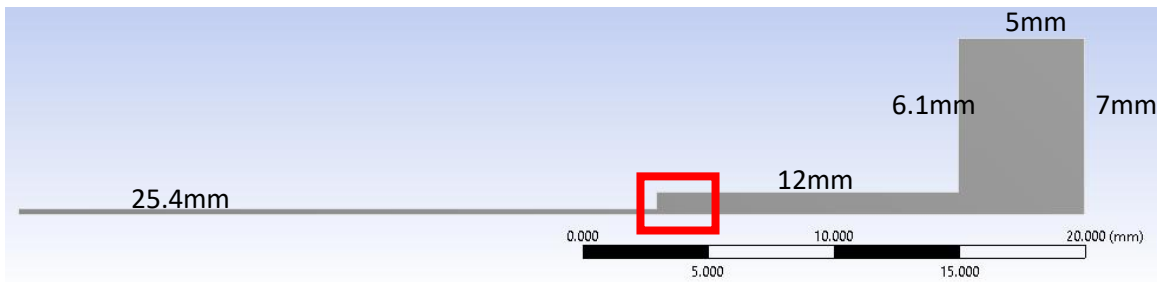


**Figure 36. Geometry with 0.254mm radius nozzle and 0.7ml hydrogel to decrease total elements, all angles are 90 degrees.**

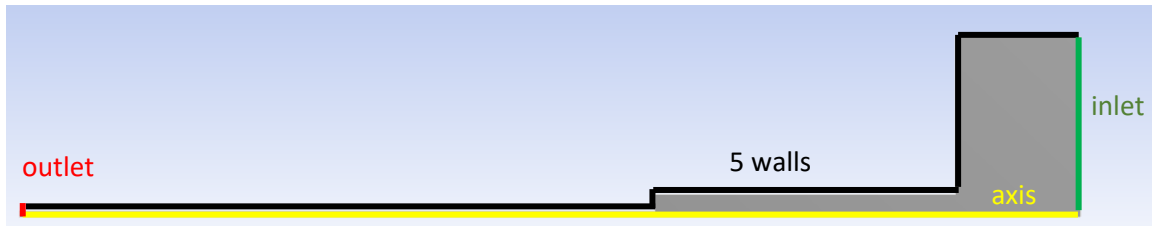


**Figure 37. Boundaries of the 2-D axisymmetric geometry.**

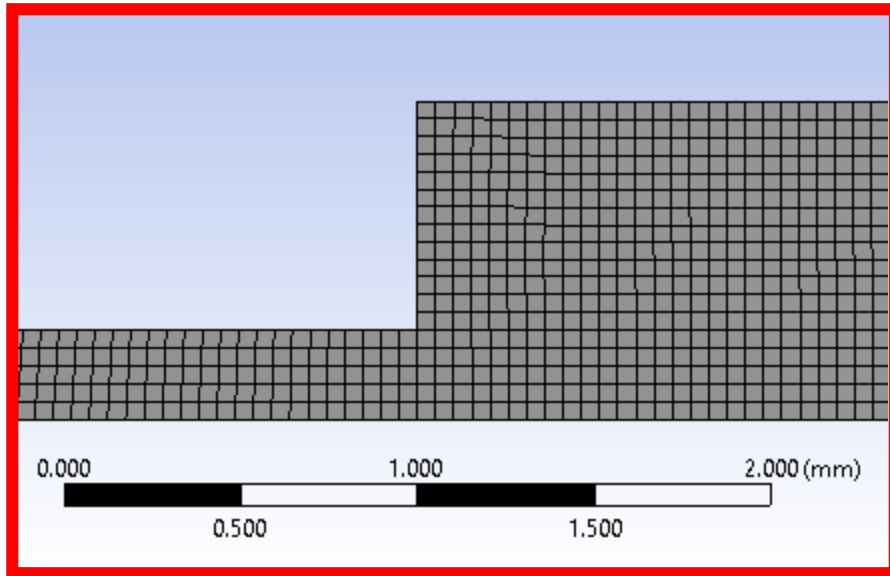


**Figure 38. Most basic mesh with 4 elements across the nozzle radius, total elements=13,283.**

The geometry and mesh were tested to obtain a mesh that produced results independent of further alterations to the mesh. As pictured above, the tested meshes are each orthogonal and mapped to the edges of the geometry to give a uniform mesh size throughout. The table below shows that the flow rates for the different meshes under a pressure of 10 psi change slightly at lower mesh densities, but flow rate levels off above 16 elements across the radius of the nozzle. 16 elements across the axisymmetric radius for the 2-D simulation became the standard mesh independence criteria for all meshes used.

**Table 9. Mesh independence study.**

Mesh Size as elements across outlet	Total number of elements in mesh	Volumetric Flow Rate (ml/s)
4	13,283	0.02850
8	53,132	0.02724
16	212,528	0.02688
32	850,112	0.02682
16 concentrated at nozzle	42,971	0.02683



Once a quality mesh was found, perturbations to the geometry, aside from nozzle specifications, were made to examine the effects of different shaped geometries on the pressure and flow relationship. This method gave insights to the flow pattern by thoroughly analyzing the effects of the geometry. Different constrictions as the nozzle narrows towards the outlet and nozzle shapes and sizes demonstrate the dynamics of the head loss as hydrogel flows through the entire geometry.

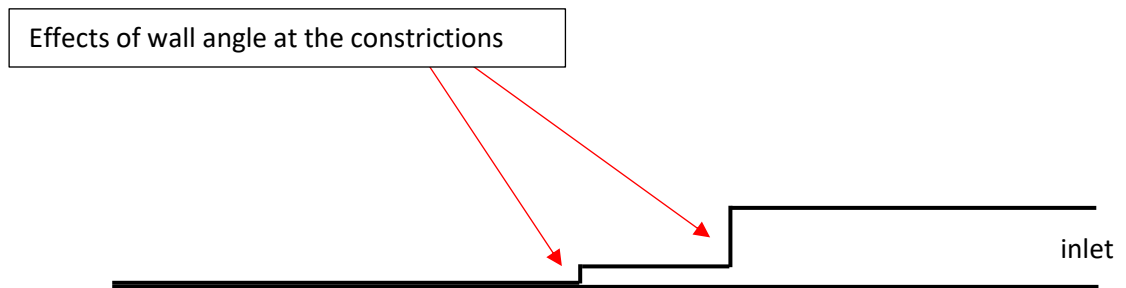


**Figure 39.** The basic geometry, 90° corners are shown, but simulations were performed to examine a range of wall angles while maintaining the dimensions of the inlet and the outlet as well as the distance between inlet and outlet.

The alternate geometries are shown in the results and include 89°, 91°, and 120° wall angles, which prove to illustrate the independence of the flow pattern from the flow boundary before the nozzle. Additionally, a syringe tapering from the inlet to the nozzle inlet simulated a simple streamlined design, and finally, a cone shaped nozzle geometry was tested. Testing these different geometry provides insight into the sources of headloss within the extrusion geometry, which improves the understanding of controls over the extrusion flow rate.



**Figure 40.** The tapered syringe design and the cone shaped nozzle geometry, each with same inlet and outlet dimensions

**Table 10. The boundary conditions and input parameters to the CFD simulation**

Input Parameters	Methods for Tuning Parameter
Geometry	Change nozzle diameter and length; change syringe shape and taper towards outlet
Pressure @ inlet & outlet	Match experimental
Viscosity	Start with viscometer, validate CFD with experimental testing
Wall treatment	No slip is used
Flow rate target	Match experimental tests

The benefit of running non-Newtonian CFD models for these hydrogels is that the experimental shear thinning behavior can be incorporated into the simulation parameters, potentially keeping the simulation accuracy high across a broad range of pressure settings. The Power law models are shown below and the equations used to obtain viscosity as a function of shear rate (the effects of temperature are described within but extrusion is maintained at room temperature in all cases).

Viscometry data was used for setting the initial viscous parameter and experimental testing was used for validation of the final viscous parameter. Since this is not a typical application of FLUENT it requires a numerical method to iteratively find the viscosity parameter as an optimization.

The extrusion test with the 3D printer to validate the CFD simulation was as follows. The pressure is set to an exact value that will be held constant while volume flow rate is measured. This value is around 20 psi for 500 cP hydrogels through 500 micron diameter nozzles. This test provides a set pressure value and geometry, and then observed flow rate is obtained to crosscheck the simulation flow rate and pressure. The ultimate goal of the CFD is to create a validated curve of the flow rate as a function of the pressure setting. With this information along with the specific geometry to be printed, the print settings can be optimally configured.

## Patient Specific Geometry

Since the geometry, wall thickness, height and overhanging features all effect the print settings and the overall hydrogel flow pattern it is fitting to discuss this other computer technology before getting to the printer configuration.

Computer tomography angiography (angiogram) images were adapted into Solidworks (Dassault Systèmes Waltham, MA) with Rapidform (Inus, Seoul, South Korea) in order to create a patient specific aortic root geometry STL file for importing into Slic3r software (open source). This geometry determines the wall thickness and dimensions, which are used to configure the slicing settings in concert with the pressure control setting and nozzle geometry.

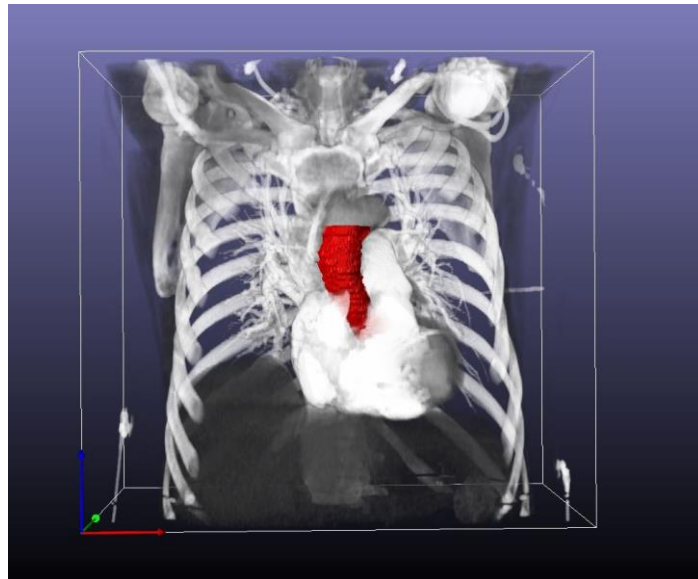


**Figure 41. (a) Medical image from CT scan is adapted with Rapidform into a Solidworks file before converting into a printable file format, (b) complete aortic root in Solidworks software showing the boundary surface and omitted coronary arteries (c) patient specific geometry file for 3D printing software, truncated for print quality.**

## Planar Biaxial Testing

Biaxial stress testing (CellScale, Waterloo, Canada) was used to understand the mechanical properties of molded hydrogel after crosslinking and 24 hrs in PBS bath at 25°C to remove unreacted particles and equilibrate unbonded water content. Two sets of orthogonal load cells (Model 31, Honeywell Inc., Columbus, OH) are attached to the sample by four tungsten CellScale BioRakes, which pierce the sample from above and hold it in the horizontal plane. Samples were lowered into a water bath at 25°C or 37°C dependent on the test. Graphite powder was added to the surface of the samples in order to track the deformation. Real-time displacement of the graphite was obtained at 15Hz from the superior-normal position. No preconditioning was performed before an equibiaxial strain of 50% with 4s duration to determine fracture conditions. Displacement data was tracked using CellScale LabJoy in order to calculate deformation gradient and green strain tensor for the center-element nodes.

### *Mold Preparation*

Mixed and degassed hydrogels were molded using 0.34 ml of 25°C hydrogel carefully distributed within 13mm by 13mm by 2.5mm casts. The hydrogel molds were covered and allowed to rest for 30 minutes after pouring. The casts were then placed under the 365nm UV light for 5 minutes at 25°C before 24 hrs of treatment in a PBS bath at 25°C in order to remove unreacted residues and reach a homeostatic water content. Sample thickness was measured with Mitutoyo Digital caliper (Model 500-754-10) before testing and remained within +/- 10% of 2mm. All samples were tested within 36 hours of crosslinking.

Molded articles were assumed to be incompressible due to the high water content. Predominantly, mechanical behavior was linear elastic so 3 tests were averaged and fit by linear

regression. Planar forces ( $F_{11}$ ,  $F_{22}$ ) applied to the sample by two load cells were distributed across the deformed cross-sectional area to ascertain Cauchy stresses ( $T_{11}$ ,  $T_{22}$ ).

$$T_{11} = \lambda_1 \frac{F_{11}}{t_0 l_0} \text{ and } T_{22} = \lambda_2 \frac{F_{22}}{t_0 l_0} \quad (4.7)$$

where  $t_0$  is the initial sample thickness, and  $\lambda=l/l_0$  is the stretch ratio of the deformed sample length to initial length. The Green strain tensors ( $E_{11}$ ,  $E_{22}$ ) were calculated using the following relationship <sup>220</sup>:

$$E_{11} = \frac{1}{2}(\lambda_1^2 - 1) \text{ and } E_{22} = \frac{1}{2}(\lambda_2^2 - 1) \quad (4.8)$$

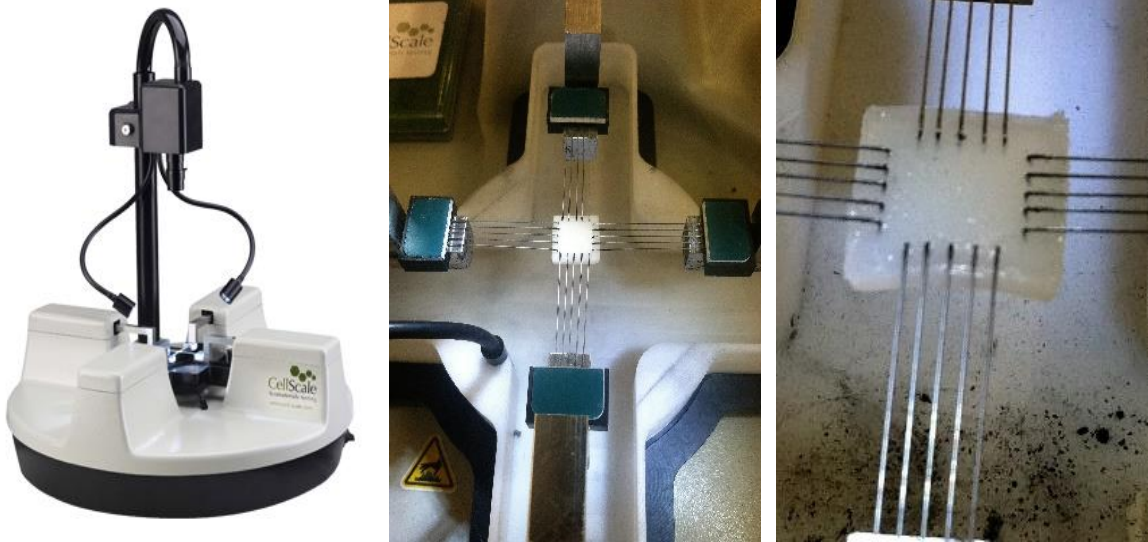


**Figure 42. Biaxial stretching system; molded sample of crosslinked hydrogel; close-up of cuboid test sample attached to prongs for biaxial testing.**

## 3-D Bioprinting

The BioBots 3-D bioprinter (BioBots, PA) including 365nm UV light with unfiltered air compressor (California Air Tools, CA), 10 ml syringes (BD Laboratories, ), 0.100mm nozzles

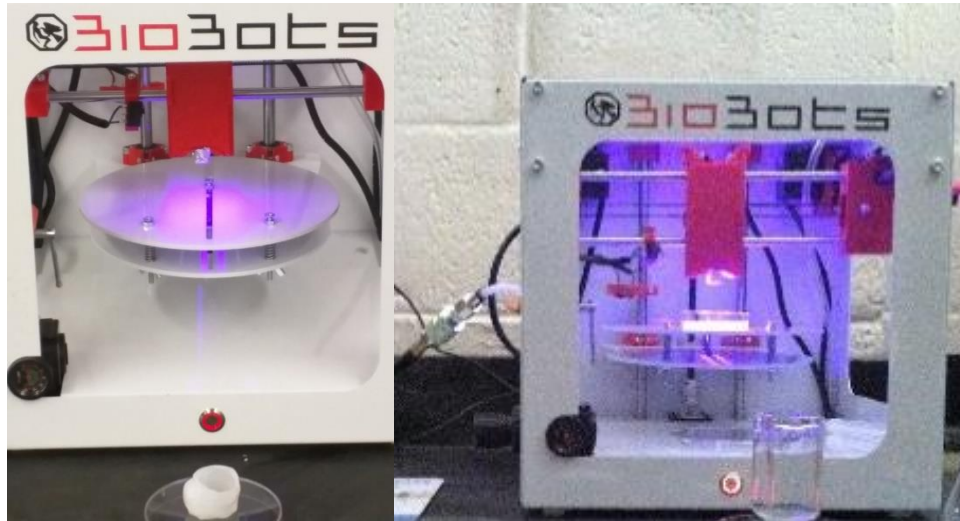


**Figure 43. BioBots beta version 3-D bioprinter.**

(Jensen Global, loc.), polystyrene Petri dishes(Sigma-Aldrich) and SI3cer software (open source) were used to control deposition and crosslinking.

The g-code is largely dependent on the number of layers desired within the wall, that is layer width. This layer width drives nozzle diameter selection. In light of the hydrogel flow properties and the Barus effect, the width of the printed filament is related to the nozzle diameter, print speed and flow rate.

The procedure for setting the print settings involves a compilation of experimental testing, CFD, and analytical results. Experimental flow rate test and protocol patterns are used to obtain extrusion data, then the CFD is used to calculate the pressure setting for a desired flow rate, and finally analytical figures are shown to illustrate the numerical configuration.

Flow rate is selected in coordination with print speed setting, determined by cross-sectional area of nozzle and deposited filament. Relative velocities of flow and print nozzle change deposition cross-sectional area. The flow rate from the nozzle equals the print speed multiplied by the printed cross-sectional area.

$$\text{Flow Rate} = V_{\text{nozzle}}A_{\text{nozzle}} = V_{\text{print}}A_{\text{deposit}} \quad (4.9)$$

$$Q = V_{\text{print}} \times \text{Area}_{\text{cross section of printed filament}} \quad (4.10)$$

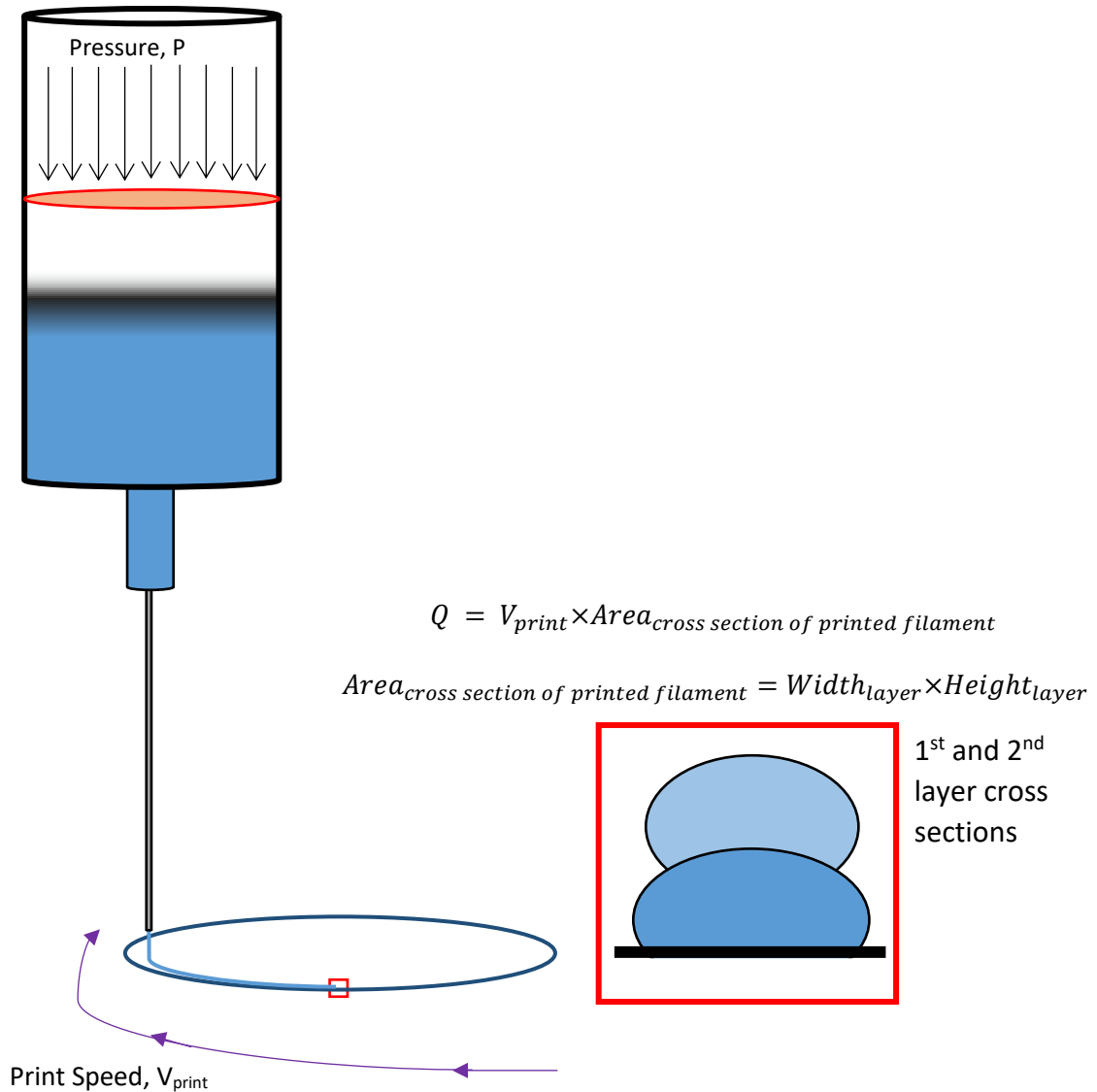


**Figure 44. First and second layers matching flow rate of hydrogel to the print velocity and the print cross-sectional area. A slight difference always exists between the first layer profile and the rest of the layers.**

The figure above illustrates the continuity of the extrusion system as it contacts the print bed and builds up layers. The relationship between relative cross-sectional areas of the nozzle and printed filament is the ratio of average flow velocity and the print speed. Also the relationship between flow rate and cross-section area of the printed filament equals the print



speed. These relationships empower good print configuration and correct tuning of subtle factors as print quality reaches its optimum.

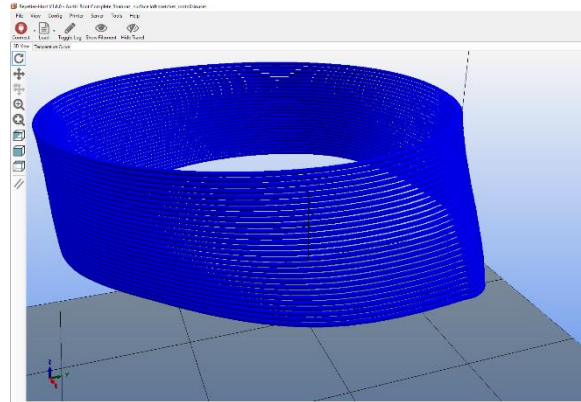


**Figure 45.** The g-code designs the pattern of motion for each layer.

Once the desired flow rate is determined from the patient-specific geometry of the pattern, the number layers laterally and vertically are chosen, and the nozzle size is selected accordingly, then the pressure setting is found using the CFD simulation as a guide for the pressure and flow rate relationship seen in the results. With the proper configuration and the polymerization reaction in sync with the timing of the printing process, the scaffold is fabricated and then put in PBS bath at room temperature for 24 hours to diffuse the ionic byproducts of the photoinitiated polymerization out of the scaffold.

Print quality was evaluated based on the wall thickness and dimensional fidelity. Many nozzle sizes and print settings were tested with the same geometries, and widely different geometries were printed with the same setup. Iterating this way allow for extensive beta testing and further the specific goal of printing an ascending aortic scaffold.

## CHAPTER 5: RESULTS

### Hydrogels

Mixing procedure is critical for efficiently solubilizing the components of the hydrogels. Temperature is useful for solubilizing LAP and gelatin, but does not significantly affect the solubility of HPMC. The ambient pressure, gaseous composition, and % humidity all affect the mixing process. Surface tension and micelle formation affect the homogenation of hydroxypropyl methyl cellulose in particular, which calls for slow addition of the powder to the solvent. Typically, the mixing process generates air bubbles within the gel. The centrifuge degassed the hydrogels once loaded into the syringes, proving to accomplish the secondary task of loading the syringes with gas-free hydrogel. Premature crosslinking was never noticed as a problem. Controlling the temperature is important to the hydrogel's viscosity so care was given to allow all hydrogels sufficient time to equilibrate.

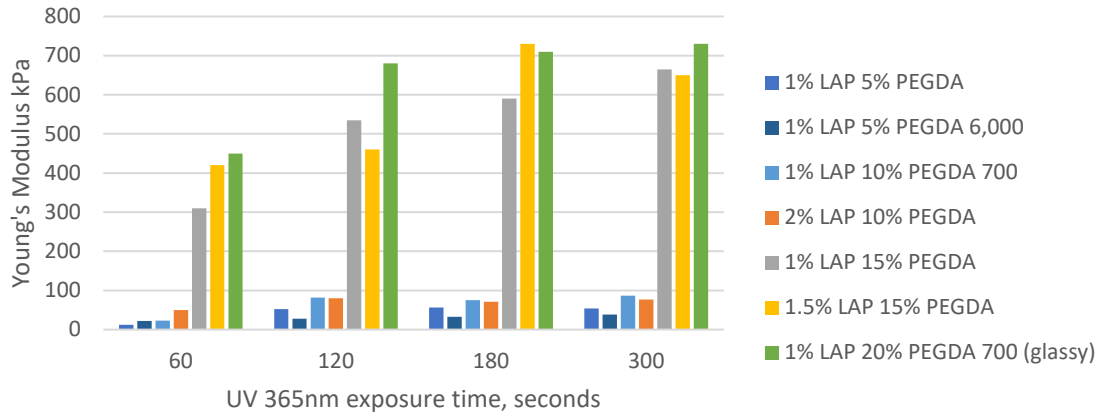
The composition of the hydrogels with regard to photoinitiator concentration was tested for performance in the earliest pilot study. The results are shown in the figure and validated the amount of LAP to be added, given the monomer concentration in the hydrogel. The effect of time of the UV light exposure with regard to resulting polymer's mechanical properties was examined and shows a plateau after 5 minutes, although mechanical properties appear to increase at a decreasing rate, given that 3 minutes of exposure achieve nearly the

same Young's modulus (74 kPa vs. 81 kPa) and at 90 seconds the Young's modulus is already 66 kPa.

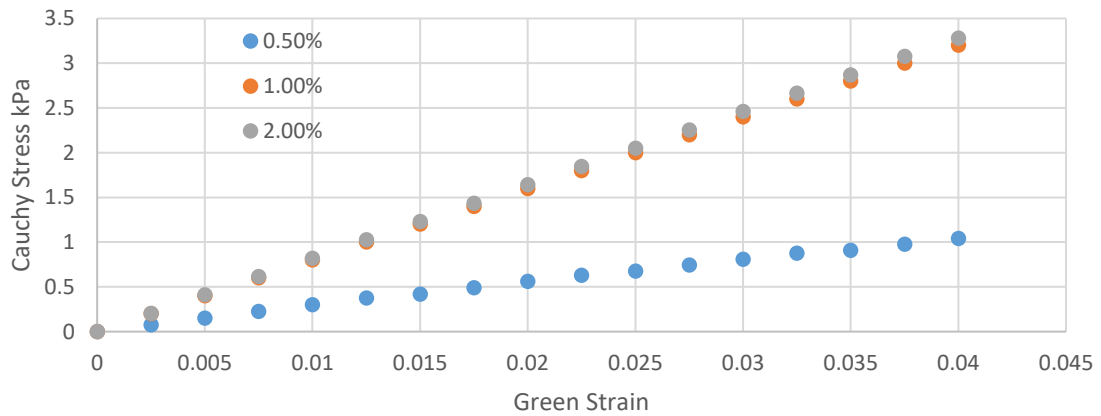
With the photoinitiator concentration relative to polymer concentration determined the variables are reduced and the copolymer choice was made based on its high viscosity. Mixing HPMC into the PEGDA solution significantly raises the viscosity and makes the hydrogel appropriate for controlled extrusion with enough force to crosslink into an undistorted construct. Balancing the polymerization and the viscosity is a critical aspect defining superior hydrogel for this application. As well, the mechanical properties are diminished by the addition of HPMC as a viscous agent further complicating the balance of relevant factors. In this work, 2% HPMC bestows sufficient viscosity and does not dramatically affect the surface tension like some other viscous agents.

Three important grafts from early testing are shown on the next page to support the % composition of photoinitiator in the hydrogel. Anseth et al. from UC Boulder have demonstrated the kinetics and conditions of the LAP photoinitiation reaction, which supports the results that 1% LAP concentration to polymer concentration is sufficient. Her research also supports the crosslinking time of  $\sim 300$  seconds, given a scaffold thickness of less than 1 cm<sup>73</sup>.

### Basic poly(ethylene glycol) diacrylate properties in relation to photoinitiator and UV time



### PEGDA 10% - effect of LAP concentration with 300 seconds UV (365 W/cm<sup>2</sup>) exposure, @25C



### Effect of UV exposure time on mechanical properties of 10% w/v PEGDA in PBS

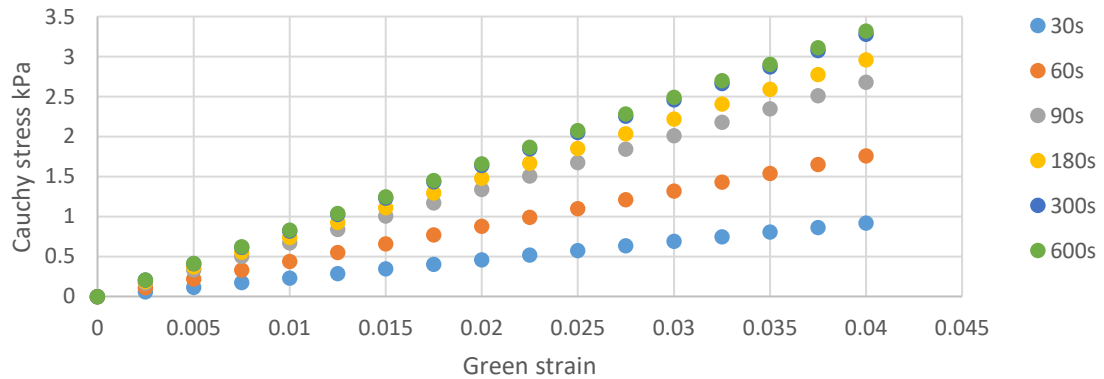


Figure 46. Effects of LP concentration and UV light exposure time, 365 nm and 410 mW/cm<sup>2</sup>.

## Viscometry

The best copolymer solution shows shear thinning behavior (Figure #). Fitting to a Power Law curve the coefficients are  $k = 5.5$  and  $n = 0.52$  (equation 4.2). If the slope of the curve is estimated at a shear rate of 500/s the apparent viscosity would be 294 cP. After fitting the curve, the coefficients and experimental data are used to set up the CFD simulation parameters.

The relationship between viscosity and temperature has many implications. As seen in figure #, the viscosity decreases from 25°C to 37°C. This is because of intermolecular space increases as fluid temperature increases and molecular kinetic energy increases. This provides analytical insight to understand viscous losses. Additionally, relating the temperature and viscosity of a hydrogel, along with printing control of temperature, can provide an effective means to tune the viscosity to a desired level. It is important to consider the possible effects of viscous heating, which has been shown to have effect in microchannel flows <sup>221</sup>.

Along with the observations from the previous section on polymers it becomes apparent that viscosity is dependent of several factors including: temperature, shear rate, molecular weight distribution and molecular shape. Temperature and shear rate are well established in the literature (equations 4.2 and 4.3). Paul Flory introduced both of the concepts used today to relate the molecular weight and the atomic interactions, due to molecular shape and polarity, in a fluid flow to the viscous behavior of the fluid flow. These observations appear relevant when designing a viscous hydrogel.

Ultimately for our purpose, the viscosity data was considered only in the context of shear rate and temperature since these were variable factors once the hydrogels were prepared. It remains true that viscosity range available to any hydrogel was positively correlated

## Printable Hydrogel

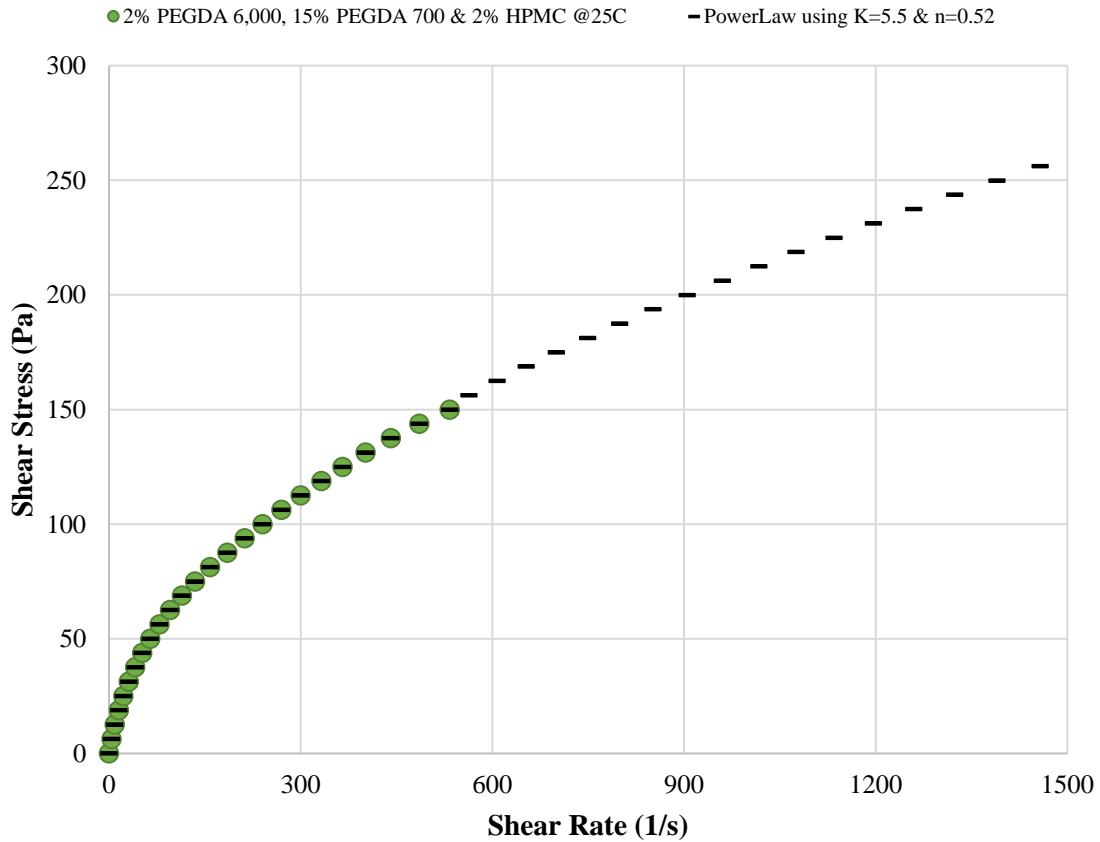


**Figure 47. The best hydrogel has shear thinning behavior as shown. A curve is well fit to the viscometry data using the formula shown for Power Law fluids.**

with the average molecular weight of the composition of the gel. The polarity and ring shape of cellulose contributes to its extraordinary viscosity at 2% w/v concentrations. The viscometer allowed quantification of these behaviors, greatly simplifying the matter, and guided CFD simulation parameters as well as provided a basis for curve fitting the non-Newtonian behavior of hydrogels.

Specifically, the viscosity of PEGDA goes from 5 cP to 12 cP as the concentration increase from 5-20% w/v. The photoinitiator does not affect the viscosity at the relatively low concentrations used. With the addition of 2% w/v HPMC the viscosity is increased substantially

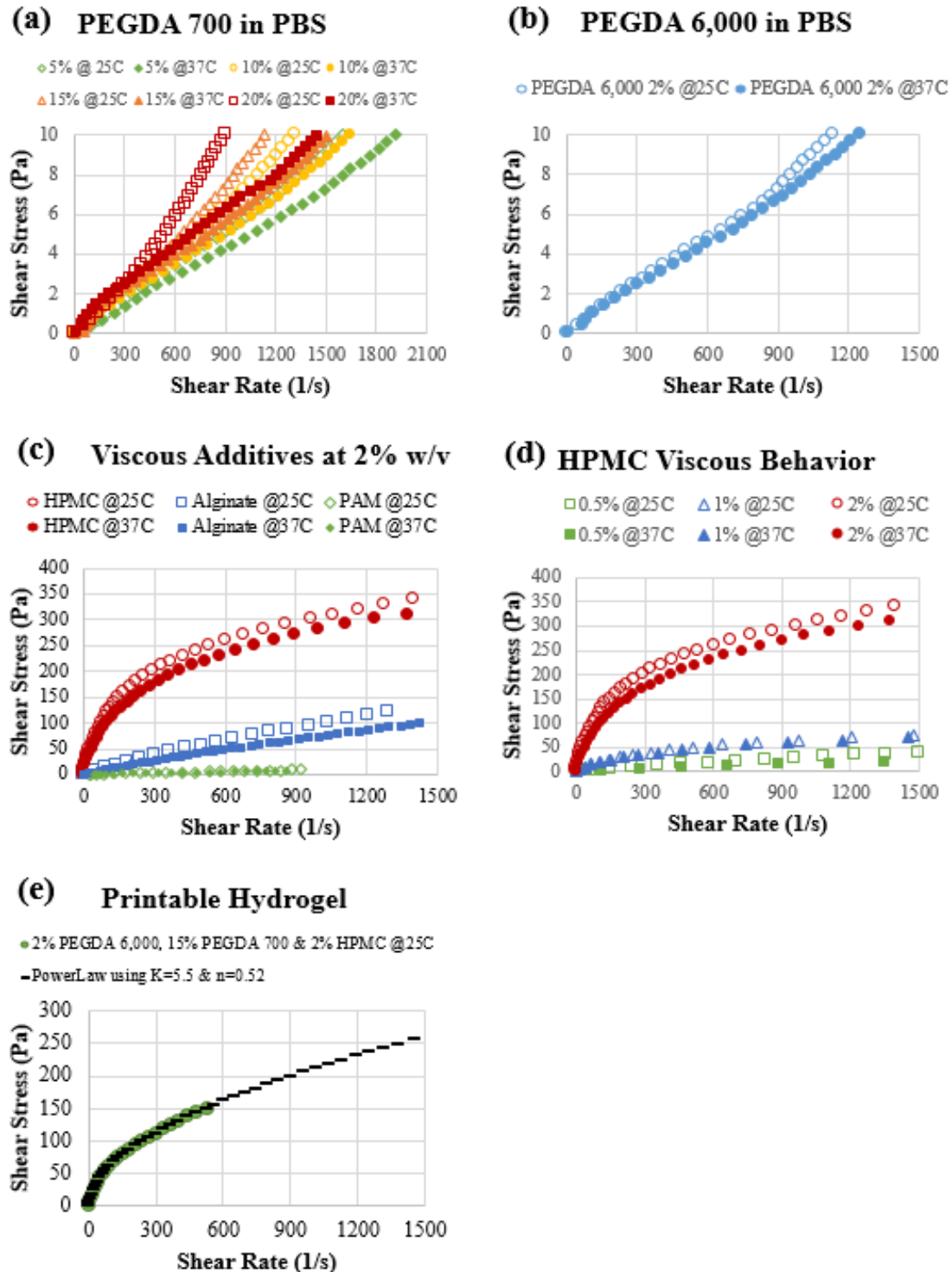
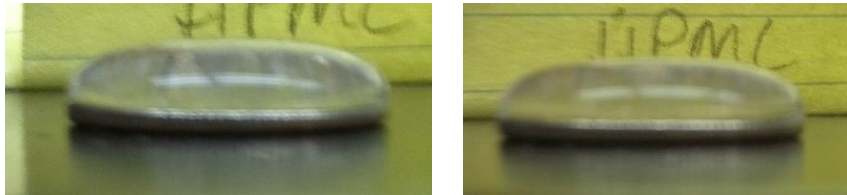


Figure 48. The best hydrogel in context of its component molecules and their viscosities.

shear rate increases from 10-600 1/s. Among several viscous agents tested, HPMC provides the best qualities for viscous properties and print fidelity.

## Surface Tension

The interfacial tension affects the deposition of the hydrogel onto the printing platform. It also affects the interaction between the hydrogel and the nozzle wall, which was not measured directly. The stress at the wall is calculated on the reasonable assumption of no-slip between the wall and the hydrogel. The friction factor and head loss show the aggregate effect of shear stress within the extrusion geometry. The low Reynolds number provides a dimensionless figure showing that the viscosity is more important than the inertia for our print system. The tension created in the surface when the hydrogel leaves the nozzle and is exposed to the air can have effects on the flow properties, which is conveyed by the capillary number. The Euler number shows the pressure energy far exceeds the kinetic energy for the system.



**Figure 49. The surface tension of a 2% w/v HPMC hydrogel on a dime for illustration of the interfacial forces in room air and temperature.**

**Table 11. Surface tension of various fluids and hydrogels at room temperature 25C.**

Polymer with PBS	Apparent Viscosity (cP)	Surface Tension (mN/m)	Young's Modulus (kPa)
Deionized water	1	72	NA
Dei water w/ PBS	1	62	NA
PEGDA 700 10%	3	56	440
PEGDA 700 15%	7	54	640
PEGDA 700 20%	11	51	775
Gelatin 5%	500	63	350
Cellulose 2%	1200	47	250
Alginate 4%	750	52	400
Polyacrylamide 4%	650	48	200
5% G & 10% P700	600	59	1000
2% C & 15% P700	1400	49	750



**Table 12. Calculation of viscous and inertial forces for the best hydrogel when extruded from 0.21mm nozzle at 10 psi.**

Wall Shear Stress (Pa):	367.50	Shear Stress (Pa):	367.5
0.000105 nozzle radius (m)		0.000105 nozzle radius (m)	
70,000 pressure gradient (Pa)		0.0193 U avg (m/s)	
0.01 length (m)		0.5 hydrogel viscosity (Pa.s)	
Friction Factor(no unit):	7,051.74	Head Loss (Pa/rho):	62.50
0.0002 nozzle diameter (m)		0.0002 nozzle diameter (m)	
0.0193 U avg (m/s)		0.0193 U avg (m/s)	
0.5 hydrogel viscosity (Pa.s)		0.01 length (m)	
1120 hydrogel density (kg/m <sup>3</sup> )			

**Table 13. Calculation of dimensionless parameters for the best hydrogel when extruded from 0.21mm nozzle at 10psi.**

Reynolds Number	0.018152
1120 hydrogel density (kg/m <sup>3</sup> )	
0.0193 U avg (m/s)	
0.00021 nozzle diameter (m)	
0.5 hydrogel viscosity (Pa.s)	
Capillary Number	0.196875
0.5 hydrogel viscosity (Pa.s)	
0.0193 U avg (m/s)	
0.049 surface tension (N/m)	
Euler Number	1.68E+05
70,000 pressure gradient (Pa)	
1120 hydrogel density (kg/m <sup>3</sup> )	
0.0193 U avg (m/s)	

The wall shear stress is not significant when compared with the total shear stress within the flow. This alludes to the fact that the no slip condition at the wall may not be as important as the shear stress within the bulk of the hydrogel. The friction factor is unremarkable but leads to the head loss value that shows there is significant consumption of pressure energy by viscous forces within the bulk of the fluid, which has a density of 1,120 kg/m<sup>3</sup>.

The dimensionless parameters for the flow regime show the relative importance of viscosity, surface tension, inertia, and geometry. The Reynolds number shows that the flow has

insignificant inertia compared with viscous forces. The capillary number shows that the surface tension is relatively important when compared with the viscosity of the extrusion. The Euler number shows that force of the pressure gradient, in terms of cross sectional area, is far greater than the kinetic energy of the fluid flow. For a perfectly frictionless flow the Euler number will be 0, so there is a significant imbalance and a great consumption of energy in the small nozzle extrusion system.

## Computational Fluid Dynamics

The laboratory experimental test showed good validation of Newtonian hydrogels, +/- 5%, but +/- 10% matching with shear thinning hydrogels where experimental shear thinning behavior may deviate from basic simulation settings. The behavior of non-Newtonian fluids is challenging to characterize in microchannels and it is necessary to configure the CFD carefully for the boundary conditions and viscous parameters when simulating non-Newtonian microchannel flows.

Using the simulation to obtain total pressure loss from desired flow rate, the plot of flow rate and pressure can be used to approximate the experimental data with 10% error.

The pressure gradient through the syringe is of particular interest because it shows the head loss along each section of the syringe. The figure below gives the contours of pressure, while the second figure shows the contours for only 99% of the total pressure at the inlet.

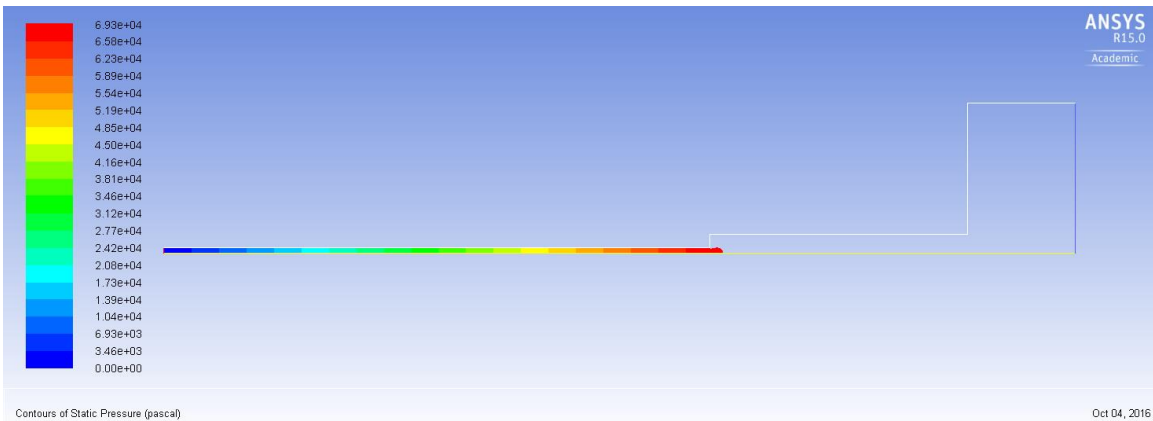
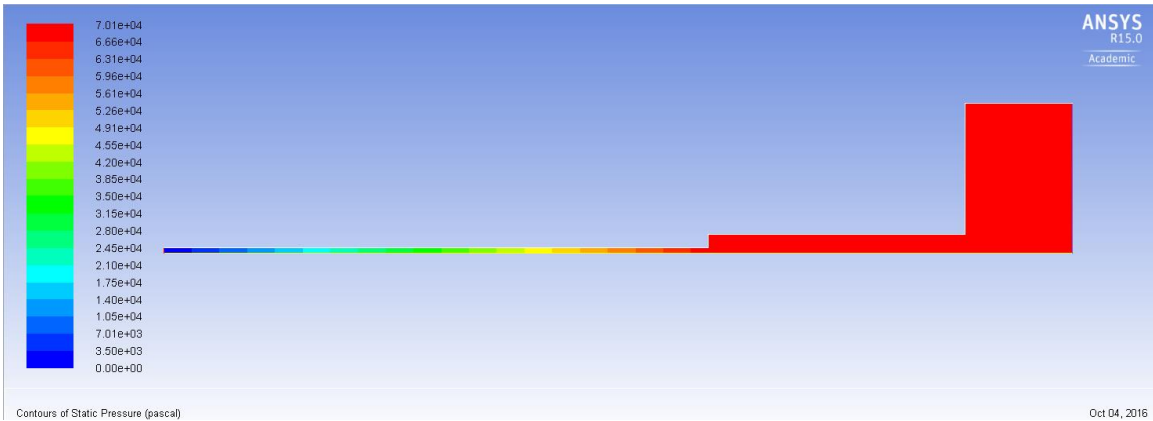


**Figure 50. 99% of pressure drop. Most of the pressure is lost due to the length of the nozzle and not the syringe. Top shows the contours for 100 % of the  $\Delta P$  while the bottom shows 99% of the  $\Delta P$ , that 70,000 Pa and 69,300 Pa respectively.**

These figures show that 99% of the pressure drop from inlet to outlet occurs within the nozzle. To illustrate the point further, it is useful to look at the alternate geometries. In each of these geometries, except the cone shaped geometry, it is also observed that the head loss in the nozzle is the main determinate of total head loss regardless of tapered edges or more streamlined geometries. The pathlines are of particular interest for the various geometries because they depict the effects of the flow boundaries. First the ordinary geometry is shown focused on the constriction into the nozzle, which shows the curvature of the path taken by flow near the wall and the acceleration of particles into the nozzle. Second the altered geometries are shown to illustrate the similarity of the flow pathlines regardless of the wall taper. This is

interesting because the corner appears to create a zone with high residence times, which not changed significantly by changing the angle in the corner of the walls. In common sense this is because the headloss is occurring in the nozzle so the amount and pattern of flow into the nozzle should not change significantly due to changes which do not affect the nozzle dimensions.

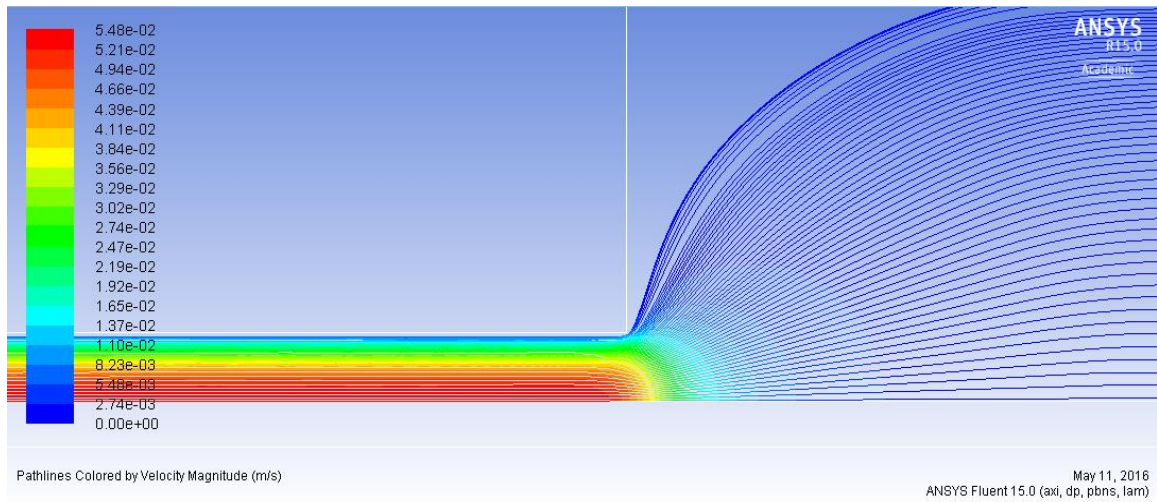


**Figure 51. Pathlines colored by velocity magnitude, notice that velocity is very low before the nozzle.**

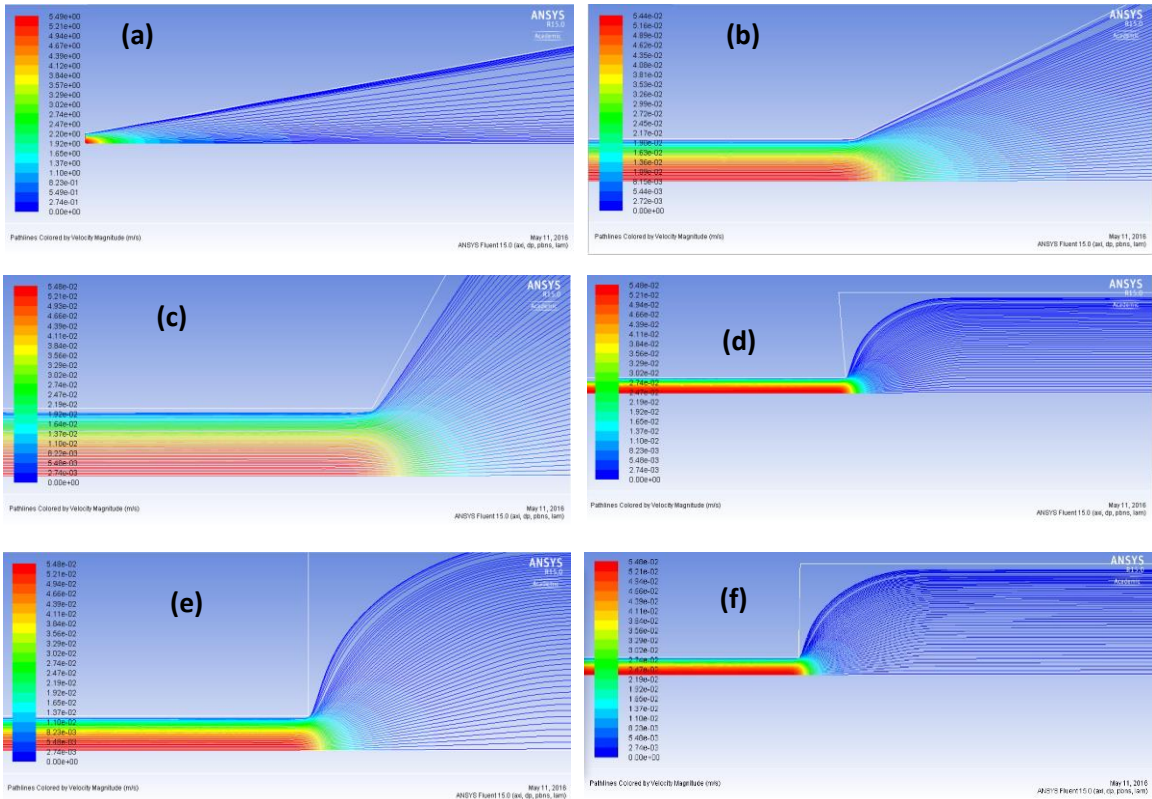


**Figure 52.** The different geometries tested and the pathlines colored by velocity magnitude, same scale for b-f. Notice the similar flow speeds under each design and the preservation of the no-flow corner between the walls.

**Table 14.** Comparing the different syringe geometries. 0.508mm diameter nozzle 70,000 Pa inlet gauge pressure, 0 outlet gauge pressure, viscosity of 100 cP.

Symbol		<u>Q ml/hr</u>	<u>dP/dz @ nozzle inlet (Pa/mm)</u>	<u>P @ 25.4mm</u>	<u>Vmax mm/s</u>	<u>Vavg mm/s</u>
A	cone	404.79984	1	139994.0	5488.950	3012.6
B	cone & neck	3.68165	3370	139471.8	54.324	27.4
C	120	3.68465	3041	139643.2	54.360	27.4
D	85	3.68524	3009	139677.1	54.379	27.4
E	90	3.68518	3008	139965.2	54.378	27.4
F	91	3.68508	3009	139661.7	54.377	27.4

Notably any perturbations to the outer corner between the syringe and the neck have no effect on flow rate to 3 significant figures. This is emphasized by the results for the corner adjacent to the nozzle, where the flow rate appears basically dependent only on the dimensions

of the nozzle alone. This result shows that the geometry of our syringe is inconsequential, due to the dramatic head loss in the nozzle of the extrusion system.

Looking back at the fundamental geometry, the wall shear stress within the syringe and nozzle are of interest. This gives the location of the maximum stress value, which can be useful if there is a stress range that must not be exceeded.

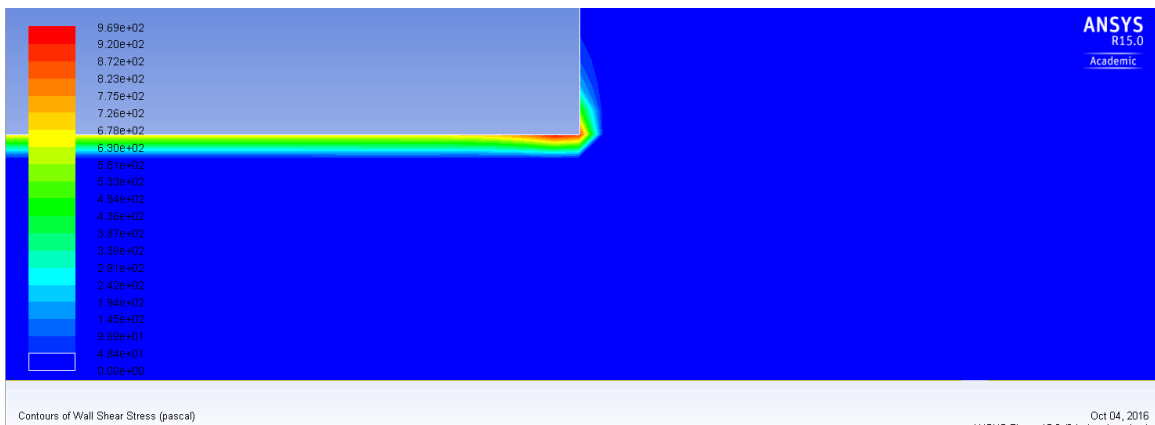


**Figure 53. The wall shear stress maximum which occurs at the entrance length of the nozzle.**

The simulation also sheds light on the shear rate within the extrusion system. This is particularly relevant if cells were combined into the hydrogel but is also relevant because a correlation may exist between the scaffold mechanical properties and excessive shear rates on large polymer chains.

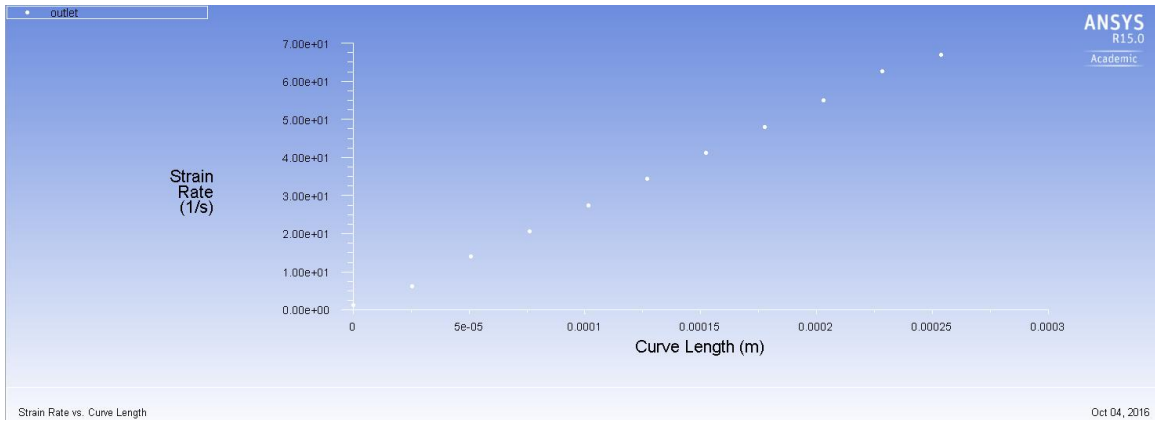


**Figure 54.** The strain rate across the outlet is interesting because it linearly increases from the center to the wall for Newtonian fluids.

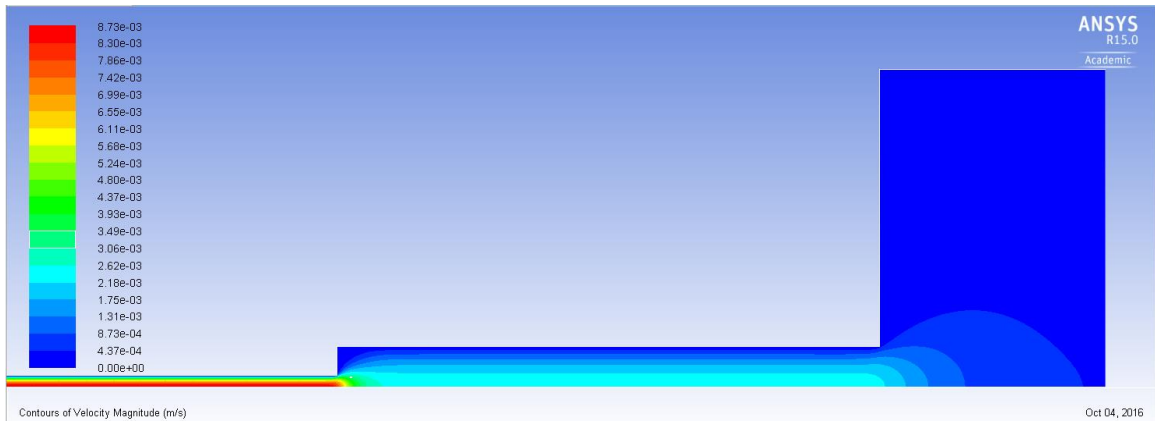


**Figure 55.** The velocity contours, maximum velocity shown in red is 8.73 mm/s.



**Figure 56.** The pathlines colored by velocity magnitude.

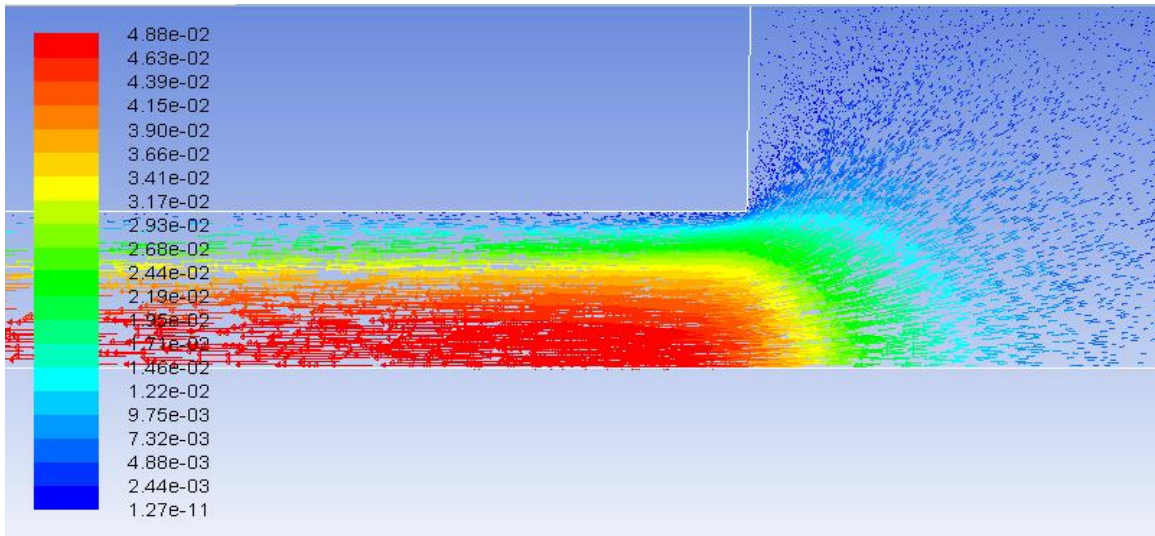


**Figure 57. The velocity vectors as the hydrogel accelerates into the nozzle and reaches a fully developed state after 78 microns.**

The main goal of the CFD was to ascertain the pressure and flow rate relationship.

Experimental tests, Newtonian simulations and non-Newtonian Power Law simulations were run and compared. The figure below summarizes the initial results of three experimental tests, two CFD simulations and the analytical work of Hagen and Poiseuille.

$$Q = \frac{\pi dP}{\mu L} \frac{D^4}{128}$$

Hagen-Poiseuille

$$Head Loss = \int_0^R \mu \frac{dv}{dr} 2\pi rL$$

Summation of layers of shear friction



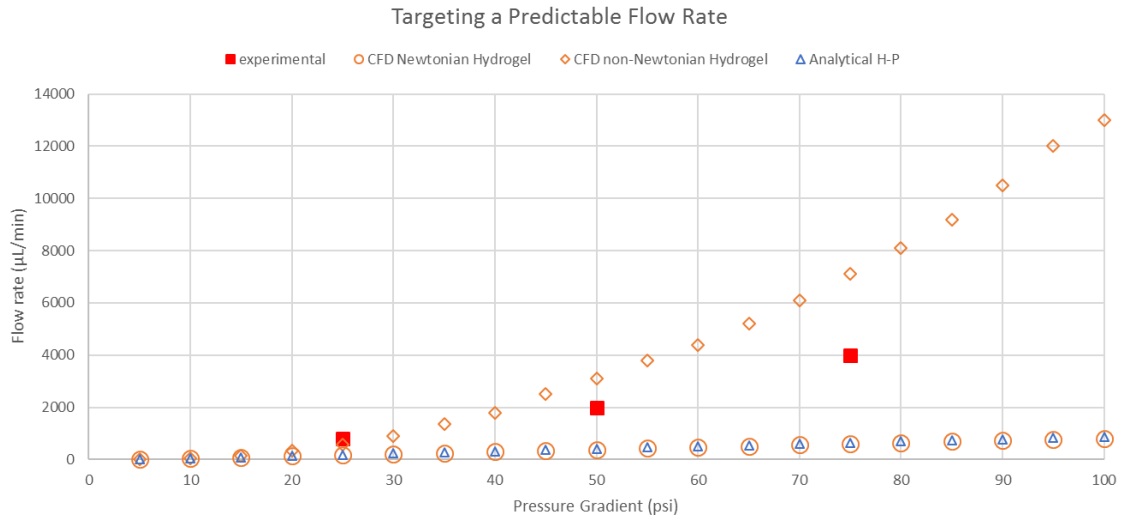


**Figure 58. The preliminary Q vs P graph showing experimental, CFD and analytical results.**

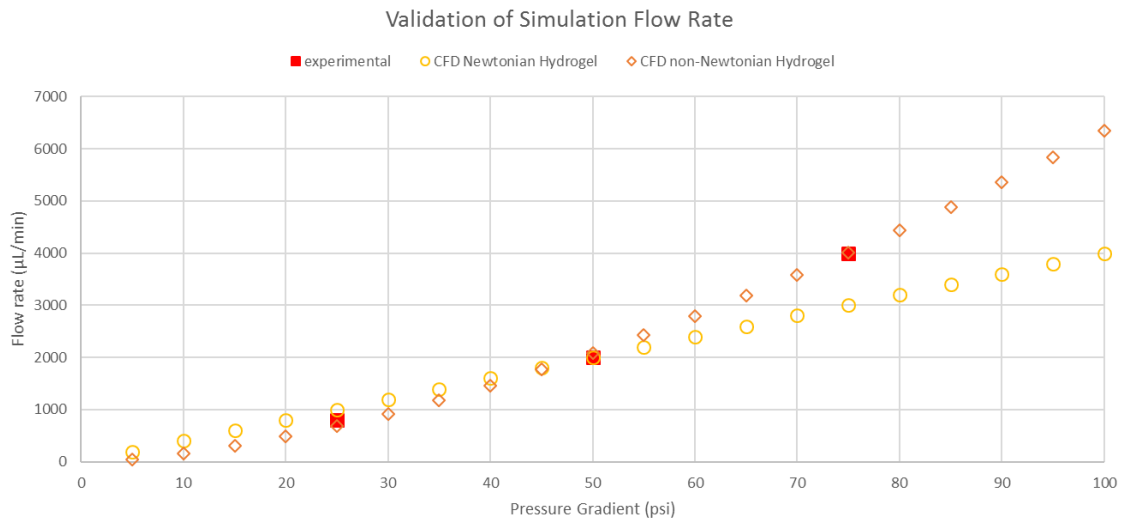


**Figure 59. The post processing graph show the simulation results after adjusting the viscosity to match the CFD simulation to the experimental P and to the experimental Q.**

The curve pictured above allows the user to select the correct pressure for whatever flow rate is desired. Additionally, if nozzle size is changed the parameters for viscosity will remain valid and become useful in swiftly ascertaining the pressure-flow rate curve for the new extrusion geometry.

**Table 15. The viscosity data from the viscometer is close to the expected value from solving the Hagen-Poiseuille equation with experimental results for viscosity, but the error shows the shear thinning behavior.**

Model	Viscosity (cP)
Viscometer	525
Hagen- Poiseuille	509

The lubricating properties of PEG based hydrogels are interesting and behave similarly to oil between the fingers as it remains slippery in very thin layers. This slip property alludes to the shear thinning property and reinforces the divergence from the Newtonian solution defined by Hagen and Poiseuille. Once the difference is established it is additionally observed that the analytical answer diverges by a greater percentage as flow rate increases, suggesting the exponential relationship.

**Table 16. CFD simulation results show effects of nozzle radius with Power Law fluid behavior.**

Nozzle Diameter (mm)	K	n	Apparent cP	Peak shear (1/s)	dP (Pa)	Q (ml/min)	V avg (mm/s) Nozzle outlet	Area mm <sup>2</sup>
0.08	4.7	-0.45	75	2967	66784	0.01	166	0.005
0.10	4.7	-0.45	90	2332	48868	0.01	117	0.0078
0.16	4.7	-0.45	94	1679	38661	0.01	40	0.020
0.21	4.7	-0.45	100	896	29468	0.01	62	0.0346
0.508	4.7	-0.45	246	70	6984	0.01	10	0.202

The tabular data above shows the influence of geometry on a single hydrogel, which is flowing at the same rate in each scenario for comparative benefits. As the nozzle radius decreases the shear rates within the flow pattern increase and further express the shear thinning behavior of the hydrogels.

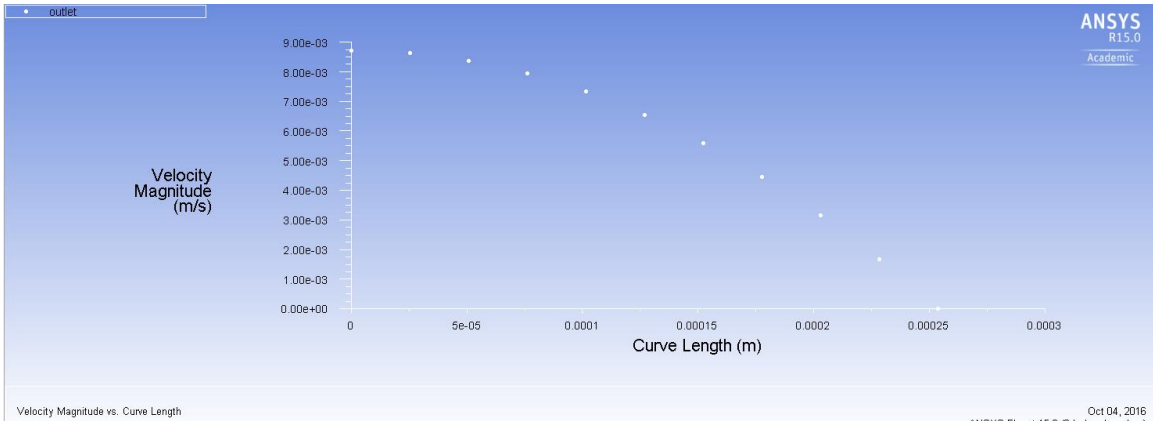


**Figure 60. The outlet velocity profile is parabolic and follows H-P as long as the viscosity is constant.**

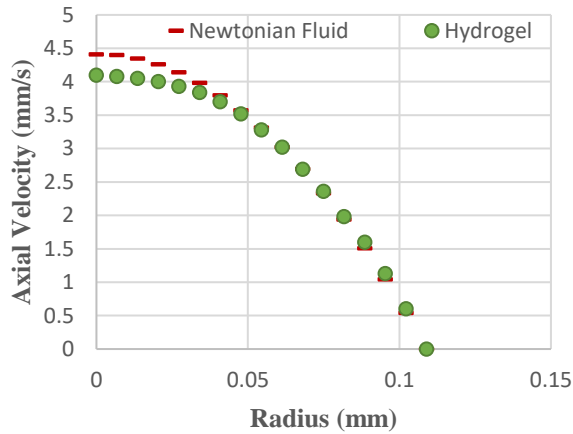


**Figure 61. The comparison of a Newtonian simulation and the Power law simulation with  $k=4$  and  $n=0.52$ .**

The results of CFD give an understanding of what causes the pressure gradient: geometry and viscosity. While wall interaction should be considered, the stainless steel nozzle is likely to have an unremarkable interaction with the hydrogel. The viscosity and the geometry are paramount components applicable to all extrusion devices. Understanding these gets us to understanding the P vs. Q relationship for each geometry.

The method is designed to answer the question  $dP = \text{coefficient } (\beta) \times Q$ , what is the coefficient once the hydrogel and the geometry are known. The answer is a scalar for Newtonian fluids but requires an exponential relationship for shear thinning fluids like most

hydrogels. If the viscosity of the hydrogel is 500 cP and the nozzle is 0.21mm I.D. and 1cm in length the coefficient  $\beta$  will be 2.61, which matches experimental values for 25, 50 and 75 psi. When the hydrogel is non-Newtonian the viscosity is defined by the Power Law (equation 4.2). Extrapolating to the extrusion relationship (equation 5.1) and solving for the two coefficients by fitting a curve to experimental results, the value for K is 0.08 and n is 1.34 ( P = Pa, Q = ml/s). These results are fundamentally simple and allow for fast reconfiguration for new prints.

$$P_{printer\ setting} = \beta \times Q_{extrusion\ geometry} \quad \text{Newtonian}$$

For Newtonian fluids this is a simple constant  $\beta$  parameter that applies to the specific geometry and the specific hydrogel. For shear thinning fluids there is a decrease in head loss per ml of flow volume as flow rate increases, so the flow rate increases exponentially with respect to pressure. The exponent n is dependent on the curvature of the non-Newtonian behavior of the hydrogel.

$$P_{printer\ setting} = K_{hydrogel\ viscosity\ coefficient} \times Q_{extrusion\ geometry}^n \quad \text{non-Newtonian}$$

## Patient Specific Geometry

Matching the design geometry is best at the bottom layers and losses fidelity as the geometry moves upwards. This is due to any undulations that are exacerbated each layer, any flow changes, any movement speed changes and z-wobble. The ultimate print quality is

evaluated in two ways, wall thickness and dimensional fidelity. Typically, the wall thickness becomes excessively thick as the print proceeds.

Typically the dimensional fidelity is best into the first 100 layers, beyond which the movement of the print under the extrusion causes

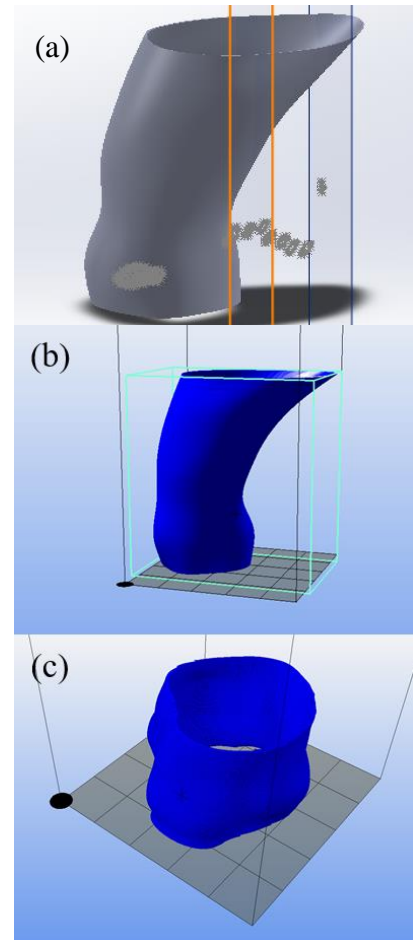
problems for print quality,

this is commonly referred to as z-wobble.

Patient specific geometry is a huge advantage over the standardized sizing and shapes for conventional Dacron grafts<sup>3</sup>. With nozzle based, pressure actuated extrusion it was possible to create overhanging features of constructs up

to 30° without support material, which is significant. The minimum thickness that was achieved was 0.3mm wall thickness, which is greater than the nozzle diameter. As nozzle sizes decrease this minimum width can be decrease but it does complicate the printer configurations to use smaller and smaller nozzles, so the cost can be substantial to decrease layer width.

**Figure 62. (a) Complete aortic root in Solidworks showing the boundary surface and omitted coronary arteries, (b) complete file imported for printing exceeds current print area, (c) patient specific geometry file for 3D printing software, truncated for print quality.**



## Biaxial Testing

Molds were used to create a standardized geometry and crosslinking condition for biaxial testing. Samples containing less than 5% PEGDA 700 without additives are difficult to test and handle due to lubricated surface characteristics and low Young's Modulus. Samples containing more than 20% PEGDA 700 without additive become remarkably hard and fracture at low strains below 1% Green Strain.

Mechanical Properties are weak because PEGDDA 700 is not long enough to give significant elasticity to the material. The longer molecules are more elastic and have higher fracture strains. The fracture stress of the materials is improved by increasing polymer concentration.

Mechanical testing results show that LAP concentration needs to be approximately 1% given our range of crosslinking times. We see a predictable increase in fracture stress as we increase PEGDA 700 concentration, and this is accompanied by a decrease in fracture strain. The viscous agent HPMC creates an interpenetrating polymer network (IPN) with the PEGDA 700 matrix and we see that it does not improve the mechanical properties of the sample, however the improvement to viscosity and surface tension is compelling. The ultimate mechanical properties of the best hydrogel is still weak but noteworthy characteristics of the hydrogel and its printability make it a step in the right direction.

How the molecules are organized may affect the mechanical properties due to entanglements and order/randomization. The amount of water in the samples matters, bonded vs unbonded water.

The fracture strain of certain materials. The Young's Modulus for various materials after different crosslink time. The Young's Modulus for various materials after different post printing time. The Young's Modulus for various materials for different mixtures of copolymers.

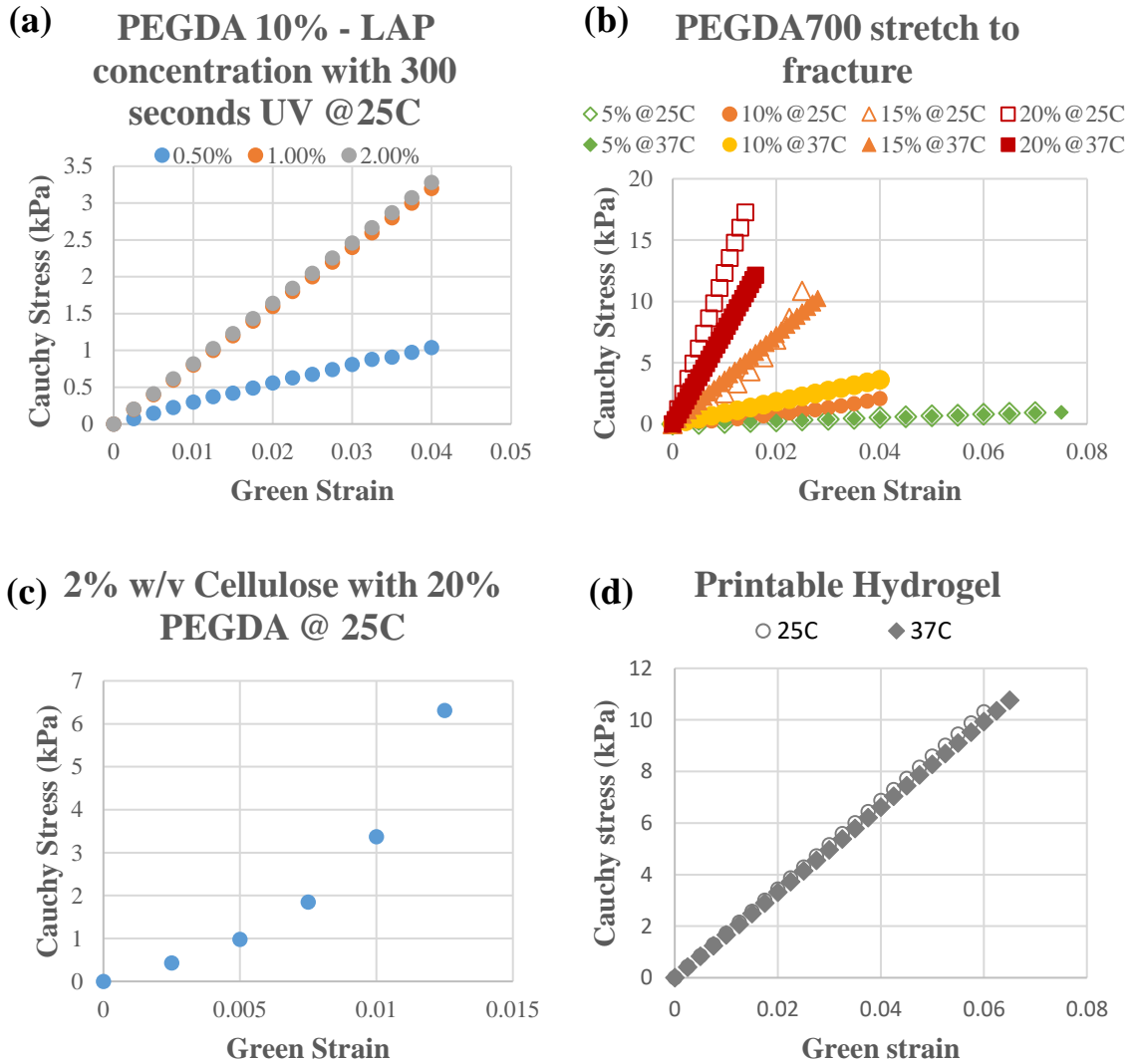


**Figure 63. Mechanical properties of scaffold materials, protocol had no preconditioning.**

From the mechanical properties it can be observed that as the concentration of PEGDA 700 is increased the Young's modulus increases. While an increase in temperature from 25°C to 37°C reduces the Young's modulus of pure PEGDA 700 constructs by up to 30%. The addition of HPMC changes the elasticity to a non-linear relationship between stress and strain. The effect of

temperature on HPMC copolymer construct mechanical properties is noticeably reduced as it was observed that constructs containing HPMC had more stable mechanical properties as temperature was varied. This may be due to the hydrogen bonding and ring structure of HPMC that conform to a very stable arrangement and reduce losses in Gibbs free energy as the temperature is increased.



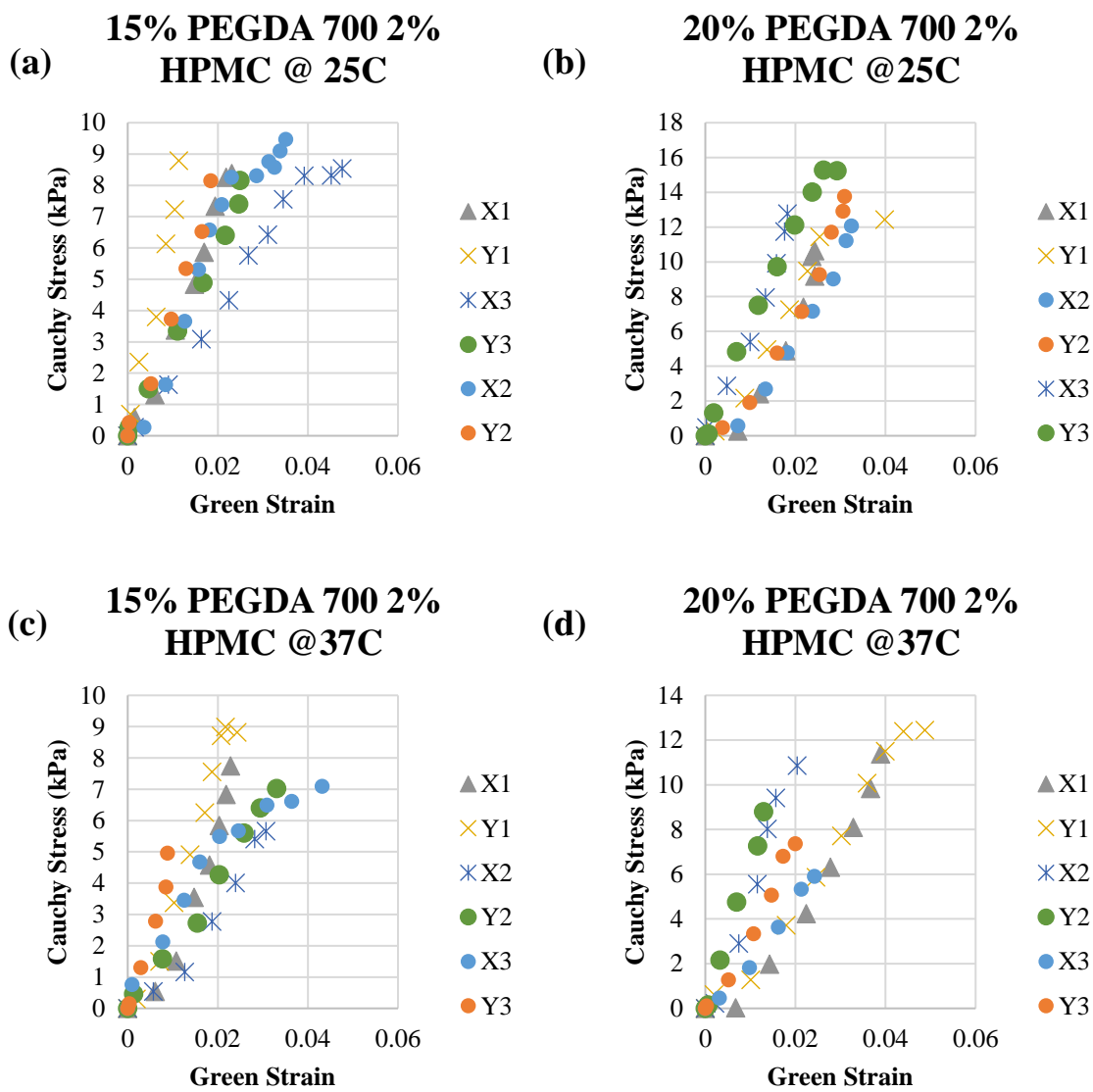
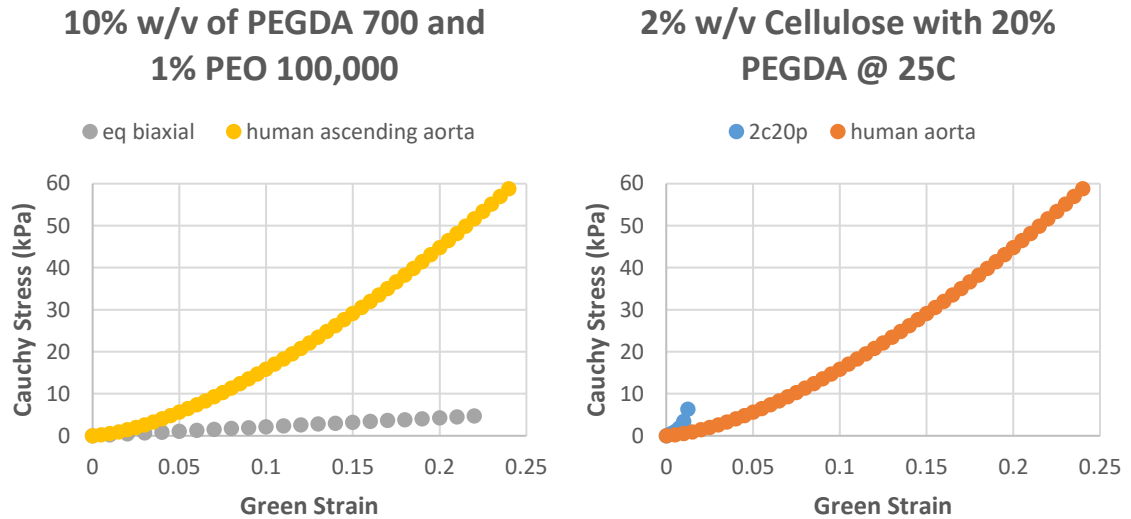


Figure 64. Raw data in x and y directions from the biaxial stretch test results (a) 15% PEGDA 700 2% HPMC w/v @ 25°C, (b) 20% PEGDA 700 2% HPMC w/v @ 25°C, (c) 15% PEGDA 700 2% HPMC w/v @ 37°C, (d) 20% PEGDA 700 2% HPMC w/v @ 37°C.

The raw data from mechanical testing shows the variation in the testing samples due to experimental error, small material differences in the composition within the molded samples, crosslinking differences from polymerization reaction proceeding at random and rapidly. The fracture strain for the samples are similar at 25°C and 37°C, which shows how HPMC minimizes the effect of temperature on the mechanical properties. In contrast, copolymer hydrogels with

gelatin are strongly affected by temperature and become stretchier and have larger fracture strains at higher temperatures.



**Figure 65. The properties of scaffolds after crosslinking compared with native tissue shows the relative disorganization of the scaffolding provisional matrix for cell seeding.**

The constructs have far lower fracture strains than native tissues. Using very high molecular weight PEO it is possible to achieve larger fracture strains but still well below native tissue. The ideal mechanical properties for scaffolds is not yet fully determined so this result shows two extremes of a stiff and a stretchy construct in order to demonstrate the variability of mechanical properties within this fabrication system using different molecular weights and crosslinking monomer units.

### 3-D Printing

Innovative 3-D bioprinting will likely print into a medium that is an equal density fluid field in order to optimize fidelity and control surface tension and oxygen and other gas exposure, which dramatically affects some polymerization reactions. Then temperature control

and pressurized filtered air and temp control on the bed as well. Combinations of methods with become the best option as research progresses. Mixtures of gels and copolymers that take the best qualities from separate materials and combine them in one material. Chemical, UV, and thermal crosslinking can each be used for specific fields in biomedical engineering, which photosensitive polymers deserve substantial attention. UV light filters and patterning, along with controlling the g-code offer flexible methods for tuning and exactly quality prints. Other 3-D techniques lack the benefits seen with the air pressure extrusion method.



**Figure 66. Aortic scaffold being printed under 365 nm UV light with intensity of 410 mW/cm<sup>2</sup>; finished scaffold from two angles, 15 % PEGDA 2% HPMC w/v.**



**Figure 67. Thin walled scaffold printed with thickness between 0.4mm-0.8mm, and dimensional fidelity is +/- 2% with several dramatically overhung features. Gelatin 5% -PEGDA 15% w/v copolymer.**

These prints show the different print geometries that can be designed with various bulbous overhanging features. The subtly different geometries show the ability of this method to fabricate patient specific geometries based on non-regular curves and geometric features that are extremely difficult to achieve with most conventional methods in short time frames. It also shows the different surface chemistry and surface

Earlier prints of aortic valves demonstrate the potential of this RP method to fabricate interesting shapes without support material. All of these constructs are based on the same geometry and this shows the progress over many different prints of the same object.



**Figure 68. Aortic valve scaffolds from separate prints of 2% HPMC and 10% PEGDA 700.**

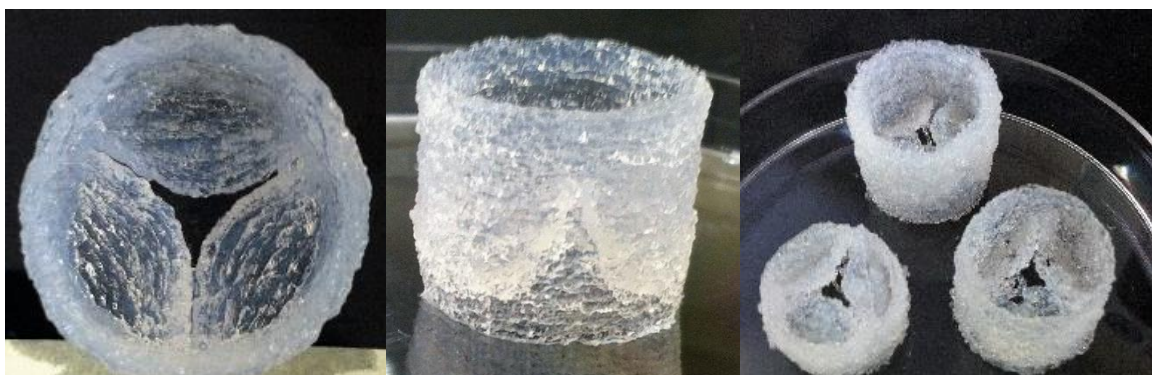


**Figure 69. Aortic valve scaffolds from separate prints of 5% gelatin and 10% PEGDA 700.**



**Figure 70. Aortic valve scaffolds from early testing with testing with alginate-PEGDA copolymer hydrogels.**

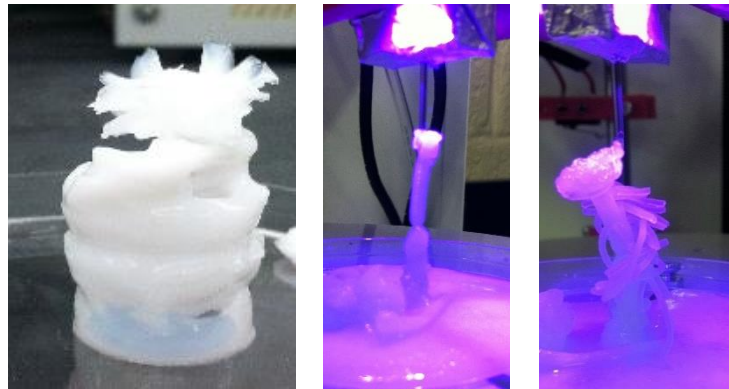


**Figure 71. There are real phenomena when the print settings are wrong.**



**Figure 72. The extrusion can be configured such that the material crosslinks before contacting the print bed and thus creates a long elastic thread.**

The print quality is highly dependent on configuration of the print settings. Errors compound as the print height increases making small miscalculations costly. The non-Newtonian behavior of the hydrogels makes small errors in pressure into larger errors in the flow rate; also

the non-Newtonian behavior is associated with the polymerization behavior, which accounts for print quality errors when polymerization occurs so quickly that the extruded material crosslinks before contacting the print bed. Each of the experimental errors helped to progress the main work of fabricating a high quality scaffold. Many of the errors demonstrate cool phenomena and in fact provide information about the cause and effect of print settings and print quality.

## CHAPTER 6: DISCUSSION

Overall, the true and simple purpose of this laboratory work is the precise extrusion, deposition and finally crosslinking of a hydrogel into a biocompatible scaffold. The realization of this requires a plot of the relationship between Q and P for a given hydrogel and a given nozzle geometry. Beyond the behavior of the fluid in the system, the relationship between extrusion flow rate and print dimensions are important because we must choose an ideal flow rate for each print setup. With this ideal flow rate in mind the CFD simulation provides the pressure setting. The previous testing can allow prediction of the mechanical properties before printing based on the mixture for the hydrogel.

The hydrogel contains the building pieces, molecularly speaking, for the matrix within the scaffold. This necessitates a perfect balance of sizing the molecular weight distribution to optimize viscous properties for extrusion and specifically incorporating cell adhesive and ubiquitously biocompatible molecules to create the optimal crosslinked matrix for cell adhesion, mechanotransduction, and diffusion. In this sense, the challenge is meeting both demands with a photoinitiated monomer solution with low viscosity. The PEGDA matrix has been shown to adhere cells<sup>7</sup>. The addition of a viscous molecule like HPMC proves to optimize the viscosity for use with the 3D BioBots printer. The result of this combination is an interpenetrating network of covalent and ionic bonded matrices<sup>7</sup>. There may be benefits and test with cells will show. The cell adhesion of HPMC is well established<sup>7</sup>.

The hydrogel properties are dependent on the molecules that comprise it. At the molecular level, the two main forces that influence fluid properties are physical chain interactions and polar interactions between oxygen moieties on the molecules. Flory et al established well regarded methods for communicating the properties and structure of polymers before and after crosslinking.

Bifunctional monomer means that the polymerization will lead to long flexible chains of PEGDA molecules linked at their ends. Random distribution of reaction sites, but the propensity is dramatically towards the double bonded carbon. The interpenetrating network.

Grafting RGD peptide and the control of cell adhesion shows promise in research from several groups<sup>124,222</sup>. This type of chemistry is becoming more common place and promises to create ideal TE scaffold molecules, which possess the correct viscous behavior, mechanical properties and cell attachment moieties.

The % of bonded and unbonded water is observed to understand the affinity for water molecules within the bulk material. The best constructs made have 83% water by weight and do not absorb any further water after crosslinking and 24hours in PBS solution. The water content affects the Young's modulus for a single test sample, where fully hydrated samples are easier to stretch. Hydrolysis is known to create more crosslinks in a polymeric material. The desired water content within the scaffold is determined by the polymers selected and their concentrations, which determine the amount of water that can be engage in hydrogel bonding at any one time.

It is clear that linear chains of PEGDA show less shear stress at any given shear rate, while gelatin represents a more branched still linear chain polymer molecule, which flows readily but with greater viscous dissipation, and finally cellulose, which contains two rings and



strong hydrogen bonding from oxygen molecules. The molecular volume of cellulose is more important to its viscosity than its molecular weight because in creep flow the steric hindrance and bulbous conformation of cellulose make it highly viscous until increasing shear rate brings greater streamlining within the boundary layers (shear thinning behavior). The molecular weight distribution has been suggested to be the appropriate guide for predicting viscosity; however, this neglects the important effects of molecular volume, steric hindrance, branching geometry, polarity and free space.

$$\mu = kM_v^a \quad (6.5)$$

The above equation represents the change of viscosity with the change molecular shape and volume. K is a constant showing the effect of molecular volume on viscosity, while  $a$  is a variable that shows the effect of random coils ( $a = 0.5$ ) and rod-like chains ( $a = 1$ ) on the viscosity<sup>223</sup>. From Malcolm Stevens Polymer chemistry. The increased viscosity of cellulose versus gelatin is likely due to the polarity of the oxygen molecules in cellulose and the intermolecular attractions.

The physical and mechanical properties of hydrogels usually reflect, to a degree, the weighted average of components. The rule of mixture suggests a basic weighted contribution, which neglect the interaction effects. A better model is to assume an interaction term exists.

$$P = P_1\phi_1 + P_2\phi_2 + I\phi_1\phi_2 \quad (6.6)$$

Here the rule of mixtures is used with a relevant addition of interaction effects. When I is negative the interaction destructive, when I is positive the interaction is synergistic.

The viscosity is dependent on the shear rate within the flow regime of the hydrogel. The mechanism for this type of behavior is still somewhat unclear, but atomic level alignment of chain molecules is proported as one of the main explanations of this phenomenon. The

viscosity is certainly affected by the space between molecules, which is evident in viscosity vs. temperature graphs. The relevance of molecular volume and chain versus star polymers becomes clear and the combination of these effects is likely the main cause of shear thinning and other non-Newtonian fluid behaviors.

The capillary number is useful to interpret the importance of inertial forces and viscous forces compared with surface tension. For the constant flow rate of 0.02682 ml/s desired, the velocity profile is picture in figure 14, the important factor for assessing the importance of capillary number is the comparison of viscosity and surface tension. The surface tension is reduced by adding PEGDA or HPMC to deionized water, while viscosity is increased by adding PEGDA or HPMC. Thus the capillary number decreases as well reduce the concentration of H<sub>2</sub>O. It is observed that for viscous hydrogels that the magnitude of the capillary number for our experiment is approximately 1. That is, the interfacial tension of our hydrogel in room air at 25C are similar in magnitude to the viscous forces for the flow rate and geometry employed.

The Euler number expresses the magnitude of the pressure drop over the kinetic energy per unit volume. This provides a validation of the unique nature of micro-syringe extrusion where the relative value of the pressure enormously exceeds the kinetic energy within the flow.

The computational simulation provides a great source of unbiased information using Navier-Stokes momentum equations. However, once we have used experimental validation, the CFD comes to life and provides a valuable interpolation tool to expedite print settings and configuration for new hydrogels.

Patient specific geometry is a major advantage. It is important that the bioreactor flow regime pertains to the shape and flow pattern through the native vessel because this will reinforce the shape as the scaffold is developed by cells.

The mechanical properties provide feedback on the polymer matrix and the strength of the crosslinks between PEGDA chains. The main value of the biaxial testing is to be able to iterate through different hydrogels while being able to predict their mechanical properties based on the rule of mixtures and the any documented interaction effects. The Young's modulus for the constructs is larger, i.e. stiffer, for our construct than native vascular wall tissue, and the fracture strain is dramatically lower at 4% Green strain compared with over 25% for aortic tissue.

The relevant range of Young's modulus for cardiovascular TE is not defined because it is not certain. However, groups have had great success adhering cells to gelatin hydrogels with low concentrations and extremely low Young's modulus of 100 kPa. 10,000 kPa is reported as the Young's modulus for PLA/PGA based on research revealing cell attachment in totally different media <sup>24</sup>. The biaxial testing showed the effect of changing PEGDA concentration, although there is room to gather more data on the effect of changing the MWD of PEGDA monomers in the hydrogel, which is shown in the research to more strongly affect the mechanical properties of the crosslinked material. Larger MW PEGDA molecules are more expensive to synthesize and purify so they are prohibitively costly.

The viscometry plays a large role in deciphering the correct print configuration. The non-Newtonian behavior of the hydrogel complicates calculations for shear stress and predicted head loss given that they are both a function of flow rate in the system. The impact of non-Newtonian behavior is also seen in features like die swell (Barus effect), the Weissenberg effect and the Kayes effect which can be seen to some extent with most relevant hydrogels. These phenomena are driven by surface tension, shear thinning behavior and molecular polarity, respectively. These behaviors involve complex interactions between molecules but ultimately can be predicted and accommodated for extrusion.

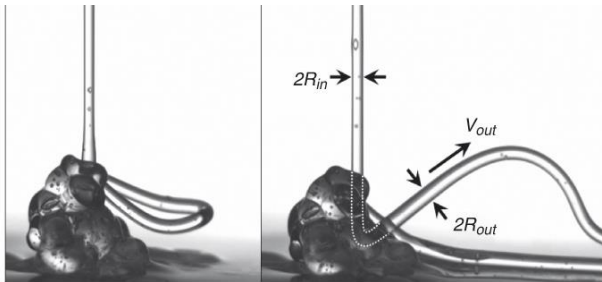


**Figure 73.** The Kayes effect is a product of the shear thinning behavior as the fast moving stream has low shear stress when it moves through the bulk material.

**Figure 74.** The Weissenberg effect is also due to the shear thinning behavior and shows dramatic contrast to Newtonian behavior.

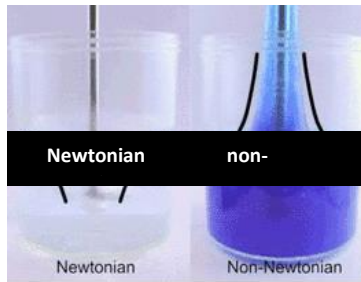


**Figure 75.** The Barus effect changes the cross-sectional area as flow leaves the nozzle, slowing its average velocity and affecting the print settings <sup>6</sup>.

The layer height and the layer width are critical printing parameters because of the aggregate effect of several hundred layers. In order to get them right the behavior of the hydrogel, the Q vs. P curve, and the patient specific geometry must all be considered. Based on the dimensions of the wall, the width of the print can be chosen, and the nozzle is chosen in light of the behavior of the hydrogel when extruded.

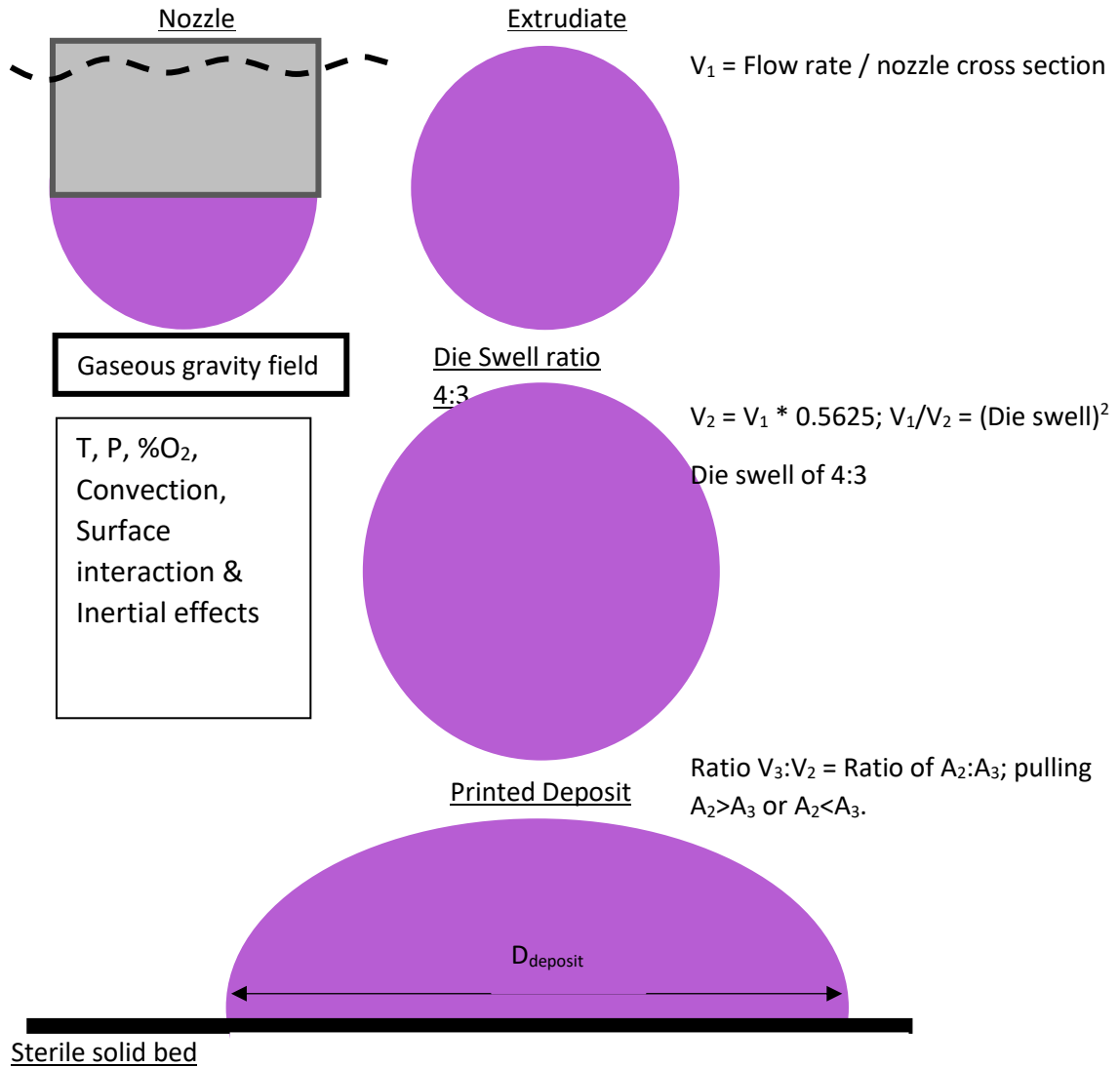


**Figure 76. First layer, matching nozzle flow rate,  $V_1 \cdot A_1$ , with print speed,  $V_3$ , by examining the cross sectional area, considering die swell, and using the law of continuity.**

Using CFD the parameters for printing are well informed, the chosen Q relates exactly to the print speed, print height and print width. The chosen Q can be related analytically with Hagen-Poiseuille's equation or related with CFD to the pressure required. This allows for tuning the print configuration and the chosen Q to the patient-specific geometry that needs to be printed.

## CHAPTER 7: CONCLUSIONS

Like a farmer who uses water, soil, and ultraviolet light to grow food: tissue engineering uses water, biocompatible polymers and a bioreactor. Understanding cellular behavior in the unique context of a TE scaffold is instrumental to success with TEVGs. Knowledge of biocompatible polymers and polymerization reactions and products is a huge advantage over imitating existing research. In the effort to progress efficiently, it will be useful to be able to predict the mechanical properties of constructs before expending the energy to make them. Evaluating the function of the bioreactor should be viewed in light of density of adhered cell within the scaffold and the change per unit time of the mechanical properties of the construct.

A valuable amount of insight from research with Raheimin Talukder on reperfusion of preserved hearts allowed me to work with at least 20 different pig hearts and closely work with them for hours. I was able to feel and work with the entire myocardium, the valves, the vessels and the intimate anatomy of the heart and adjacent anatomy. In understanding these tissues to some extent, the marvelous organization of native vessels appears clearly. It is with great humility that a tissue engineering scaffold seeks to employ cells to construct instinctively. Harnessing the organization so instinctive to cells will require iterative testing and therefore well designed methods for setting flow rate with novel non-Newtonian hydrogels and for predicting the mechanical properties of scaffolds.

New biocompatible copolymers with grafted functional groups for cell adhesion will become more available and sophisticated with time, but remain costly; however, current

research to define the working parameters of highly similar organic molecules will be relevant to the *atomically engineered* molecules that will ultimately drive the completion of decades of research pursuing TEVGs. Research to design software that connects viscometry, CFD, and pilot testing to configure print settings for a plethora of nozzle-based extrusion methods provides value by decreasing configuration times. Furthermore, this will be valuable for the duration of this process because it appears evident that while many fabrication methods exist, nozzle-based rapid prototyping provides a practical and sophisticated solution. Ultimately, it may be that ideal bioreactor protocol is the most important factor, and therein may require only the most fundamentally simple hydrogels and scaffold materials that are high in water content and create particularly spacious matrices for cells to advance unhindered. The ability to intricately design the polymerized matrix and the available bonding sites for cells may increase the functionality of high water content scaffolds that have sparse networks and begin with high Young's modulus and low burst pressures.

The work here has demonstrated that medium quality scaffolds can be printed by the beta version of this printer. In testing this prototype printer from BioBots, I have been able to validate CFD and I have successfully printed dozens of valves and vessels with good dimensional fidelity. This task required a great deal of practice working towards definitive configurations for the 3-D bioprinter in order to perceive all of the factors affecting print quality that have been discussed here.. This work is not novel but it illustrates several functional methods for setting up a nozzle-based extrusion of a non-Newtonian hydrogel for photoinitiated crosslinking into a scaffold of specific mechanical properties and atomic structure for cell adhesion.

This provides the basis to create a database of the configurations for printing scaffolds. This database can contain the viscosity curves for a hydrogel like PEGDA 700 at a range of

concentrations from 5-20% w/v, in addition to the viscosity data for a viscous additive like HPMC, understanding any interaction effects the viscosity of the mixed copolymer hydrogel can be reasonably predicted and further verified by direct viscometry of the hydrogel. With this viscous information the CFD simulation promises to offer a way to predict the flow rate and pressure relationship for that hydrogel with any printing geometry. Beyond the quintessential print settings and composition of ideal hydrogels for extrusion, the database can allow for cross-referencing of mechanical properties in order to have a prediction of the mechanical properties of the resulting scaffold before it is constructed. This requires extensive validation of CFD and relies heavily on experimental testing rather than computational complexity.

Non-Newtonian modeling is dynamic and requires post processing and customization of several boundary conditions to obtain nearly correct results. As CFD research moves forward non-Newtonian modeling will improve and the ability to predict pressure from flow rate for this challenging RP system. A 0.08mm nozzle may become fundamental to bioprinting of shear thinning hydrogels and this requires validation because FLUENT overestimates the shear rate and therefore underestimates total head loss for Power Law fluids.

Despite any limitations, the beta version of the BioBots bioprinter shows the miraculous work that is possible with RP technologies. With well reason work from a mechanical engineering standpoint, the viscosity and the mechanical properties can be connected to the % composition inputs and the polymer science of the photosensitive reaction. Contributions from many different fields have continued to advance TE constructs from petri dish cell culture to patient-specific geometries with tailored mechanical properties and functionalized polymer matrices with cell attachment sites.



## REFERENCES

- 1 Shinoka, T. *et al.* Creation of viable pulmonary artery autografts through tissue engineering. *The Journal of thoracic and cardiovascular surgery* **115**, 536-545; discussion 545-536, doi:10.1016/S0022-5223(98)70315-0 (1998).
- 2 Sodian, R. *et al.* Application of stereolithography for scaffold fabrication for tissue engineered heart valves. *ASAIO journal* **48**, 12-16 (2002).
- 3 Skardal, A. & Atala, A. Biomaterials for integration with 3-D bioprinting. *Annals of biomedical engineering* **43**, 730-746, doi:10.1007/s10439-014-1207-1 (2015).
- 4 Billiet, T., Vandenhoute, M., Schelfhout, J., Van Vlierberghe, S. & Dubruel, P. A review of trends and limitations in hydrogel-rapid prototyping for tissue engineering. *Biomaterials* **33**, 6020-6041, doi:10.1016/j.biomaterials.2012.04.050 (2012).
- 5 Mahler, G. J., Frendl, C. M., Cao, Q. & Butcher, J. T. Effects of shear stress pattern and magnitude on mesenchymal transformation and invasion of aortic valve endothelial cells. *Biotechnology and bioengineering* **111**, 2326-2337, doi:10.1002/bit.25291 (2014).
- 6 Oishi, C. M., Martins, F. P., Tomé, M. F., Cuminato, J. A. & McKee, S. Numerical solution of the eXtended Pom-Pom model for viscoelastic free surface flows. *Journal of Non-Newtonian Fluid Mechanics* **166**, 165-179, doi:10.1016/j.jnnfm.2010.11.001 (2011).
- 7 Al-Refai, M. A., Oueida, F. M., Lui, R. C., Al-Saif, S. M. & Al-Omran, H. M. Impressive echocardiographic images of a rare pathology: Aneurysm of the mitral valve - Report of two cases and review of the literature. *J Saudi Heart Assoc* **25**, 47-51, doi:10.1016/j.jsha.2012.11.002 (2013).
- 8 Velnar, T., Bunc, G., Klobucar, R. & Gradisnik, L. Biomaterials and host versus graft response: a short review. *Bosnian journal of basic medical sciences / Udruzenje basicnih medicinskih znanosti = Association of Basic Medical Sciences* **16**, 82-90, doi:10.17305/bjbms.2016.525 (2016).
- 9 Hasan, A. *et al.* Biomechanical properties of native and tissue engineered heart valve constructs. *Journal of biomechanics* **47**, 1949-1963, doi:10.1016/j.jbiomech.2013.09.023 (2014).
- 10 Blanksby, S. J. & Ellison, G. B. Bond dissociation energies of organic molecules. *Accounts of chemical research* **36**, 255-263, doi:10.1021/ar020230d (2003).
- 11 Azadani, A. N. *et al.* Comparison of mechanical properties of human ascending aorta and aortic sinuses. *The Annals of thoracic surgery* **93**, 87-94, doi:10.1016/j.athoracsur.2011.08.002 (2012).
- 12 Chang, S.-W. & Buehler, M. J. Molecular biomechanics of collagen molecules. *Materials Today* **17**, 70-76, doi:10.1016/j.mattod.2014.01.019 (2014).
- 13 Wiltz, D. *et al.* Extracellular Matrix Organization, Structure, and Function. doi:10.5772/52842 (2013).
- 14 Zanetti, P. P. *et al.* The dacron aorta. *The Journal of cardiovascular surgery* **39**, 307-310 (1998).
- 15 Azadani, A. N. *et al.* Biomechanical properties of human ascending thoracic aortic aneurysms. *The Annals of thoracic surgery* **96**, 50-58, doi:10.1016/j.athoracsur.2013.03.094 (2013).
- 16 Naito, Y. *et al.* Successful clinical application of tissue-engineered graft for extracardiac Fontan operation. *The Journal of thoracic and cardiovascular surgery* **125**, 419-420, doi:10.1067/mtc.2003.134 (2003).

- 17 Alavi, S. H., Sinha, A., Steward, E., Milliken, J. C. & Kheradvar, A. Load-dependent extracellular matrix organization in atrioventricular heart valves: differences and similarities. *Am J Physiol Heart Circ Physiol* **309**, H276-284, doi:10.1152/ajpheart.00164.2015 (2015).
- 18 Zemel, A. Active mechanical coupling between the nucleus, cytoskeleton and the extracellular matrix, and the implications for perinuclear actomyosin organization. *Soft matter* **11**, 2353-2363, doi:10.1039/c4sm02425g (2015).
- 19 Hay, E. D. Biogenesis and organization of extracellular matrix. *FASEB journal : official publication of the Federation of American Societies for Experimental Biology* **13 Suppl 2**, S281-283 (1999).
- 20 Hilenski, L. L., Terracio, L., Sawyer, R. & Borg, T. K. Effects of extracellular matrix on cytoskeletal and myofibrillar organization in vitro. *Scanning Microsc* **3**, 535-548 (1989).
- 21 van der Kamp, A. W. & Nauta, J. Fibroblast function and the maintenance of the aortic-valve matrix. *Cardiovascular research* **13**, 167-172 (1979).
- 22 Tseng, Q. *et al.* Spatial organization of the extracellular matrix regulates cell-cell junction positioning. *Proceedings of the National Academy of Sciences of the United States of America* **109**, 1506-1511, doi:10.1073/pnas.1106377109 (2012).
- 23 Papadaki, M. *et al.* Tissue engineering of functional cardiac muscle: molecular, structural, and electrophysiological studies. *Am J Physiol Heart Circ Physiol* **280**, H168-178 (2001).
- 24 Lee, Y. U. *et al.* Rational design of an improved tissue-engineered vascular graft: determining the optimal cell dose and incubation time. *Regenerative medicine* **11**, 159-167, doi:10.2217/rme.15.85 (2016).
- 25 Dixit, P., Hern-Anderson, D., Ranieri, J. & Schmidt, C. E. Vascular graft endothelialization: comparative analysis of canine and human endothelial cell migration on natural biomaterials. *Journal of biomedical materials research* **56**, 545-555 (2001).
- 26 Radomski, J. S., Jarrell, B. E., Pratt, K. J. & Williams, S. K. Effects of in vitro aging on human endothelial cell adherence to dacron vascular graft material. *The Journal of surgical research* **47**, 173-177 (1989).
- 27 Shi, Q. *et al.* Proof of fallout endothelialization of impervious Dacron grafts in the aorta and inferior vena cava of the dog. *Journal of vascular surgery* **20**, 546-556; discussion 556-547 (1994).
- 28 Yavuz, K. *et al.* Comparison of the endothelialization of small intestinal submucosa, dacron, and expanded polytetrafluoroethylene suspended in the thoracoabdominal aorta in sheep. *Journal of vascular and interventional radiology : JVIR* **17**, 873-882, doi:10.1097/01.RVI.0000217938.20787.BB (2006).
- 29 Cha, C., Liechty, W. B., Khademhosseini, A. & Peppas, N. A. Designing biomaterials to direct stem cell fate. *ACS nano* **6**, 9353-9358, doi:10.1021/nn304773b (2012).
- 30 Chiu, Y. N., Norris, R. A., Mahler, G., Recknagel, A. & Butcher, J. T. Transforming growth factor beta, bone morphogenetic protein, and vascular endothelial growth factor mediate phenotype maturation and tissue remodeling by embryonic valve progenitor cells: relevance for heart valve tissue engineering. *Tissue engineering. Part A* **16**, 3375-3383, doi:10.1089/ten.tea.2010.0027 (2010).
- 31 Gerecht-Nir, S. *et al.* Biophysical regulation during cardiac development and application to tissue engineering. *The International journal of developmental biology* **50**, 233-243, doi:10.1387/ijdb.052041sg (2006).

- 32 Yang, D., Guo, T., Nie, C. & Morris, S. F. Tissue-engineered blood vessel graft produced by self-derived cells and allogenic acellular matrix: a functional performance and histologic study. *Annals of plastic surgery* **62**, 297-303, doi:10.1097/SAP.0b013e318197eb19 (2009).
- 33 Capulli, A. K., MacQueen, L. A., Sheehy, S. P. & Parker, K. K. Fibrous scaffolds for building hearts and heart parts. *Advanced drug delivery reviews* **96**, 83-102, doi:10.1016/j.addr.2015.11.020 (2016).
- 34 Park, H., Larson, B. L., Kolewe, M. E., Vunjak-Novakovic, G. & Freed, L. E. Biomimetic scaffold combined with electrical stimulation and growth factor promotes tissue engineered cardiac development. *Experimental cell research* **321**, 297-306, doi:10.1016/j.yexcr.2013.11.005 (2014).
- 35 Alavi, S. H., Ruiz, V., Krasieva, T., Botvinick, E. L. & Kheradvar, A. Characterizing the collagen fiber orientation in pericardial leaflets under mechanical loading conditions. *Annals of biomedical engineering* **41**, 547-561, doi:10.1007/s10439-012-0696-z (2013).
- 36 Butcher, J. T., Simmons, C. A. & Warnock, J. N. Mechanobiology of the aortic heart valve. *The Journal of heart valve disease* **17**, 62-73 (2008).
- 37 Carrier, R. L. *et al.* Cardiac tissue engineering: cell seeding, cultivation parameters, and tissue construct characterization. *Biotechnology and bioengineering* **64**, 580-589 (1999).
- 38 El-Hamamsy, I., Chester, A. H. & Yacoub, M. H. Cellular regulation of the structure and function of aortic valves. *Journal of Advanced Research* **1**, 5-12, doi:10.1016/j.jare.2010.02.007 (2010).
- 39 Ku, C. H. *et al.* Collagen synthesis by mesenchymal stem cells and aortic valve interstitial cells in response to mechanical stretch. *Cardiovascular research* **71**, 548-556, doi:10.1016/j.cardiores.2006.03.022 (2006).
- 40 Hinton, R. B., Jr. *et al.* Extracellular matrix remodeling and organization in developing and diseased aortic valves. *Circulation research* **98**, 1431-1438, doi:10.1161/01.RES.0000224114.65109.4e (2006).
- 41 Heinz, A. *et al.* Molecular-level characterization of elastin-like constructs and human aortic elastin. *Matrix biology : journal of the International Society for Matrix Biology* **38**, 12-21, doi:10.1016/j.matbio.2014.07.006 (2014).
- 42 Kantorova, V. I. The spatial-temporal organization of the extracellular matrix. *Ontogenез* **25**, 14-30 (1994).
- 43 Cramer, J. W. *et al.* Aortic aneurysms remain a significant source of morbidity and mortality after use of Dacron((R)) patch aortoplasty to repair coarctation of the aorta: results from a single center. *Pediatric cardiology* **34**, 296-301, doi:10.1007/s00246-012-0442-1 (2013).
- 44 De Paulis, R. *et al.* A third generation of ascending aorta Dacron graft: preliminary experience. *The Annals of thoracic surgery* **85**, 305-309, doi:10.1016/j.athoracsur.2007.05.073 (2008).
- 45 Furukoshi, M., Moriwaki, T. & Nakayama, Y. Development of an in vivo tissue-engineered vascular graft with designed wall thickness (biotube type C) based on a novel caged mold. *Journal of artificial organs : the official journal of the Japanese Society for Artificial Organs* **19**, 54-61, doi:10.1007/s10047-015-0859-4 (2016).
- 46 Khalil, A., Helmy, T. & Porembka, D. T. Aortic pathology: aortic trauma, debris, dissection, and aneurysm. *Critical care medicine* **35**, S392-400, doi:10.1097/01.CCM.0000270276.01938.C0 (2007).

- 47 Berry, C. L., Sosa-Melgarejo, J. A. & Greenwald, S. E. The relationship between wall tension, lamellar thickness, and intercellular junctions in the fetal and adult aorta: its relevance to the pathology of dissecting aneurysm. *The Journal of pathology* **169**, 15-20, doi:10.1002/path.1711690104 (1993).
- 48 Schoenberg, S. O. *et al.* Abdominal aortic aneurysm. Detection of multilevel vascular pathology by time-resolved multiphase 3D gadolinium MR angiography: initial report. *Invest Radiol* **34**, 648-659 (1999).
- 49 Giagtzidis, I. T., Konstantinidis, K., Kalogirou, T. E., Karkos, C. D. & Papazoglou, K. O. Use of Endurant Stent-Graft Aortic Extensions for the Treatment of Focal Aortic Pathology. *Annals of vascular surgery* **36**, 99-105, doi:10.1016/j.avsg.2016.03.017 (2016).
- 50 Chester, A. H. & Taylor, P. M. Molecular and functional characteristics of heart-valve interstitial cells. *Philosophical transactions of the Royal Society of London. Series B, Biological sciences* **362**, 1437-1443, doi:10.1098/rstb.2007.2126 (2007).
- 51 Vunjak-Novakovic, G. *et al.* Dynamic cell seeding of polymer scaffolds for cartilage tissue engineering. *Biotechnology progress* **14**, 193-202, doi:10.1021/bp970120j (1998).
- 52 Tanford, C. Membrane Transport: Transport and Diffusion across Cell Membranes. *Science* **233**, 898, doi:10.1126/science.233.4766.898 (1986).
- 53 Domnina, L. V., Ivanova, O. Y. & Vasiliev, J. M. Effect of microtubule-specific drugs upon spatial organization of extracellular matrix in fibroblastic cultures. *Cell Biol Int* **19**, 743-748, doi:10.1006/cbir.1995.1125 (1995).
- 54 Ofek, G., Wiltz, D. C. & Athanasiou, K. A. Contribution of the cytoskeleton to the compressive properties and recovery behavior of single cells. *Biophysical journal* **97**, 1873-1882, doi:10.1016/j.bpj.2009.07.050 (2009).
- 55 Dale, M. A. *et al.* Elastin-Derived Peptides Promote Abdominal Aortic Aneurysm Formation by Modulating M1/M2 Macrophage Polarization. *Journal of immunology* **196**, 4536-4543, doi:10.4049/jimmunol.1502454 (2016).
- 56 Ijaz, T., Tilton, R. G. & Brasier, A. R. Cytokine amplification and macrophage effector functions in aortic inflammation and abdominal aortic aneurysm formation. *J Thorac Dis* **8**, E746-754, doi:10.21037/jtd.2016.06.37 (2016).
- 57 Halstenberg, S., Panitch, A., Rizzi, S., Hall, H. & Hubbell, J. A. Biologically engineered protein-graft-poly(ethylene glycol) hydrogels: a cell adhesive and plasmin-degradable biosynthetic material for tissue repair. *Biomacromolecules* **3**, 710-723 (2002).
- 58 Manwaring, M. E., Walsh, J. F. & Tresco, P. A. Contact guidance induced organization of extracellular matrix. *Biomaterials* **25**, 3631-3638, doi:10.1016/j.biomaterials.2003.10.043 (2004).
- 59 Cohen, S. *et al.* Design of synthetic polymeric structures for cell transplantation and tissue engineering. *Clinical materials* **13**, 3-10 (1993).
- 60 Bures, P., Huang, Y., Oral, E. & Peppas, N. A. Surface modifications and molecular imprinting of polymers in medical and pharmaceutical applications. *Journal of controlled release : official journal of the Controlled Release Society* **72**, 25-33 (2001).
- 61 Cima, L. G. *et al.* Tissue engineering by cell transplantation using degradable polymer substrates. *Journal of biomechanical engineering* **113**, 143-151 (1991).
- 62 Godard, F. *et al.* Aneurysm formation on dacron prosthesis after 84 months of use. Pathology, structural and chemical evaluation of the explanted device. *Journal des maladies vasculaires* **6**, 167-171 (1981).

- 63 Meinel, L. *et al.* Engineering bone-like tissue in vitro using human bone marrow stem cells and silk scaffolds. *Journal of biomedical materials research. Part A* **71**, 25-34, doi:10.1002/jbm.a.30117 (2004).
- 64 Zhu, J. Bioactive modification of poly(ethylene glycol) hydrogels for tissue engineering. *Biomaterials* **31**, 4639-4656, doi:10.1016/j.biomaterials.2010.02.044 (2010).
- 65 Brunski, J. B. Biomaterials and biomechanics in dental implant design. *The International journal of oral & maxillofacial implants* **3**, 85-97 (1988).
- 66 Curtis, J. W., Jr. Chemical and mechanical properties of metallic implant biomaterials. *The Journal of the Tennessee Dental Association* **66**, 44-46 (1986).
- 67 Xie, C., Lu, H., Li, W., Chen, F. M. & Zhao, Y. M. The use of calcium phosphate-based biomaterials in implant dentistry. *Journal of materials science. Materials in medicine* **23**, 853-862, doi:10.1007/s10856-011-4535-9 (2012).
- 68 Mabry, K. M., Lawrence, R. L. & Anseth, K. S. Dynamic stiffening of poly(ethylene glycol)-based hydrogels to direct valvular interstitial cell phenotype in a three-dimensional environment. *Biomaterials* **49**, 47-56, doi:10.1016/j.biomaterials.2015.01.047 (2015).
- 69 Smith, S. D. & Millar, E. A. Arthrorisis by means of a subtalar polyethylene peg implant for correction of hindfoot pronation in children. *Clinical orthopaedics and related research*, 15-23 (1983).
- 70 Heuts, J. *et al.* Bio-functionalized star PEG-coated PVDF surfaces for cytocompatibility-improved implant components. *Journal of biomedical materials research. Part A* **92**, 1538-1551, doi:10.1002/jbm.a.32478 (2010).
- 71 Mooney, D. J., Breuer, C., McNamara, K., Vacanti, J. P. & Langer, R. Fabricating tubular devices from polymers of lactic and glycolic Acid for tissue engineering. *Tissue engineering* **1**, 107-118, doi:10.1089/ten.1995.1.107 (1995).
- 72 Albertini, G. *et al.* Organization of extracellular matrix fibers within polyglycolic acid-poly(lactic acid) scaffolds analyzed using X-ray synchrotron-radiation phase-contrast micro computed tomography. *Tissue engineering. Part C, Methods* **15**, 403-411, doi:10.1089/ten.tec.2008.0270 (2009).
- 73 Fairbanks, B. D., Schwartz, M. P., Bowman, C. N. & Anseth, K. S. Photoinitiated polymerization of PEG-diacrylate with lithium phenyl-2,4,6-trimethylbenzoylphosphinate: polymerization rate and cytocompatibility. *Biomaterials* **30**, 6702-6707, doi:10.1016/j.biomaterials.2009.08.055 (2009).
- 74 Lee, H. J., Sen, A., Bae, S., Lee, J. S. & Webb, K. Poly(ethylene glycol) diacrylate/hyaluronic acid semi-interpenetrating network compositions for 3-D cell spreading and migration. *Acta biomaterialia* **14**, 43-52, doi:10.1016/j.actbio.2014.12.007 (2015).
- 75 Pouliot, R. *et al.* Tissue engineering of fish skin: behavior of fish cells on poly(ethylene glycol terephthalate)/poly(butylene terephthalate) copolymers in relation to the composition of the polymer substrate as an initial step in constructing a robotic/living tissue hybrid. *Tissue engineering* **10**, 7-21, doi:10.1089/107632704322791655 (2004).
- 76 Dragan, E. S. Design and applications of interpenetrating polymer network hydrogels. A review. *Chemical Engineering Journal* **243**, 572-590, doi:10.1016/j.cej.2014.01.065 (2014).
- 77 Parenteau-Bareil, R., Gauvin, R. & Berthod, F. Collagen-Based Biomaterials for Tissue Engineering Applications. *Materials* **3**, 1863-1887, doi:10.3390/ma3031863 (2010).
- 78 Vader, D. Strain induced alignment in collagen gels. *PLoS ONE* **4**, doi:10.1371/journal.pone.0005902.g001 (2009).

- 79 Machado, R. *et al.* Exploring the Properties of Genetically Engineered Silk-Elastin-Like Protein Films. *Macromolecular bioscience* **15**, 1698-1709, doi:10.1002/mabi.201500132 (2015).
- 80 McKenna, K. A. *et al.* Mechanical property characterization of electrospun recombinant human tropoelastin for vascular graft biomaterials. *Acta biomaterialia* **8**, 225-233, doi:10.1016/j.actbio.2011.08.001 (2012).
- 81 Das, S. *et al.* Bioprintable, cell-laden silk fibroin-gelatin hydrogel supporting multilineage differentiation of stem cells for fabrication of three-dimensional tissue constructs. *Acta biomaterialia* **11**, 233-246, doi:10.1016/j.actbio.2014.09.023 (2015).
- 82 Sun, X. *et al.* Development of a hybrid gelatin hydrogel platform for tissue engineering and protein delivery applications. *J. Mater. Chem. B* **3**, 6368-6376, doi:10.1039/c5tb00645g (2015).
- 83 Bertassoni, L. E. *et al.* Direct-write bioprinting of cell-laden methacrylated gelatin hydrogels. *Biofabrication* **6**, 024105, doi:10.1088/1758-5082/6/2/024105 (2014).
- 84 Santoro, M., Tataru, A. M. & Mikos, A. G. Gelatin carriers for drug and cell delivery in tissue engineering. *Journal of controlled release : official journal of the Controlled Release Society* **190**, 210-218, doi:10.1016/j.jconrel.2014.04.014 (2014).
- 85 Duan, B., Hockaday, L. A., Kang, K. H. & Butcher, J. T. 3D bioprinting of heterogeneous aortic valve conduits with alginate/gelatin hydrogels. *Journal of biomedical materials research. Part A* **101**, 1255-1264, doi:10.1002/jbm.a.34420 (2013).
- 86 Goeau-Brissonniere, O. *et al.* Prevention of vascular graft infection by rifampin bonding to a gelatin-sealed Dacron graft. *Annals of vascular surgery* **5**, 408-412, doi:10.1007/BF02133043 (1991).
- 87 Jordan, G. L., Jr., Stump, M. M., Allen, J., De Bakey, M. E. & Halpert, B. Gelatin-impregnated Dacron prosthesis implanted into porcine thoracic aorta. *Surgery* **53**, 45-51 (1963).
- 88 Sarkar, S., Dadhania, M., Rourke, P., Desai, T. A. & Wong, J. Y. Vascular tissue engineering: microtextured scaffold templates to control organization of vascular smooth muscle cells and extracellular matrix. *Acta biomaterialia* **1**, 93-100, doi:10.1016/j.actbio.2004.08.003 (2005).
- 89 McDonald, J. A., Kelley, D. G. & Broekelmann, T. J. Role of fibronectin in collagen deposition: Fab' to the gelatin-binding domain of fibronectin inhibits both fibronectin and collagen organization in fibroblast extracellular matrix. *J Cell Biol* **92**, 485-492 (1982).
- 90 Brown, A. C. & Barker, T. H. Fibrin-based biomaterials: modulation of macroscopic properties through rational design at the molecular level. *Acta biomaterialia* **10**, 1502-1514, doi:10.1016/j.actbio.2013.09.008 (2014).
- 91 Costa Jde, O. *et al.* Structural and functional comparison of proteolytic enzymes from plant latex and snake venoms. *Biochimie* **92**, 1760-1765, doi:10.1016/j.biochi.2010.09.002 (2010).
- 92 Fischer, K. M. *et al.* Poly(Limonene Thioether) Scaffold for Tissue Engineering. *Advanced healthcare materials* **5**, 813-821, doi:10.1002/adhm.201500892 (2016).
- 93 Vellayappan, M. V. *et al.* Multifaceted prospects of nanocomposites for cardiovascular grafts and stents. *International journal of nanomedicine* **10**, 2785-2803, doi:10.2147/IJN.S80121 (2015).

- 94 Han, F. *et al.* Woven silk fabric-reinforced silk nanofibrous scaffolds for regenerating load-bearing soft tissues. *Acta biomaterialia* **10**, 921-930, doi:10.1016/j.actbio.2013.09.026 (2014).
- 95 Sakhenberg, E. I., Nikolaenko, N. S. & Pinaev, G. P. [Actin cytoskeleton organization and spreading of bone marrow stromal cells and cartilage cells during their combined and independent cultivation on different extracellular matrix proteins]. *Tsitologiya* **56**, 708-716 (2014).
- 96 Lawyer, T., McIntosh, K., Clavijo, C., Potekhina, L. & Mann, B. K. Formulation Changes Affect Material Properties and Cell Behavior in HA-Based Hydrogels. *International journal of cell biology* **2012**, 737421, doi:10.1155/2012/737421 (2012).
- 97 Jia, J. *et al.* Engineering alginate as bioink for bioprinting. *Acta biomaterialia* **10**, 4323-4331, doi:10.1016/j.actbio.2014.06.034 (2014).
- 98 Bayer, C. L., Herrero, E. P. & Peppas, N. A. Alginate films as macromolecular imprinted matrices. *Journal of biomaterials science. Polymer edition* **22**, 1523-1534, doi:10.1163/092050610X514115 (2011).
- 99 Stevens, M. M., Qanadilo, H. F., Langer, R. & Prasad Shastri, V. A rapid-curing alginate gel system: utility in periosteum-derived cartilage tissue engineering. *Biomaterials* **25**, 887-894 (2004).
- 100 Jiang, G., Sun, J. & Ding, F. PEG-g-chitosan thermosensitive hydrogel for implant drug delivery: cytotoxicity, in vivo degradation and drug release. *Journal of biomaterials science. Polymer edition* **25**, 241-256, doi:10.1080/09205063.2013.851542 (2014).
- 101 Zhou, C. & Wu, Q. A novel polyacrylamide nanocomposite hydrogel reinforced with natural chitosan nanofibers. *Colloids and surfaces. B, Biointerfaces* **84**, 155-162, doi:10.1016/j.colsurfb.2010.12.030 (2011).
- 102 Berger, J. *et al.* Structure and interactions in covalently and ionically crosslinked chitosan hydrogels for biomedical applications. *European journal of pharmaceuticals and biopharmaceutics : official journal of Arbeitsgemeinschaft fur Pharmazeutische Verfahrenstechnik e.V* **57**, 19-34 (2004).
- 103 Fujita, M. *et al.* Inhibition of vascular prosthetic graft infection using a photocrosslinkable chitosan hydrogel. *The Journal of surgical research* **121**, 135-140, doi:10.1016/j.jss.2004.04.010 (2004).
- 104 Alves, C. M. *et al.* Modulating bone cells response onto starch-based biomaterials by surface plasma treatment and protein adsorption. *Biomaterials* **28**, 307-315, doi:10.1016/j.biomaterials.2006.09.010 (2007).
- 105 Costa, S. A. & Reis, R. L. Immobilisation of catalase on the surface of biodegradable starch-based polymers as a way to change its surface characteristics. *Journal of materials science. Materials in medicine* **15**, 335-342 (2004).
- 106 Oh, C. M., Ru Shan Siow, C., Heng, P. W. & Chan, L. W. Impact of HPMC on the physical properties of spray-congealed PEG microparticles and its swelling effect on rifampicin dissolution. *Drug development and industrial pharmacy* **42**, 403-411, doi:10.3109/03639045.2015.1061536 (2016).
- 107 Oh, C. M., Heng, P. W. & Chan, L. W. A study on the impact of hydroxypropyl methylcellulose on the viscosity of PEG melt suspensions using surface plots and principal component analysis. *AAPS PharmSciTech* **16**, 466-477, doi:10.1208/s12249-014-0204-x (2015).

- 108 Ding, C., Zhang, M., Tian, H. & Li, G. Effect of hydroxypropyl methylcellulose on collagen fibril formation in vitro. *International journal of biological macromolecules* **52**, 319-326, doi:10.1016/j.ijbiomac.2012.10.003 (2013).
- 109 Siepmann, J. & Peppas, N. A. Modeling of drug release from delivery systems based on hydroxypropyl methylcellulose (HPMC). *Advanced drug delivery reviews* **48**, 139-157 (2001).
- 110 Qin, G. *et al.* Expression, cross-linking, and characterization of recombinant chitin binding resilin. *Biomacromolecules* **10**, 3227-3234, doi:10.1021/bm900735g (2009).
- 111 van Beilen, J. B. & Poirier, Y. Prospects for biopolymer production in plants. *Adv Biochem Eng Biotechnol* **107**, 133-151, doi:10.1007/10\_2007\_056 (2007).
- 112 Pashkuleva, I., Marques, A. P., Vaz, F. & Reis, R. L. Surface modification of starch based blends using potassium permanganate-nitric acid system and its effect on the adhesion and proliferation of osteoblast-like cells. *Journal of materials science. Materials in medicine* **16**, 81-92, doi:10.1007/s10856-005-6450-4 (2005).
- 113 Lee, W. & Park, J. 3D patterned stem cell differentiation using thermo-responsive methylcellulose hydrogel molds. *Scientific reports* **6**, 29408, doi:10.1038/srep29408 (2016).
- 114 Basumallick, L., Ji, J. A., Naber, N. & Wang, Y. J. The fate of free radicals in a cellulose based hydrogel: detection by electron paramagnetic resonance spectroscopy. *Journal of pharmaceutical sciences* **98**, 2464-2471, doi:10.1002/jps.21632 (2009).
- 115 Guilak, F. & Baaijens, F. P. Functional tissue engineering: Ten more years of progress. *Journal of biomechanics* **47**, 1931-1932, doi:10.1016/j.jbiomech.2014.04.003 (2014).
- 116 Heinrich, D. *et al.* Synthesis Gas (Syngas)-Derived Medium-Chain-Length Polyhydroxyalkanoate Synthesis in Engineered *Rhodospirillum rubrum*. *Applied and environmental microbiology* **82**, 6132-6140, doi:10.1128/AEM.01744-16 (2016).
- 117 Sudesh, K. Microbial polyhydroxyalkanoates (PHAs): an emerging biomaterial for tissue engineering and therapeutic applications. *The Medical journal of Malaysia* **59 Suppl B**, 55-56 (2004).
- 118 Lee, S. Y. Bacterial polyhydroxyalkanoates. *Biotechnology and bioengineering* **49**, 1-14, doi:10.1002/(SICI)1097-0290(19960105)49:1<1::AID-BIT1>3.0.CO;2-P (1996).
- 119 Puertolas, J. A. *et al.* Compression behaviour of biphasic calcium phosphate and biphasic calcium phosphate-agarose scaffolds for bone regeneration. *Acta biomaterialia* **7**, 841-847, doi:10.1016/j.actbio.2010.07.032 (2011).
- 120 Norotte, C., Marga, F. S., Niklason, L. E. & Forgacs, G. Scaffold-free vascular tissue engineering using bioprinting. *Biomaterials* **30**, 5910-5917, doi:10.1016/j.biomaterials.2009.06.034 (2009).
- 121 Zhang, X. *et al.* Integrating valve-inspired design features into poly(ethylene glycol) hydrogel scaffolds for heart valve tissue engineering. *Acta biomaterialia* **14**, 11-21, doi:10.1016/j.actbio.2014.11.042 (2015).
- 122 Toh, J. B. <Synthesis\_and\_Characterisation\_of\_PEGDA-based\_Hydrogels\_2011.pdf>. (2011).
- 123 Beamish, J. A., Zhu, J., Kottke-Marchant, K. & Marchant, R. E. The effects of monoacrylated poly(ethylene glycol) on the properties of poly(ethylene glycol) diacrylate hydrogels used for tissue engineering. *Journal of biomedical materials research. Part A* **92**, 441-450, doi:10.1002/jbm.a.32353 (2010).



- 124 Beamish, J. A. *et al.* The influence of RGD-bearing hydrogels on the re-expression of contractile vascular smooth muscle cell phenotype. *Biomaterials* **30**, 4127-4135, doi:10.1016/j.biomaterials.2009.04.038 (2009).
- 125 Ke, Y., Wu, G. & Wang, Y. PHBV/PAM scaffolds with local oriented structure through UV polymerization for tissue engineering. *BioMed research international* **2014**, 157987, doi:10.1155/2014/157987 (2014).
- 126 Zhou, C., Wu, Q., Yue, Y. & Zhang, Q. Application of rod-shaped cellulose nanocrystals in polyacrylamide hydrogels. *Journal of colloid and interface science* **353**, 116-123, doi:10.1016/j.jcis.2010.09.035 (2011).
- 127 Ke, Y. *et al.* Photografting polymerization of polyacrylamide on PHBV films (I). *Journal of Applied Polymer Science* **104**, 4088-4095, doi:10.1002/app.25678 (2007).
- 128 Russo, P. A., Bouchard, C. S. & Galasso, J. M. Extended-wear silicone hydrogel soft contact lenses in the management of moderate to severe dry eye signs and symptoms secondary to graft-versus-host disease. *Eye & contact lens* **33**, 144-147, doi:10.1097/01.icl.0000244154.76214.2d (2007).
- 129 Peppas, N. A. & Yang, W. H. Properties-based optimization of the structure of polymers for contract lens applications. *Contact and intraocular lens medical journal* **7**, 300-314 (1981).
- 130 Wu, H. *et al.* New understanding of microstructure formation of the rubber phase in thermoplastic vulcanizates (TPV). *Soft matter* **10**, 1816-1822, doi:10.1039/c3sm52375f (2014).
- 131 Chen, Y., Xu, C., Liang, X. & Cao, L. In situ reactive compatibilization of polypropylene/ethylene-propylene-diene monomer thermoplastic vulcanizate by zinc dimethacrylate via peroxide-induced dynamic vulcanization. *The journal of physical chemistry. B* **117**, 10619-10628, doi:10.1021/jp404427w (2013).
- 132 Kamil, S. H., Eavey, R. D., Vacanti, M. P., Vacanti, C. A. & Hartnick, C. J. Tissue-engineered cartilage as a graft source for laryngotracheal reconstruction: a pig model. *Archives of otolaryngology--head & neck surgery* **130**, 1048-1051, doi:10.1001/archotol.130.9.1048 (2004).
- 133 Dornelas, K. L., Dossi, N. & Piccin, E. A simple method for patterning poly(dimethylsiloxane) barriers in paper using contact-printing with low-cost rubber stamps. *Analytica chimica acta* **858**, 82-90, doi:10.1016/j.aca.2014.11.025 (2015).
- 134 Rajan, K. P., Al-Ghamdi, A., Parameswar, R. & Nando, G. B. Blends of thermoplastic polyurethane and polydimethylsiloxane rubber: assessment of biocompatibility and suture holding strength of membranes. *International journal of biomaterials* **2013**, 240631, doi:10.1155/2013/240631 (2013).
- 135 Wang, Z. *et al.* Bioinspired design of nanostructured elastomers with cross-linked soft matrix grafting on the oriented rigid nanofibers to mimic mechanical properties of human skin. *ACS nano* **9**, 271-278, doi:10.1021/nn506960f (2015).
- 136 Chai, W. Y. *et al.* Synthesis of polyisoprene terpenoid dendrons and their applications in oligo(phenylene ethynylene)s as "shells". *Chemistry, an Asian journal* **7**, 143-155, doi:10.1002/asia.201100480 (2012).
- 137 Mooibroek, H. & Cornish, K. Alternative sources of natural rubber. *Applied microbiology and biotechnology* **53**, 355-365 (2000).
- 138 Kanyanta, V. & Ivankovic, A. Mechanical characterisation of polyurethane elastomer for biomedical applications. *Journal of the mechanical behavior of biomedical materials* **3**, 51-62, doi:10.1016/j.jmbbm.2009.03.005 (2010).

- 139 Behrend, D. & Schmitz, K. P. [Polyurethane or silicone as long-term implant substance--a critical evaluation]. *Biomedizinische Technik. Biomedical engineering* **38**, 172-178 (1993).
- 140 Szycher, M. & Reed, A. M. Biostable polyurethane elastomers. *Med Device Technol* **3**, 42-51 (1992).
- 141 Jaganathan, S. K., Supriyanto, E., Murugesan, S., Balaji, A. & Asokan, M. K. Biomaterials in cardiovascular research: applications and clinical implications. *BioMed research international* **2014**, 459465, doi:10.1155/2014/459465 (2014).
- 142 Wang, W., Ouyang, Y. & Poh, C. K. Orthopaedic implant technology: biomaterials from past to future. *Annals of the Academy of Medicine, Singapore* **40**, 237-244 (2011).
- 143 Furqan Muhammad, I., Mahmood, A. & Aysha, R. Synthesis and in Vitro Characterization of Hydroxypropyl Methylcellulose-Graft-Poly (Acrylic Acid/2-Acrylamido-2-Methyl-1-Propanesulfonic Acid) Polymeric Network for Controlled Release of Captopril. *Acta poloniae pharmaceutica* **73**, 183-196 (2016).
- 144 Shenogin, S. & Ozisik, R. Deformation of glassy polycarbonate and polystyrene: the influence of chemical structure and local environment. *Polymer* **46**, 4397-4404, doi:10.1016/j.polymer.2005.03.015 (2005).
- 145 Thakker, M. M., Zhang, J. & Sires, B. S. Chronic inflammation from polycarbonate motility peg inhibits osteogenesis in a human hydroxyapatite orbital implant. *Ophthalm Plast Reconstr Surg* **21**, 399-401 (2005).
- 146 Pinchuk, L. *et al.* Medical applications of poly(styrene-block-isobutylene-block-styrene) ("SIBS"). *Biomaterials* **29**, 448-460, doi:10.1016/j.biomaterials.2007.09.041 (2008).
- 147 Harel, E., Meltzer, S. E., Requicha, A. A., Thompson, M. E. & Koel, B. E. Fabrication of polystyrene latex nanostructures by nanomanipulation and thermal processing. *Nano letters* **5**, 2624-2629, doi:10.1021/nl0342592 (2005).
- 148 Leone, G. *et al.* A PVA/PVP hydrogel for human lens substitution: Synthesis, rheological characterization, and in vitro biocompatibility. *Journal of biomedical materials research. Part B, Applied biomaterials* **97**, 278-288, doi:10.1002/jbm.b.31813 (2011).
- 149 Peppas, N. A. & Merrill, E. W. Development of semicrystalline poly(vinyl alcohol) hydrogels for biomedical applications. *Journal of biomedical materials research* **11**, 423-434, doi:10.1002/jbm.820110309 (1977).
- 150 Xiang, F., Ward, S. M., Givens, T. M. & Grunlan, J. C. Structural tailoring of hydrogen-bonded poly(acrylic acid)/poly(ethylene oxide) multilayer thin films for reduced gas permeability. *Soft matter* **11**, 1001-1007, doi:10.1039/c4sm02363c (2015).
- 151 Lue, S. J. *et al.* Micron- and nano-sized poly(N-isopropylacrylamide-co-acrylic acid) latex syntheses and their applications for controlled drug release. *Journal of nanoscience and nanotechnology* **13**, 5305-5315 (2013).
- 152 Lee, A. L. S. <Novel Glycerol-Crosslinked PAA hydrogel\_ Phillipines.2011.pdf>. *Phillipine Science Letters* (2011).
- 153 Padavan, D. T., Hamilton, A. M., Millon, L. E., Boughner, D. R. & Wan, W. Synthesis, characterization and in vitro cell compatibility study of a poly(amic acid) graft/cross-linked poly(vinyl alcohol) hydrogel. *Acta biomaterialia* **7**, 258-267, doi:10.1016/j.actbio.2010.07.038 (2011).
- 154 Kong, X. & Narine, S. S. Sequential interpenetrating polymer networks produced from vegetable oil based polyurethane and poly(methyl methacrylate). *Biomacromolecules* **9**, 2221-2229, doi:10.1021/bm800335x (2008).
- 155 Huang, J., Best, S. M., Brooks, R. A., Rushton, N. & Bonfield, W. In vitro evaluation of nanosized carbonate-substituted hydroxyapatite and its polyhydroxyethylmethacrylate

- nanocomposite. *Journal of biomedical materials research. Part A* **87**, 598-607, doi:10.1002/jbm.a.31815 (2008).
- 156 Giandalia, G., De Caro, V., Cordone, L. & Giannola, L. I. Trehalose-hydroxyethylcellulose microspheres containing vancomycin for topical drug delivery. *European journal of pharmaceutics and biopharmaceutics : official journal of Arbeitsgemeinschaft fur Pharmazeutische Verfahrenstechnik e.V* **52**, 83-89 (2001).
- 157 Peppas, N. A., Moynihan, H. J. & Lucht, L. M. The structure of highly crosslinked poly(2-hydroxyethyl methacrylate) hydrogels. *Journal of biomedical materials research* **19**, 397-411, doi:10.1002/jbm.820190405 (1985).
- 158 Migliaresi, C., Nicodemo, L., Nicolais, L. & Passerini, P. Physical characterization of microporous poly(2-hydroxyethyl methacrylate) gels. *Journal of biomedical materials research* **15**, 307-317, doi:10.1002/jbm.820150303 (1981).
- 159 Zhang, J. & Peppas, N. A. Morphology of poly(methacrylic acid)/poly(N-isopropyl acrylamide) interpenetrating polymeric networks. *Journal of biomaterials science. Polymer edition* **13**, 511-525 (2002).
- 160 Bell, C. L. & Peppas, N. A. Water, solute and protein diffusion in physiologically responsive hydrogels of poly (methacrylic acid-g-ethylene glycol). *Biomaterials* **17**, 1203-1218 (1996).
- 161 Brannon-Peppas, L. & Peppas, N. A. Dynamic and equilibrium swelling behaviour of pH-sensitive hydrogels containing 2-hydroxyethyl methacrylate. *Biomaterials* **11**, 635-644 (1990).
- 162 Mikos, A. G. & Peppas, N. A. Flory interaction parameter chi for hydrophilic copolymers with water. *Biomaterials* **9**, 419-423 (1988).
- 163 Chakrabarty, A., Zhang, L., Cavicchi, K. A., Weiss, R. A. & Singha, N. K. Tailor-Made Fluorinated Copolymer/Clay Nanocomposite by Cationic RAFT Assisted Pickering Miniemulsion Polymerization. *Langmuir : the ACS journal of surfaces and colloids* **31**, 12472-12480, doi:10.1021/acs.langmuir.5b01799 (2015).
- 164 Lu, Y. & Larock, R. C. New hybrid latexes from a soybean oil-based waterborne polyurethane and acrylics via emulsion polymerization. *Biomacromolecules* **8**, 3108-3114, doi:10.1021/bm700522z (2007).
- 165 Culver, H. R., Steichen, S. D., Herrera-Alonso, M. & Peppas, N. A. Versatile Route to Colloidal Stability and Surface Functionalization of Hydrophobic Nanomaterials. *Langmuir : the ACS journal of surfaces and colloids* **32**, 5629-5636, doi:10.1021/acs.langmuir.6b00929 (2016).
- 166 Schade, R., Weiss, T., Berg, A., Schnabelrauch, M. & Liefelth, K. Two-photon techniques in tissue engineering. *The International journal of artificial organs* **33**, 219-227 (2010).
- 167 Otto, D. P., Vosloo, H. C., Liebenberg, W. & de Villiers, M. M. Development of microporous drug-releasing films cast from artificial nanosized latexes of poly(styrene-co-methyl methacrylate) or poly(styrene-co-ethyl methacrylate). *European journal of pharmaceutics and biopharmaceutics : official journal of Arbeitsgemeinschaft fur Pharmazeutische Verfahrenstechnik e.V* **69**, 1121-1134, doi:10.1016/j.ejpb.2008.02.004 (2008).
- 168 M. Vacatello, P. J. F. <Conformational statistics of poly(methyl methacrylate)\_P J Flory 1985.pdf>. (1985).
- 169 Saigal, T. *et al.* Stable emulsions with thermally responsive microstructure and rheology using poly(ethylene oxide) star polymers as emulsifiers. *Journal of colloid and interface science* **394**, 284-292, doi:10.1016/j.jcis.2012.11.033 (2013).

- 170 Kondo, A., Xu, H., Abe, H. & Naito, M. Thermoresponsive gelling behavior of concentrated alumina suspensions containing poly(acrylic acid) and PEO-PPO-PEO copolymer. *Journal of colloid and interface science* **373**, 20-26, doi:10.1016/j.jcis.2011.09.071 (2012).
- 171 Bland, M. H. & Peppas, N. A. Photopolymerized multifunctional (meth)acrylates as model polymers for dental applications. *Biomaterials* **17**, 1109-1114 (1996).
- 172 Etz, C. D. *et al.* Vascular graft replacement of the ascending and descending aorta: do Dacron grafts grow? *The Annals of thoracic surgery* **84**, 1206-1212; discussion 1212-1203, doi:10.1016/j.athoracsur.2007.05.034 (2007).
- 173 Hata, H. *et al.* Replacement of the aortic root and ascending aorta using a freestyle valve and woven Dacron graft. *Artificial organs* **26**, 862-867 (2002).
- 174 Franke, U. *et al.* In vivo morphology of woven, collagen-sealed Dacron prostheses in the thoracic aorta. *The Annals of thoracic surgery* **64**, 1096-1098 (1997).
- 175 Lieberman, J. R., Lozman, J., Czajka, J. & Dougherty, J. Repair of Achilles tendon ruptures with Dacron vascular graft. *Clinical orthopaedics and related research*, 204-208 (1988).
- 176 Guidoin, R. *et al.* [Polyethylene terephthalate (Dacron) prostheses as arterial substitutes. Value of commercial grafts as abdominal aorta substitutes in the dog (author's transl)]. *Journal des maladies vasculaires* **5**, 3-12 (1980).
- 177 Oeconomos, N. Dacron prosthesis for coarctation of aorta with aneurysm; report of a case in a pregnant woman. *A.M.A. archives of surgery* **77**, 181-184 (1958).
- 178 Wood, P. A., Pidcock, E. & Allen, F. H. Interaction geometries and energies of hydrogen bonds to C[double bond]O and C[double bond]S acceptors: a comparative study. *Acta Crystallogr B* **64**, 491-496, doi:10.1107/S0108768108015437 (2008).
- 179 Leobandung, W., Ichikawa, H., Fukumori, Y. & Peppas, N. A. Preparation of stable insulin-loaded nanospheres of poly(ethylene glycol) macromers and N-isopropyl acrylamide. *Journal of controlled release : official journal of the Controlled Release Society* **80**, 357-363 (2002).
- 180 Jung, Y., Lee, S. H., Kim, S. H., Lim, J. C. & Kim, S. H. Synthesis and characterization of the biodegradable and elastic terpolymer poly(glycolide-co-L-lactide-co--caprolactone) for mechano-active tissue engineering. *Journal of biomaterials science. Polymer edition* **24**, 386-397, doi:10.1080/09205063.2012.690281 (2013).
- 181 Jung, Y. *et al.* Cartilage regeneration with highly-elastic three-dimensional scaffolds prepared from biodegradable poly(L-lactide-co-epsilon-caprolactone). *Biomaterials* **29**, 4630-4636, doi:10.1016/j.biomaterials.2008.08.031 (2008).
- 182 Garkhal, K., Verma, S., Tikoo, K. & Kumar, N. Surface modified poly(L-lactide-co-epsilon-caprolactone) microspheres as scaffold for tissue engineering. *Journal of biomedical materials research. Part A* **82**, 747-756, doi:10.1002/jbm.a.31150 (2007).
- 183 Shum-Tim, D. *et al.* Tissue engineering of autologous aorta using a new biodegradable polymer. *The Annals of thoracic surgery* **68**, 2298-2304; discussion 2305 (1999).
- 184 Freed, L. E. *et al.* Biodegradable polymer scaffolds for tissue engineering. *Bio/technology* **12**, 689-693 (1994).
- 185 Keeley, R. D., Nguyen, K. D., Stephanides, M. J., Padilla, J. & Rosen, J. M. The artificial nerve graft: a comparison of blended elastomer-hydrogel with polyglycolic acid conduits. *Journal of reconstructive microsurgery* **7**, 93-100, doi:10.1055/s-2007-1006766 (1991).
- 186 Berman, M., Pearce, W. J. & Tinnin, M. The use of Gore-Tex E-PTFE bonded to silicone rubber as an alloplastic implant material. *Laryngoscope* **96**, 480-483 (1986).

- 187 Reynolds, M. M., Frost, M. C. & Meyerhoff, M. E. Nitric oxide-releasing hydrophobic  
polymers: preparation, characterization, and potential biomedical applications. *Free  
Radic Biol Med* **37**, 926-936, doi:10.1016/j.freeradbiomed.2004.06.019 (2004).
- 188 Kesti, M. *et al.* A versatile bioink for three-dimensional printing of cellular scaffolds  
based on thermally and photo-triggered tandem gelation. *Acta biomaterialia* **11**, 162-  
172, doi:10.1016/j.actbio.2014.09.033 (2015).
- 189 Simmons, P. A., Kelly, W., Prather, W. & Vehige, J. Clinical benefits and physical  
properties of addition of hydroxypropyl methylcellulose to a multi-purpose contact lens  
care solution. *Advances in experimental medicine and biology* **506**, 981-985 (2002).
- 190 Olubamiji, A. D. *et al.* Modulating mechanical behaviour of 3D-printed cartilage-mimetic  
PCL scaffolds: influence of molecular weight and pore geometry. *Biofabrication* **8**,
- 191 Panja, S., Saha, B., Ghosh, S. K. & Chattopadhyay, S. synthesis of novel four armed PE-  
PCL grafted superparamagnetic and biocompatible nanoparticles. *Langmuir : the ACS  
journal of surfaces and colloids* **29**, 12530-12540, doi:10.1021/la401811c (2013).
- 192 Zhang, M. *et al.* Small-diameter tissue engineered vascular graft made of electrospun  
PCL/lecithin blend. *Journal of materials science. Materials in medicine* **23**, 2639-2648,  
doi:10.1007/s10856-012-4721-4 (2012).
- 193 Duling, R. R., Dupaix, R. B., Katsube, N. & Lannutti, J. Mechanical characterization of  
electrospun polycaprolactone (PCL): a potential scaffold for tissue engineering. *Journal  
of biomechanical engineering* **130**, 011006, doi:10.1115/1.2838033 (2008).
- 194 Tajiri, N. *et al.* Cerebral aneurysm as an exacerbating factor in stroke pathology and a  
therapeutic target for neuroprotection. *Curr Pharm Des* **18**, 3663-3669 (2012).
- 195 Bergamini, T. M. Regarding "Treatment of vascular graft infection by in situ replacement  
with a rifampin-bonded gelatin-sealed Dacron graft". *Journal of vascular surgery* **20**,  
847-848 (1994).
- 196 Duan, B., Kapetanovic, E., Hockaday, L. A. & Butcher, J. T. Three-dimensional printed  
trileaflet valve conduits using biological hydrogels and human valve interstitial cells.  
*Acta biomaterialia* **10**, 1836-1846, doi:10.1016/j.actbio.2013.12.005 (2014).
- 197 Rennerfeldt, D. A., Renth, A. N., Talata, Z., Gehrke, S. H. & Detamore, M. S. Tuning  
mechanical performance of poly(ethylene glycol) and agarose interpenetrating network  
hydrogels for cartilage tissue engineering. *Biomaterials* **34**, 8241-8257,  
doi:10.1016/j.biomaterials.2013.07.052 (2013).
- 198 Bussemer, T., Peppas, N. A. & Bodmeier, R. Evaluation of the swelling, hydration and  
rupturing properties of the swelling layer of a rupturable pulsatile drug delivery system.  
*European journal of pharmaceuticals and biopharmaceutics : official journal of  
Arbeitsgemeinschaft fur Pharmazeutische Verfahrenstechnik e.V* **56**, 261-270 (2003).
- 199 Azadani, A. N. *et al.* Mechanical properties of surgical glues used in aortic root  
replacement. *The Annals of thoracic surgery* **87**, 1154-1160,  
doi:10.1016/j.athoracsur.2008.12.072 (2009).
- 200 Lai, V. K. *et al.* Microstructural and mechanical differences between digested collagen-  
fibrin co-gels and pure collagen and fibrin gels. *Acta biomaterialia* **8**, 4031-4042,  
doi:10.1016/j.actbio.2012.07.010 (2012).
- 201 Cummings, C. L., Gawlitta, D., Nerem, R. M. & Stegemann, J. P. Properties of engineered  
vascular constructs made from collagen, fibrin, and collagen-fibrin mixtures.  
*Biomaterials* **25**, 3699-3706, doi:10.1016/j.biomaterials.2003.10.073 (2004).

- 202 Siepmann, J., Kranz, H., Bodmeier, R. & Peppas, N. A. HPMC-matrices for controlled drug  
delivery: a new model combining diffusion, swelling, and dissolution mechanisms and  
predicting the release kinetics. *Pharmaceutical research* **16**, 1748-1756 (1999).
- 203 Vinatier, C. *et al.* A silanized hydroxypropyl methylcellulose hydrogel for the three-  
dimensional culture of chondrocytes. *Biomaterials* **26**, 6643-6651,  
doi:10.1016/j.biomaterials.2005.04.057 (2005).
- 204 Zatloukal, Z. & Sklupalova, Z. Sterilized ophthalmic hydrogels with hydroxypropyl  
methylcellulose: determination and mathematical treatment of flow properties.  
*Pharmaceutical development and technology* **12**, 55-60,  
doi:10.1080/10837450601166593 (2007).
- 205 N. Davidenko, T. G. <AA -Biomimetic Collagen Scaffolds with Anisotropic Pore  
Architecture.Cambridge.2009.pdf>. (2009).
- 206 Roy, A. *et al.* Effects of plasticizers and surfactants on the film forming properties of  
hydroxypropyl methylcellulose for the coating of diclofenac sodium tablets. *Saudi  
pharmaceutical journal : SPJ : the official publication of the Saudi Pharmaceutical Society*  
**17**, 233-241, doi:10.1016/j.jsps.2009.08.004 (2009).
- 207 Meinel, L. *et al.* Bone tissue engineering using human mesenchymal stem cells: effects  
of scaffold material and medium flow. *Annals of biomedical engineering* **32**, 112-122  
(2004).
- 208 Hinton, T. J. *et al.* Three-dimensional printing of complex biological structures by  
freeform reversible embedding of suspended hydrogels. *Sci Adv* **1**, e1500758,  
doi:10.1126/sciadv.1500758 (2015).
- 209 Reid, J. A. *et al.* Accessible bioprinting: adaptation of a low-cost 3D-printer for precise  
cell placement and stem cell differentiation. *Biofabrication* **8**, 025017,  
doi:10.1088/1758-5090/8/2/025017 (2016).
- 210 Niklason, L. E. & Langer, R. S. Advances in tissue engineering of blood vessels and other  
tissues. *Transplant immunology* **5**, 303-306 (1997).
- 211 Radisic, M. *et al.* High-density seeding of myocyte cells for cardiac tissue engineering.  
*Biotechnology and bioengineering* **82**, 403-414, doi:10.1002/bit.10594 (2003).
- 212 Wu, Y. F. *et al.* Reendothelialization of tubular scaffolds by sedimentary and rotative  
forces: a first step toward tissue-engineered venous graft. *Cardiovascular  
revascularization medicine : including molecular interventions* **9**, 238-247,  
doi:10.1016/j.carrev.2008.01.005 (2008).
- 213 Thomas, L. V. & Nair, P. D. The effect of pulsatile loading and scaffold structure for the  
generation of a medial equivalent tissue engineered vascular graft. *BioResearch open  
access* **2**, 227-239, doi:10.1089/biores.2013.0003 (2013).
- 214 Schipke, K. J., To, S. D. & Warnock, J. N. Design of a cyclic pressure bioreactor for the ex  
vivo study of aortic heart valves. *Journal of visualized experiments : JoVE*,  
doi:10.3791/3316 (2011).
- 215 DiMuzio, P. *et al.* Development of a tissue-engineered bypass graft seeded with stem  
cells. *Vascular* **14**, 338-342 (2006).
- 216 Nieponice, A. *et al.* Development of a tissue-engineered vascular graft combining a  
biodegradable scaffold, muscle-derived stem cells and a rotational vacuum seeding  
technique. *Biomaterials* **29**, 825-833, doi:10.1016/j.biomaterials.2007.10.044 (2008).
- 217 Augustinus Bader, T. S. <Tissue engineering of heart valves - human endothelial cell  
seeding of detergent acellularized porcine valves\_Germany 1998.pdf>. *European Journal  
of Cardio-Thoracic Surgery* **14** (1998).

- 218 Checa, S., Rausch, M. K., Petersen, A., Kuhl, E. & Duda, G. N. The emergence of extracellular matrix mechanics and cell traction forces as important regulators of cellular self-organization. *Biomechanics and modeling in mechanobiology* **14**, 1-13, doi:10.1007/s10237-014-0581-9 (2015).
- 219 Bajaj, P., Schweller, R. M., Khademhosseini, A., West, J. L. & Bashir, R. 3D biofabrication strategies for tissue engineering and regenerative medicine. *Annual review of biomedical engineering* **16**, 247-276, doi:10.1146/annurev-bioeng-071813-105155 (2014).
- 220 Azadani, A. N. *et al.* Transcatheter aortic valves inadequately relieve stenosis in small degenerated bioprostheses. *Interactive cardiovascular and thoracic surgery* **11**, 70-77 (2010).
- 221 Celli, M., Alves, L. S. & Barletta, A. Nonlinear stability analysis of Darcy's flow with viscous heating. *Proceedings. Mathematical, physical, and engineering sciences / the Royal Society* **472**, 20160036, doi:10.1098/rspa.2016.0036 (2016).
- 222 Li, J. *et al.* A novel strategy to graft RGD peptide on biomaterials surfaces for endothelization of small-diameter vascular grafts and tissue engineering blood vessel. *Journal of materials science. Materials in medicine* **19**, 2595-2603, doi:10.1007/s10856-007-3354-5 (2008).
- 223 Vlachopoulos, J. <The Role of Rheology in Polymer Extrusion.Canada.pdf>.

## APPENDIX

The properties of different mixtures were explored and are mentioned briefly because of their biocompatibility. Specifically, PEO, sodium alginate, gelatin from porcine skin Type A and HPMC were also tested.

**Table 17. PEO copolymer hydrogel with PEGDA 700.**

Weighout:		Polymer solution with photoinitiator			Volume, mL
Ingredient:	Density, g/ml	Weight, grams:	Baker's %:	w/v	
PEGDA MW700 at 15°C	1.100	3.00	78.9%	15.0%	2.73
PEO	5.000	1.00	26.3%	5.0%	0.20
LAP	10.000	0.030	0.8%	0.15%	0.00
Deionized Water	1.000	17.070	449%	79.9%	17.07
Set desired volume total, mL	20			100.0%	20.00

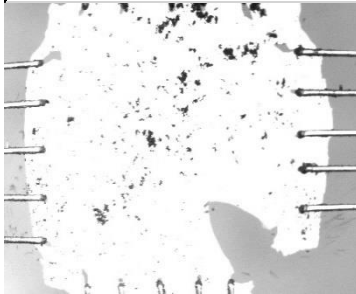


**Figure 77. Top, fracture of PEO-PEGDA copolymer hydrogel at 22% Green strain. Right, biaxial stretch data plot compared with human aortic tissue.**

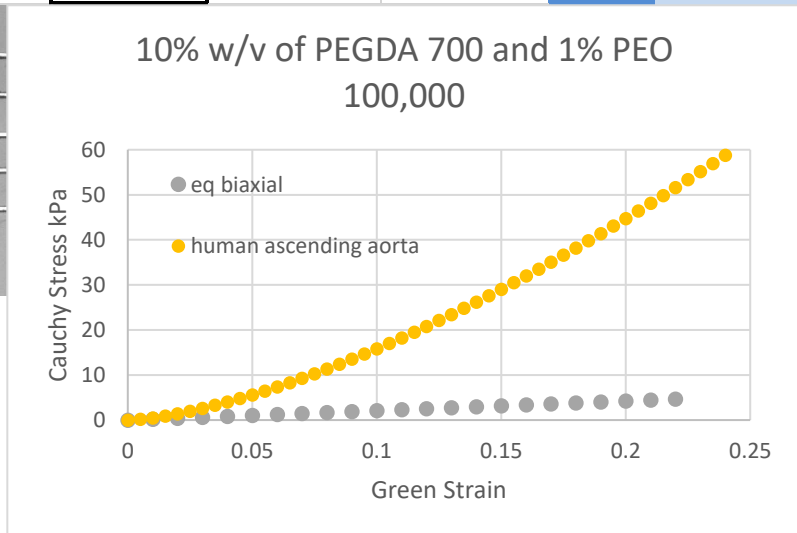




**Table 18. Gelatin copolymer with PEGDA 700.**

Weighout:		Polymer solution with photoinitiator			Volume, mL
Ingredient:	Density, g/ml	Weight, grams:	Baker's %:	w/v	
PEGDA MW700 at 15°C	1.100	3.00	78.9%	15.0%	2.73
Gelatin from porcine skin Type A	4.000	1.00	26.3%	5.0%	0.25
LAP	10.000	0.030	0.8%	0.15%	0.00
Deionized Water	1.000	17.020	448%	79.9%	17.02
Set desired volume total, mL	20			100.0%	20.00

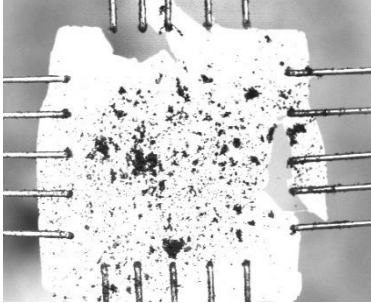


**Figure 78. Top, fracture of Gelatin-PEGDA (5-15% w/v) copolymer hydrogel at 3% Green strain. Right, biaxial stretch data plot comparing concentration of PEGDA 700 at 10% and 15% w/v.**

**Equibiaxial - Gelatin 5% w/v PEGDA 10 & 15% w/v Copolymer Effects**

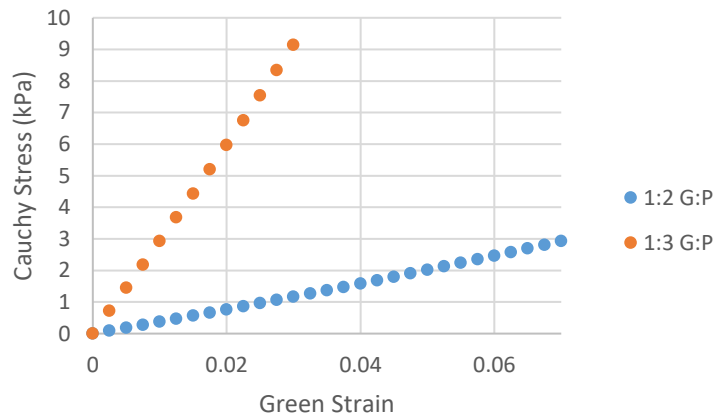


**Table 19. Alginate copolymer with PEGDA 700.**

Weighout:		Polymer solution with photoinitiator			Volume, mL
Ingredient:	Density, g/ml	Weight, grams:	Baker's %:	w/v	
PEGDA MW700 at 15°C	1.100	3.00	78.9%	15.0%	2.73
Sodium Alginate	10.000	0.80	21.1%	4.0%	0.08
LAP	10.000	0.030	0.8%	0.15%	0.00
Calcium Chloride	10.000	0.080	2.1%	0.40%	0.01
Deionized Water	1.000	17.182	452%	80.5%	17.18
Set desired volume total, mL	20			100.0%	20.00

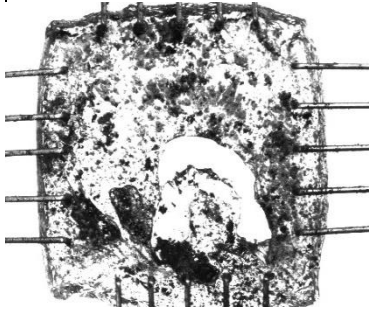


**Figure 79. Top, fracture of Alginate-PEGDA (4-15% w/v) copolymer hydrogel at 4% Green strain. Right, biaxial stretch data plot comparing the effect of concentration of PEGDA 700 and alginate on the mechanical properties.**

**Interpenetrating networks of ionic and covalently crosslinked matrices**

